

Review

Low-temperature electron-transporting materials for perovskite solar cells: Fundamentals, progress, and outlook

Haonan Si ^{a,b}, Xuan Zhao ^{a,b}, Zheng Zhang ^{a,b}, Qingliang Liao ^{a,b,*}, Yue Zhang ^{a,b,*}^a Academy for Advanced Interdisciplinary Science and Technology, Beijing Advanced Innovation Center for Materials Genome Engineering, University of Science and Technology Beijing, Beijing 100083, People's Republic of China^b Key Laboratory of Advanced Materials and Devices for Post-Moore Chips, Ministry of Education, Beijing Key Laboratory for Advanced Energy Materials and Technologies, School of Materials Science and Engineering, University of Science and Technology Beijing, Beijing 100083, People's Republic of China

ARTICLE INFO

ABSTRACT

Keywords:

Perovskite solar cells
Electron-transporting materials
Low-temperature fabrication
Perovskite modules

Perovskite solar cells (PSCs) have unprecedentedly rapid emerged as a promising next-generation clean-energy-harvesting technology. Compelling market advantages over existing photovoltaic devices include material properties and low-temperature processes. Throughout the development of PSCs, the electron-transporting materials (ETMs) as an integral part, has played a distinctive role in photon-to-electron conversion and device stability. With the accelerating commercialization, the market demand puts forward new criterion for the evolution of ETMs to suitable for flexible, tandem cells and large-scale module development. However, guidelines for low-temperature ETMs critical for industrial applications are still missing. In this review, we discuss the fundamental theory and propose the design guideline of low-temperature ETMs for economical, efficient and stable PSCs. Then, the notable progress of low-temperature ETMs is outlined with emphasis focused on the various low-temperature processing routes. Further, we emphatically reviewed the optimization strategies of low-temperature ETMs for champion solar cells, and extend to large-scale ETMs covering their strategic importance, current status, and development tendency. Beyond that, the service mechanism of low-temperature ETMs are systematically summarized. We conclude with an outlook of critical targets, the key technical challenges of low-temperature ETMs, and outline potential pathways to push the performance bottleneck of low-temperature perovskite cells and modules.

1. Introduction

Solar energy as a clean and renewable energy is abundant and less dependent on geographical locations. According to the 'Global Renewable Energy Market Outlook', nearly a third of the worldwide new electricity generation capability will rely on photovoltaic technology by 2030.^[1] In photovoltaic field, silicon cells are still dominant. Opportunities exist for emerging cells that promise either dramatically higher power conversion efficiency (PCE) or significantly lower fabrication cost. Perovskite solar cells (PSCs) exhibit excellent prospects in both fronts. Historically, there has been no photovoltaic cell like the PSC, which has achieved a staggering 26.1 % photoelectric conversion efficiency in just a few years.^[2] This efficiency exceeds the PCEs of multi-crystalline Si (23.3 %), thin-film crystalline Si (21.2 %), CdTe-based thin-film cells (22.3 %), copper indium gallium selenide (23.6 %),

organic cells (19.2 %) and dye-sensitized cells (13.0 %).^[2] Such extraordinary device performance is not surprising, since the mixed organic-inorganic halide perovskites have strong solar absorption ability in the visible and near-infrared region, low non-radiative carrier recombination rate, long carrier lifetime and diffusion length, as well as high defect tolerance.^[3] Nowadays, more than 190,000 related research articles emerge and numerous companies including Oxford PV, Microquanta, Golden Concord Holdings Limited and Dyesol, look at its commercial applications.^[4]

Beyond the incredible efficiency granted by excellent photoelectric properties, the convenience of solution processing of perovskite materials has contributed to the widespread proliferation of PSC research around the world.^[5] The multiformity in processing methods may give rise to low preparation costs and simple implementation of proactive products, such as flexible, semi/fully-transparent PSC modules.^[6]

* Corresponding authors at: Academy for Advanced Interdisciplinary Science and Technology, Beijing Advanced Innovation Center for Materials Genome Engineering, University of Science and Technology Beijing, Beijing 100083, People's Republic of China.

E-mail addresses: liao@ustb.edu.cn (Q. Liao), yuezhang@ustb.edu.cn (Y. Zhang).

Specifically, the first examples of flexible PSC were in the n-i-p configuration with $\text{CH}_3\text{NH}_3\text{PbI}_3$ (MAPbI₃) perovskite built on ZnO ETMs.^[7] Later, the low-temperature TiO_x ETM prepared via atomic layer deposition (ALD) was inserted underneath perovskite materials, which realized a high efficiency of 12.2 %.^[8] In 2015, the room-temperature processed Zn₂SO₄ nanoparticles on PEN/ITO substrate achieved 15.3 % efficiency.^[9] The development of highly crystalline low-temperature ETMs is crucial for efficient flexible perovskite devices and modules.^[10,11] Recently, the PCE of small-area flexible PSC based on low temperature SnO₂ has been improved over 23.94 % (Fig. 1).^[12] Moreover, the advantage of low-temperature preparation makes perovskite materials have a unique development prospect in the field of high-performance tandem cells. The PSCs are usually applied as top cells and the ZnO, SnO₂ serve as ETMs as well as buffer layer.^[13] At present, the tandem PSCs have achieved an efficiency over 33.7 %.^[14] Obviously, in contrast with traditional PSCs based on glass substrate, the charge transport materials, especially the ETMs, should be formed at a low temperature of below 150 °C due to the poor heat resistance of plastic substrates and bottom cells, which is quite a challenge to realize high efficiency. Incontestably, the development of highly crystalline low-temperature ETMs is crucial for efficient flexible/tandem perovskite devices and modules. Thus, the constant drive to push the PCE toward a new gradient has lately increased the search for more efficient and low temperature processable ETMs.^[4]

Herein, this review provides an up-to-date summary of the recent development of low-temperature ETMs for PSCs and modules. In the light of condensed design guidelines of the ideal low-temperature ETMs, we summarize the fundamental characteristics and outline the pros and cons of various ETMs. Then, we discuss the widely proposed cryogenic deposition approaches, examine the progress in performance and provide an overview of the methodologies for achieving high-quality low-temperature ETMs. Further, the progress in the optimization of low-temperature ETMs for high-performance PSCs have been further summarized. Moreover, we emphasize the strategic importance of developing large-area low-temperature ETMs for perovskite modules, summarize recent progress in minimizing the efficiency gap, and highlight the development tendency for moving PSCs technology toward industrial scale. Beyond that, service behavior evaluation of low-temperature ETMs is summarized and the relevant stability issues are scrutinized. We conclude with a perspective on the challenges and opportunities of low-temperature ETM towards future practical

applications.

2. Fundamentals of Low-Temperature ETMs

2.1. Design guideline of low-temperature ETMs

PSCs have attracted tremendous attention in the past decade due to the merit of high efficiency. Generally, the efficient PSCs comprise an intrinsic perovskite absorber sandwiched between n-type ETMs and p-type hole-transporting materials (HTMs). These materials act as a medium for collecting and transferring photogenerated carriers.^[15] At the micro level, the outstanding performance is premised on effective photoinduced-carrier generation and charge separation. However, the undesired photovoltaic processes include (1) recombination within perovskite bulk, (2) back charge transfer at ETM/perovskite interfaces, (3) charge transfer at HTM/perovskite interfaces, and (4) charge transfer between ETM and the HTM, severely restrict the efficiency, as illustrated in Fig. 2. In order to acquire high performance, above undesired processes (1–4) should be controlled at slower timescales than charge generation and extraction. It proposes high demands for ETMs as well as the contact interface.^[16] More important, the ETMs serve as the platform for subsequent perovskite growth and dominate its crystallization quality, which also highlight the remarkable role of ETMs. Regarding the unsatisfactory operational stability of PSCs, the low-temperature ETMs and ETM/perovskite interface should be carefully assessed. In this context, we dissect the market demand and put forward the design guidelines of low-temperature ETMs from the Angle of materials and processing.

(1) Excellent optoelectronic properties

The optical and electrical properties of ETMs directly affect the charge transport behavior within PSCs, particularly on the nano- to microscale -, which is essential to push devices to their performance limits.

- To ensure a high current density, the ETMs should process broad optical transparency to guarantee maximum light absorption in the n-i-p PSCs, particularly in tandem cells. ^[17] Furthermore, the low-temperature ETMs should feature a high optical bandgap

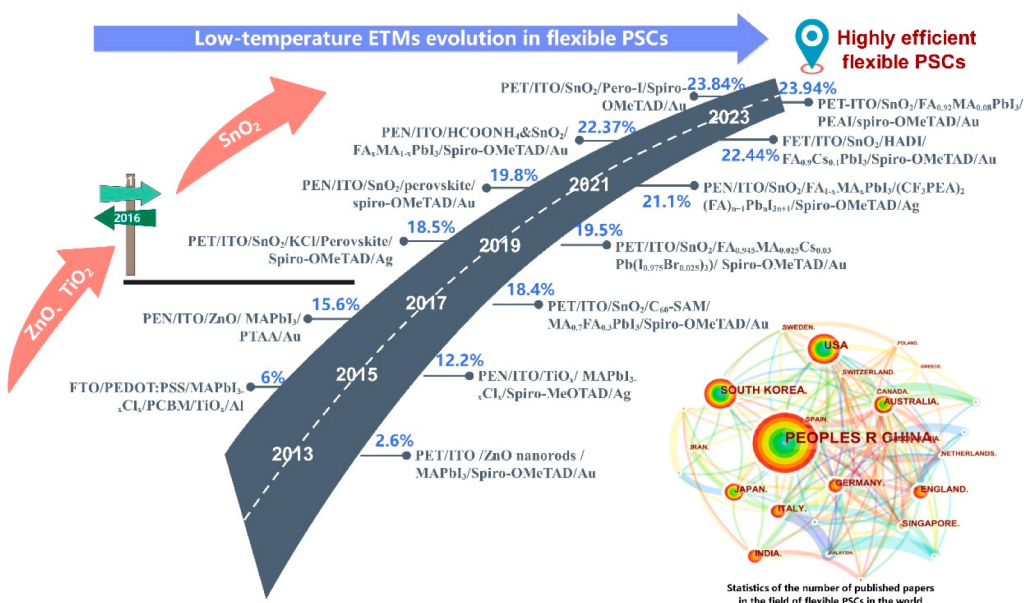


Fig. 1. Efficiencies evolution of reported typical flexible PSCs based on various low-temperature ETMs.

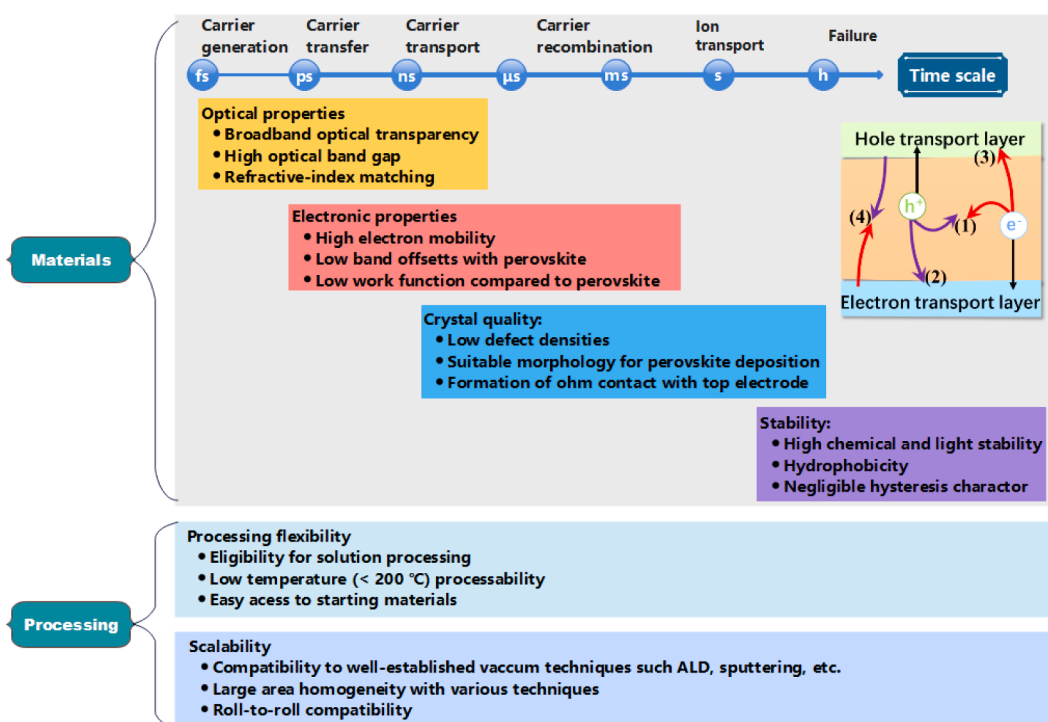


Fig. 2. Schematic diagram of the charge transfer process and the factors for ideal low-temperature ETMs.

and a low refractive index to realize the optical match and transmittance enhancement.

- To effectively extract the photogenerated charges from perovskite absorbers, a slightly lower conduction band minimum (CBM) level relative to that of perovskite absorber is preferred. While the lower valence band maximum (VBM) level than that of the perovskite materials is necessary to realize the exciton confinement and hole-blocking function. Moreover, the high electron mobility is also important to withstand the space-charge-limit effect induced by the charge accumulation at the interface.

(2) High crystallization quality

In view of the ambipolar transport property of perovskite absorber, the highly crystalline ETM is important for efficient PSCs. The conformal, uniform and pinhole-free morphology of ETMs is needed to avoid the current leakage and charge recombination[18]. Especially, the low-temperature ETMs fabricate at relative low temperature should pay more attention to the crystal defects. On the device level, the suitable morphology of ETMs dictates sequent perovskite growth and dominate its crystallization quality. As for electrode interface, the formation of selective ohmic contact put requirements on ETMs quality.

(3) Long-term stability

The stability of PSCs has been widely questioned, and the contact stability is one of the key constraints. Due to the moisture-sensitive property of perovskite materials, the hydrophobicity of ETMs in perovskite-based cells is vital for device stability[19]. Also, the ETMs should have high chemical resistance to polar aprotic solvents[20]. And then, the ideal ETMs should have chemical inertness with negligible catalytic properties. Meanwhile, the stable ETMs are irresponsive to UV-light. Last but not least, the long-term operational stability of ETMs in PSCs is also important.

(4) Process flexible

The eligibility for solution processing of ETMs at low temperature

(<200 °C) enables the device fabrication on temperature-sensitive substrates as well as tandem bottom cells specimen. Additionally, the flexible low-temperature processing is critical toward compatibility with large-area fabrication and high-throughput applications. Moreover, easy access to starting materials should also be mentioned.

(5) Scalability

The scaling of PSCs into large scale modules puts forward new demands on the scalability of ETMs. The compatibility to well-established scalable deposition methods, such as sputtering, ALD etc. as well as roll-to-roll process is beneficial to the development of perovskite modules. Also, various scalable fabrication techniques should guarantee the large area homogeneity of ETMs.

(6) Cost-effectiveness

Considering the commercial application of PSCs, the economic feasibility and sustainability of ETMs should be addressed. From this point of view, The ETMs should better naturally exist in the earth.

2.2. Basic theory of low-temperature ETMs

To date, numerous low-temperature processed n-type materials have already been employed in PSCs. Each material owns unique advantages to boost the PCE. Herein, we summarized and compared the optoelectronic properties of widely used low-temperature ETMs including binary and ternary inorganic low-temperature ETMs as well as organic ETMs. Also, we emphatically highlighted the advantages and inadequacies of various inorganic low-temperature ETMs for PSCs and modules. The comparison of common low-temperature ETMs is shown in Fig. 3.

2.2.1. Basic theory of binary low-temperature ETMs

(1) Low-temperature TiO₂

TiO₂ plays a vital role among various ETMs owing to the favorable

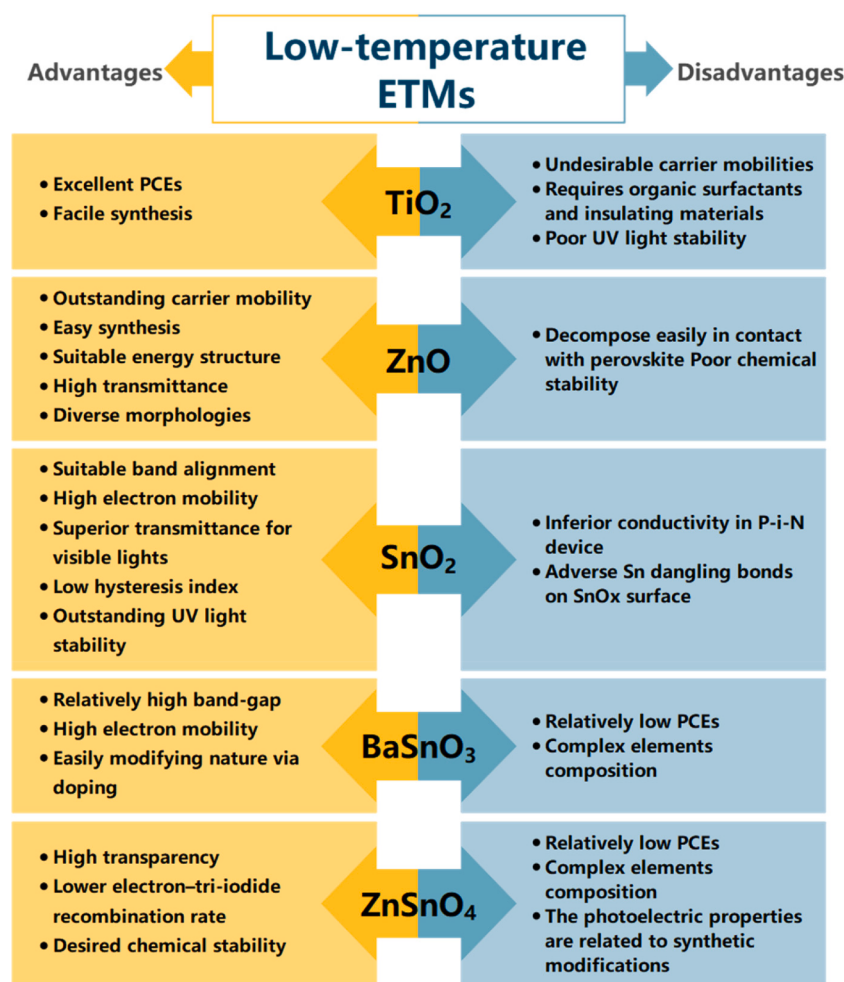


Fig. 3. Direct comparison of commonly used inorganic low-temperature ETMs.

opto-electronic properties. In detail, TiO_2 shows satisfactory CBM of -4.1 eV with a large bandgap (3.2 eV for anatase, 3.1 eV for brookite, and 3.0 eV for rutile, respectively) and low refractive index about 2.4–2.5, as demonstrated in Table 1.[21] The suitable energy band guarantees efficient electron injection and is appropriate for blocking holes. The commercial anatase TiO_2 nanoparticles (NPs) with $20 \sim 50$ nm are proposed to form mesoscopic structure, which has been extensively used in DSSCs and inherited by PSCs at early stage. However, high-temperature sintering process (around 500°C) is required to realize the phase transformation from amorphous TiO_2 into anatase phase, which is unfeasible on plastic substrates and unfavorable for future commercial applications. Fortunately, mesoscopic TiO_2 is not necessary for PSCs. The planar PSCs with compact TiO_2 layer have gradually become popular in latest researches.[16] In particular, the

compact TiO_2 layer is simple to synthesize and has the possibility of low-temperature preparation. Many researchers have tried various methods to optimize the preparation technique of TiO_2 layers under low temperatures to fulfill the requirement of highly efficient PSCs. Currently, several solution processes like sol-gel methods and liquid deposition methods, as well as various vapor deposition strategies have been proposed to prepare the low-temperature TiO_2 ETMs.

(2) Low-temperature ZnO

ZnO is another wide used ETMs and has been regarded as a potential alternative to TiO_2 . Specifically, ZnO owns a higher electron mobility than TiO_2 as well as the suitable energy structure (the CBM of -4.17 eV and the band gap 3.3 eV), which is conducive to the extraction and transport of electrons.[16] The high transmittance in whole visible spectrum enables efficient light absorption. More important, ZnO is easy synthesize and has plenty of fabrication methods.[22] It can be directly prepared by solution and vapor deposition methods at relatively low temperature, such as spin-coating, electrodeposition, hydrothermal growth and ALD et.al. Ease of low-temperature preparation enables ZnO to be used in regular (n-i-p) and inverted (p-i-n) PSCs as well as fully compatible to both rigid and flexible substrates [23,24]. Besides, the morphology can be controlled by tuning the growth methods and parameters at low cost. All above merits make ZnO a promising ETMs in PSCs.

(3) Low-temperature SnO_2

Table 1
Direct comparison of commonly used inorganic low-temperature ETMs.

ETMs	Conduction Band [eV]	Valance Band [eV]	Mobility [$\text{cm}^2\text{V}^{-1}\text{s}^{-1}$]	Refractive index	Ref.
TiO_2	-4.1	-7.3	0.1–4	2.4–2.5	[21]
ZnO	-4.2	-7.6	205–300	2.2	[16]
SnO_2	-4.5	-8.1	240	2	[16,17]
WO_x	-5.3	-8.3	10–20	1.95	[28]
CeO_x	-4.0	-7.5	0.01	1.6–2.5	[16]
Nb_2O_5	-4.25	-7.65	26	2.1–2.4	[30]
ZnSnO_4	-4.1	-7.8	10–30	~2	[9,35]
BaSnO_3	-3.9	-7.1	150	2.07	[36,37]

SnO_2 has been fully researched and successfully applied in the perovskite photovoltaic field over the past six years, mostly due to the combination of excellent photoelectrical performance and stability. Besides, the characteristic of low temperature preparation makes its application more extensive. In particular, SnO_2 merges favorable band structure with high electron mobility and superior transmittance for visible lights. The deep energy levels of conduction and valence band meets the requirement for electrons extraction and holes blocking. While the wide band gap of 3.6–4.5 eV and small reflective index of 2 conspire to contribute to superior transmittance.^[16,17] Many relative researches have pointed out that its transmittance for visible spectra can exceed 90 % or even more than 95 %.^[25] This feature ensures the light passes efficiently and in turns enhances the light absorption by perovskite materials. In addition, SnO_2 stands out among all competitors with electron mobility up to $421 \text{ cm}^2 \text{ V}^{-1} \text{ s}^{-1}$, which is 100 times compared with TiO_2 .^[17] This factor potentially enhances the electron transport capability and decrease the recombination loss. The detailed parameters are listed in Table 1. Beyond the optical and electrical properties, remarkable stability qualifies SnO_2 a promising material to construct efficient and stable PSCs. SnO_2 as one of the UV-inert ETMs could restrain the formation of oxygen defects, thus suppressing the UV-induced degradation to a certain extent.^[26] Moreover, SnO_2 is more suitable to prepare at low temperature than TiO_2 . The employ of SnO_2 will significantly promote the development of flexible devices and tandem solar cells. Recently, researchers have developed a number of effective low-temperature methods to prepare SnO_2 ETMs. SnO_2 can also be prepared as compact layers or mesoporous layers.^[27] The former is composed of SnO_2 nanocrystal particles for planar structure devices. While the latter is composed of nanocrystals, nanotubes and nanosheets as scaffold layers to increase contact area and improve charge extraction. Up to now, SnO_2 has occupied an important position in perovskite photovoltaic field with the advantages of outstanding performance and simple preparation approach. Here we will summarize the widely adopted fabrication strategies for low-temperature SnO_2 as well as the fundamental synthesis mechanism.

(4) Other binary low-temperature ETMs

Apart from the extensive utilized low-temperature TiO_2 , ZnO and SnO_2 ETMs, some alternative low-temperature ETMs have been employed, such as WO_x ,^[28] CeO_x ,^[29] Nb_2O_5 ^[30] and so on. For instance, WO_x as low-cost n-type semiconductor with wide band gap (2–3 eV) and high electron mobility ($10\text{--}20 \text{ cm}^2 \text{ V}^{-1} \text{ s}^{-1}$) could be fabricated at relative low temperature. In 2015, Ma *et al.* firstly employed the low-temperature WO_x ETM in PSCs.^[28] It was prepared by simple spin-coating an isopropyl solution of tungsten chloride followed by annealing at 150 °C and exhibited the better electrical conductivity than TiO_2 ETM. In 2017, Vedraine *et al.* ink-jet printed the WO_x ETM at 100 °C for the first time. But these low-temperature WO_x ETMs have relatively low Fermi level and in turns suffer from low Voc and FF. Recently, Gao *et al.* innovatively dissolved WCl_6 in hexanol which contributed to the transformation from precursor solution into stable colloidal particles.^[31] On the basis, the WO_x ETM with restrained charge recombination and boost Fermi level was fabricated at an ultra-low-temperature of 50 °C. CeO_x with suitable band gap and good ionic conductivity was also used to transport electrons. In 2017, Zheng *et al.* prepared the CeO_x ETM by so-gel method at 150 °C.^[32] Nb_2O_5 with similar optoelectronic property as TiO_2 was selected to act as the ETMs in PSCs. The e-beam evaporation process was developed to deposit Nb_2O_5 film with different thickness.^[33] The heat-treatment-free Nb_2O_5 with 60 nm thickness shown the largest recombination resistance and thereby the highest device performance. Subsequently, the two-dimensional Nb_2O_5 nanosheets with (001) orientation were synthesized by hydrothermal method.^[34] These structure effectively facilitated the charge transportation and contributed to PCE improvement.

2.2.2. Basic theory of ternary low-temperature ETMs

Besides the abovementioned binary metal oxide, some ternary oxides have recently been used as low-temperature ETMs. Among them, Zn_2SnO_4 is a well-known n-type semiconductor with high-electron Hall mobility ($10\text{--}30 \text{ cm}^2 \text{ V}^{-1} \text{ s}^{-1}$), wide band gap (3.8 eV) and desired chemical stability.^[35] While high temperature over 200 °C is always required to synthesize Zn_2SnO_4 ETM with highly dispersed nanoparticles, due to the complex elements composition. Prof. seok used hydrazine hydrate instead conventional NaOH to synthesis zinc ammine hydroxo complex (Zn-N-H-OH) precursors. Such designed precursor effectively suppressed the formation of ZnSn(OH)_6 intermediate phase. Compared with ZnSn(OH)_6 , the zinc ammine hydroxo complex only needs a relatively low temperature (<100 °C) to form Zn_2SnO_4 due to the low-energy kinetics of zinc-ammine dissociation, as well as hydroxide condensation and dehydration reactions. Though this kind of ternary oxide exhibits the excellent potential as ETMs for PSCs, the complicated fabrication processes may impede the further application for large-scale and flexible PSCs.

2.2.3. Basic theory of organic low-temperature ETMs

Organic n-type materials are among the popular choice for low-temperature ETMs, due to the impressive advantages, such as easy synthesis and purification, tunable frontier molecular orbitals, decent electron mobility, low cost, good solubility in different organic solvents, and reasonable chemical/thermal stability.^[38] On the basis, the optoelectronic properties and morphological characteristics of organic ETMs can be easily modulated by tailoring molecular structures. Additionally, the organic ETMs exhibit superior capabilities in defect passivation and suppression of non-radiative recombination in perovskite films, owing to the presence of electron-rich heteroatoms or heterocycles.^[39] Moreover, organic ETMs exhibit compatibility with low-temperature, flexible, and large-area fabrication processes while also demonstrating good batch-to-batch reproducibility. These characteristics are advantageous for the commercialization of PSCs.^[40] So far, various organic materials have been employed as ETMs in PSCs, including fullerene derivatives, rylene diimide polymers and small molecules, as well as fused-ring electron acceptors. To clarity, these materials can be categorized into two groups: fullerene-based derivatives and non-fullerene organic small molecules or polymers. [18] Fig. 4 illustrates the chemical structures and properties of fullerene derivatives and non-fullerene acceptors.

Fullerene C60 and its derivatives, particularly PCBM, are widely utilized as low-temperature ETMs due to their well-aligned energy levels with perovskite and excellent electron extraction/transport properties.^[38] Zhan *et al.* designed a series of fullerene dyads FP-Cn ($n = 4, 8, 12$) primarily consisting of a C60 cage, long alkyl chain, and terpyridine end group. These components are responsible for electron transportation, improved solubility, and chelation with the perovskite. The FP-C8 molecule has a lower unoccupied molecular orbital (LUMO) energy level of -4.15 eV, which is closer to the conductive band of perovskite and suggests better electron extraction ability. Additionally, its mobility and conductivity are higher than those of PCBM at $4.9 \times 10^{-3} \text{ cm}^2 \text{ V}^{-1} \text{ s}^{-1}$ and $2.6 \times 10^{-3} \text{ S cm}^{-1}$ respectively. The devices based on FP-C8/C60 with FAPbI_3 as a light absorber achieve a champion PCE of 23.08 % among inverted PSCs using solution-processed fullerene derivatives at that time.^[41] Recently, He *et al.* employed PC_{61}BM as ETMs to fabricate PSC with an ITO/Perovskite/ PC_{61}BM / BCP/ Ag architecture, achieving an impressive efficiency of 25.86 %.^[42] Additionally, the Rylene diimide polymers as one type of non-fullerene acceptors are highly suitable choices as ETMs in PSCs due to their excellent electron transport ability, adjustable LUMO energy level, abundant heteroatoms, and exceptional stability.^[40] Huang *et al.* designed an amino-functionalized copolymer with a conjugated backbone composed of fluorene, naphthalene diimide, and thiophene spacers (PFN-2TNDI). It possesses a suitable LUMO energy level of -3.84 eV and exhibits high electron mobility of $4.8 \times 10^{-4} \text{ cm}^2 \text{ V}^{-1} \text{ s}^{-1}$, resulting in a high device efficiency of 16.7 %.^[43]

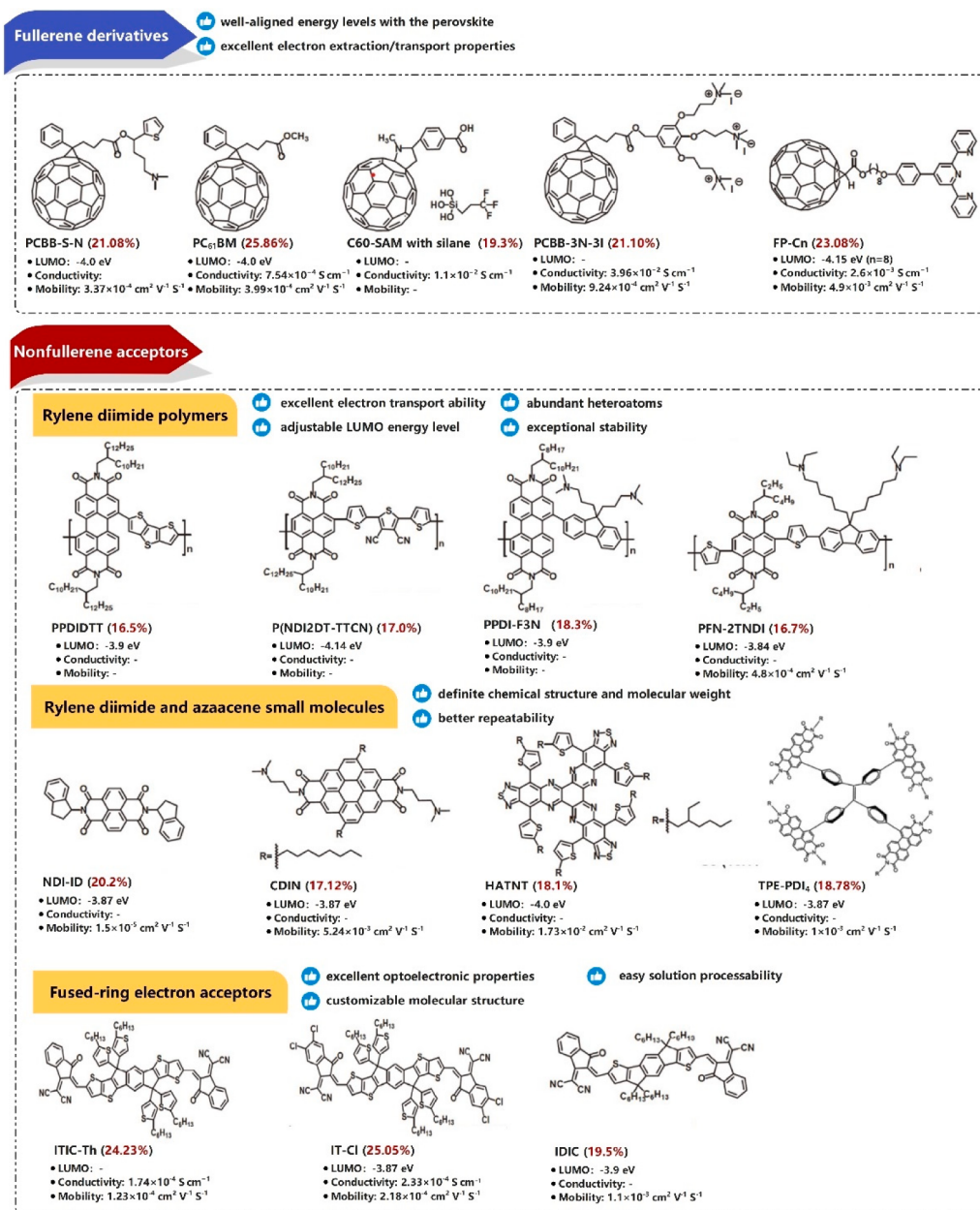


Fig. 4. The chemical structures and properties of fullerene derivatives and non-fullerene acceptors as ETMs in PSCs.

Moreover, compared with the polymers, the Rylene diimide and azaacene small molecules possess distinct chemical structure and molecular weight as well as better repeatability, making them widely utilized as ETMs in PSCs.[39] Kwon et al. designed and synthesized new nonfullerene organic ETMs based on NDI cores. The new NDI-ID ETM exhibits high electron mobility ($1.5 \times 10^{-5} \text{ cm}^2 \text{ V}^{-1} \text{ S}^{-1}$), similar to PCBM and its derivatives, along with suitable LUMO levels (-3.87 eV), resulting in a PCE exceeding 20 %.[44] Not only that, the Fused-ring electron acceptors are also widely used in PSCs due to their excellent optoelectronic properties, customizable molecular structure, and easy solution processability.[45] For example, the IT-IC ETM with a matched LUMO level of -3.87 eV, high conductivity ($2.33 \times 10^{-4} \text{ S cm}^{-1}$), and good electron mobility ($2.18 \times 10^{-4} \text{ cm}^2 \text{ V}^{-1} \text{ S}^{-1}$) was synthesized. Han et al. incorporated IT-Cl molecules as ETMs into regular PSCs and yielded a high PCE of 25.05 %.[46].

3. Synthetic methods of Low-Temperature ETMs

In view of the considerable achievements low-temperature ETMs have scored, it is necessary to take an overview of the development and popularization of cryogenic processing technology. Generally, the commonly used low-temperature synthetic methods can be divided into two categories: i) solution processing, which employs precursors and colloidal dispersions for deposition, such as spin-coating, print, chemical bath deposition, and ii) vapor deposition, which applies solid or liquid precursors or target materials, including ALD, magnetron sputtering, e-beam evaporation. In this Review, we analyze the current progress of solution- and vapor-based cryogenic processing technology of PSCs and modules. The comprehensive comparation of these processing strategies have been discussed and summarized in Fig. 5. On the basis of our analysis, we provide our views on the major challenges needed to be overcome to successfully minimize the efficiency gap (i.e., the difference in the performance between high-temperature techniques and low-temperature routes). The first challenge is related to the preparation

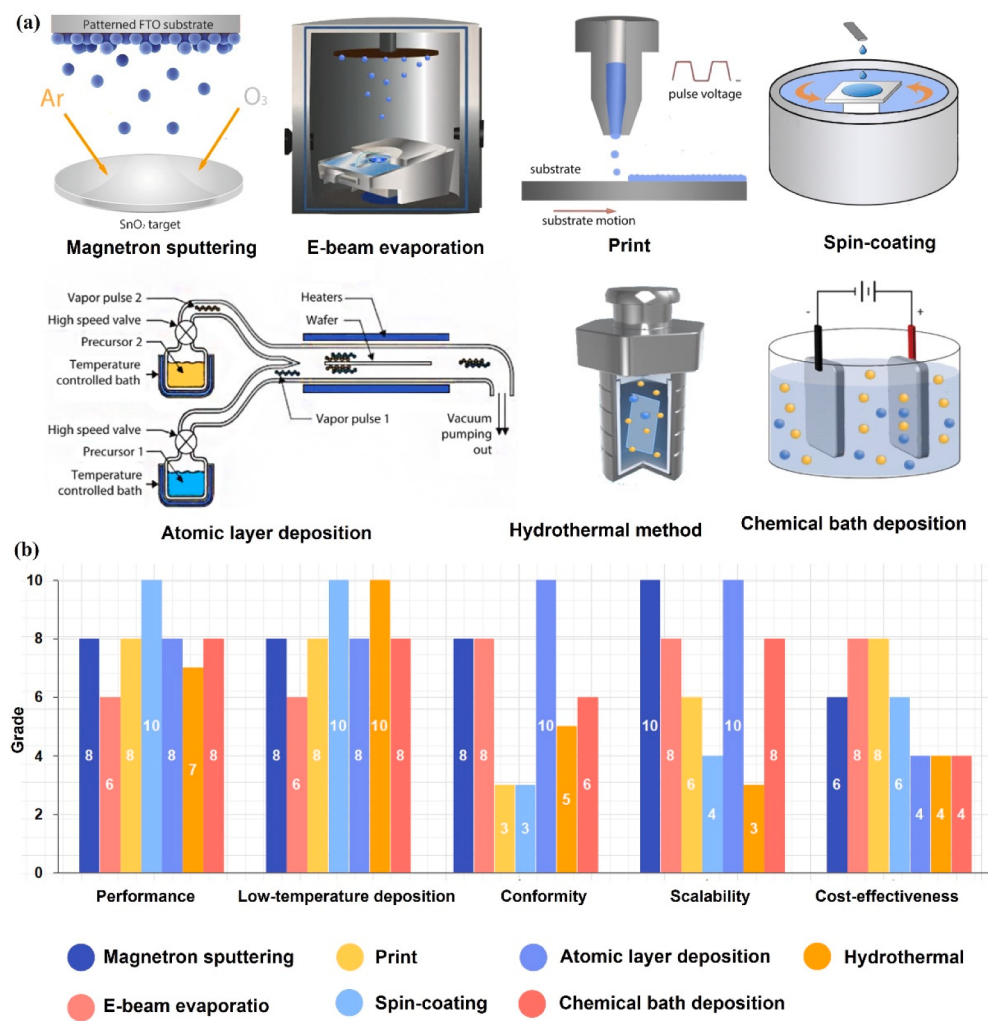


Fig. 5. (a) Illustration of various deposition strategies of low-temperature ETMs, (b) Lateral comparison of some low-temperature processing technologies (the qualitative characteristics are evaluated on a scale from one (lowest) to ten).

of high-quality (i.e., uniform coverage and chemical composition, high-crystallinity, and low surface roughness at relative low temperature) and reproducible films with adjacent perovskite layer forming the whole low-temperature PSC. The second challenge concerns the fabrication-cost issues during development of scale-up. As follows, we will discuss next in greater detail with a focus on the merits and demerits of single low-temperature ETMs and its processing -performance relation.

3.1. Solution-processed low-temperature ETMs

The solution-processed fabrication technologies generally use precursor solutions and colloidal dispersions for deposition, which have the advantages of low cost, high utilization rate of raw materials and roll-to-roll preparation. Currently one of the most challenging issues of above low-temperature solution synthesis routes is the need to reproducibly deposit smooth and pinhole-free ETMs with high-crystallinity, and uniform stoichiometry, especially across large areas. The understanding and control of the physicochemical dynamics during film growth, which are strongly dependent on the different coating processes and solution precursor, are requisites for attaining high-quality low-temperature ETMs.

3.1.1. Spin-coating method

Spin-coating is one of the widely used solution processing method, which can be considered to be a medium-size area technique (areas up to

a few 100 cm²) if the homogeneity can be carefully controlled. Moreover, spin-coating of nanoparticles is the most reported protocol due to its convenience, ease of access to raw materials, and high reproducibility. Nowadays, spin-coating method has become one of the main deposition techniques of low-temperature ETMs in the laboratory. As following, the progress of preparation of low-temperature ETMs by spin coating is introduced.

(1) The low-temperature TiO₂ deposited by spin-coating

Generally, the spin-coated TiO₂ ETMs require high-temperature sintering treatment. Fortunately, TiO₂ NPs can be synthesized through titanium tetrachloride and benzyl alcohol at relative low temperature. It enables the deposition of low-temperature TiO₂ (LT-TiO₂) ETMs by facilely spin-coating pre-formed NPs solution. Snaith *et al.* used the highly crystalline small TiO₂ NPs to fabricate the dense films by spin-coating method.^[47] To improve the adhesive properties of NPs, titanium diisopropoxide bis(acetylacetone) (TiAcAc) was added to the NPs dispersion. Due to the chelation between acetylacetone ligands and the TiO₂ NPs, the original non-transparent dispersion became diaphanous. TiAcAc not only stabilized the NPs in the dispersion to prevent clusters but also could form TiO_x during the drying process to fill the gaps between NPs.^[48] As shown in Fig. 6(a, b), the TiO₂ film obtained by drying this dispersion at 150 °C was uniform and crack-free. The X-ray diffraction (XRD) spectrum in Fig. 6(c) demonstrated that

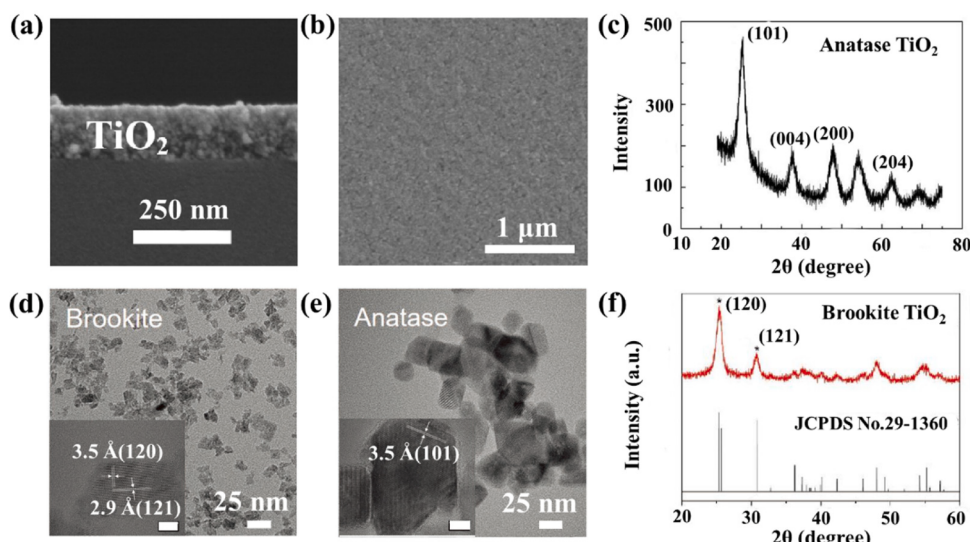


Fig. 6. SEM images of cross section (a) and top view (b) of compact layers prepared by TiO_2 NPs; (c) XRD of LT- TiO_2 compact layer.^[47] Copyright 2014, Royal Society of Chemistry. TEM and HRTEM (inset) images of (d) brookite LT- TiO_2 and (e) traditional anatase HT- TiO_2 scaffolds; (f) XRD of LT- TiO_2 mesoporous layer.^[51] Copyright 2017, Wiley-VCH.

the prepared LT- TiO_2 was anatase structure, and the diameter of the NPs was about 4.5 nm calculated from the peak width. Moreover, the addition of TiAcAc is conducive to the improvement of electronic property.^[49] The conductivity of the LT- TiO_2 ETM with small amount of TiAcAc is 100 times higher than that of TiO_2 deposited by high-temperature process. In addition to the TiO_2 compact layer, the mesoporous scaffold layer can also be acquired at relative low temperature through spin-coating method.^[50] A commercially available brookite colloid solution dissolving in organic solvent was used to prepare mesoporous LT- TiO_2 .^[51] Fig. 6(d,e) shows the transmission electron microscopic (TEM) and high-resolution TEM images (HRTEM) of brookite LT- TiO_2 and anatase TiO_2 deposited by high-temperature process. The anatase nanocrystals represented bipyramids shape with the size of 25 ~ 30 nm, while the brookite nanocrystals exhibited plate shape and smaller particle size ranging from 16 to 18 nm. Consistent with the HRTEM, the X-ray diffraction proved that the diffraction peaks match the orthorhombic structure of brookite TiO_2 , as shown in Fig. 6(f). The brookite LT- TiO_2 with small size formed denser mesoporous scaffold compared to conventional anatase counterparts, which offered excellent electron transport channels and contributed to efficient electron extraction.

(2) The low-temperature ZnO deposited by spin-coating

Spin-coating method is a most widely used solution processing strategy to deposit ZnO ETMs. The surface morphologies, thickness, crystallinity can be controlled by tuning the spin-coated gel and processing parameters. Initially, Kelly *et al.* employed ZnO nanoparticle solution and then spin coated on ITO substrate without high-temperature annealing treatment.^[24] The ZnO nanoparticles with approximate 5 nm in size were prepared by the hydrolysis of zinc acetate in methanol. Furthermore, the sol-gel method is also extensively used for fabrication of ZnO ETMs for PSCs.^[52,53] Although these two methods both require spin-coating and low-temperature post-annealing processes, the surface morphologies of resulting ZnO ETMs are different. Song *et al.* comprehensively compared sol-gel (SG) and hydrolysis-condensation (HC) methods under parallel conditions.^[54] The homogeneous transparent 2-methoxyethanol solution of zinc acetate dihydrate with equimolar ethanolamine was spin-coated on cleaned ITO and annealed to get a uniform planar SG-ZnO layer. On the other hand, nanocrystals suspension synthesized from zinc acetate dihydrate and methanol solution containing KOH replaced the precursor solution in

the preparation process was used to obtain HC-ZnO layer. The resulted ZnO ETMs have different surface morphologies, as shown in Fig. 7(a, b). Specifically, the SG-ZnO has ripple-like surface structure. While the surface of HC-ZnO is flat. The surface structure is related to the crystallinity and morphology of subsequent perovskite layer. The perovskite deposited on HC-ZnO has less pinholes than that of the perovskite on SG-ZnO ETM. Moreover, the conductivity and charge-transportation ability are also different. As demonstrated in Fig. 7(c), the I-V curve of HC-ZnO had a larger slope than that of SG-ZnO, which meant a better conductivity. The average charge mobilities of perovskite on HC-ZnO ($0.34 \pm 0.02 \text{ cm}^2 \text{ V}^{-1} \text{ S}^{-1}$) is larger than that of the perovskite on SG-ZnO ($0.25 \pm 0.02 \text{ cm}^2 \text{ V}^{-1} \text{ S}^{-1}$), according to the space-charge limited current model analysis in Fig. 7(d). The steady-state and transient photoluminescence (PL) were also proposed to investigate the charge extraction ability of such ZnO films as shown in Fig. 7(e, f). The lower PL intensity and shorter carrier lifetime of ITO/HC-ZnO/perovskite indicated the more efficient extraction of electrons from perovskite compared with ITO/SG-ZnO/perovskite. All of above discussions confirm that HC method is better than SG method to prepare the high-quality ZnO ETMs, which, meanwhile, reflects the important influence of the preparation technology on the properties of the ZnO ETMs and the target device.

There is no doubt that the spin-coating method is one of the simple and low-cost film deposition strategy. It is suitable for both rigid and flexible substrates. The thickness and particle size of the ZnO film can be controlled by adjusting the spin procedures and spin-coated gel. However, ZnO ETM prepared by spin-coating process always have the problem of poor coverage and many defects, which need to be further improved.

(3) The low-temperature SnO_2 deposited by spin-coating

The solution spin-coating method is the most extensively proposed strategy to fabricate highly crystalline SnO_2 ETMs, which has the advantages of simple operation and low cost. It always uses two types of deposition precursors, namely tin salt and tin oxide colloid. Specifically, SnCl_2 , SnCl_4 or corresponding hydrate were usually selected as tin salts, which can be dissolved directly with an organic solvent, then spin-coated and annealed at low temperature.^[55] In order to acquire the high-quality SnO_2 ETMs, it is worth noticing that the moisture atmosphere and UV-Ozone treatment are necessary and the suitable

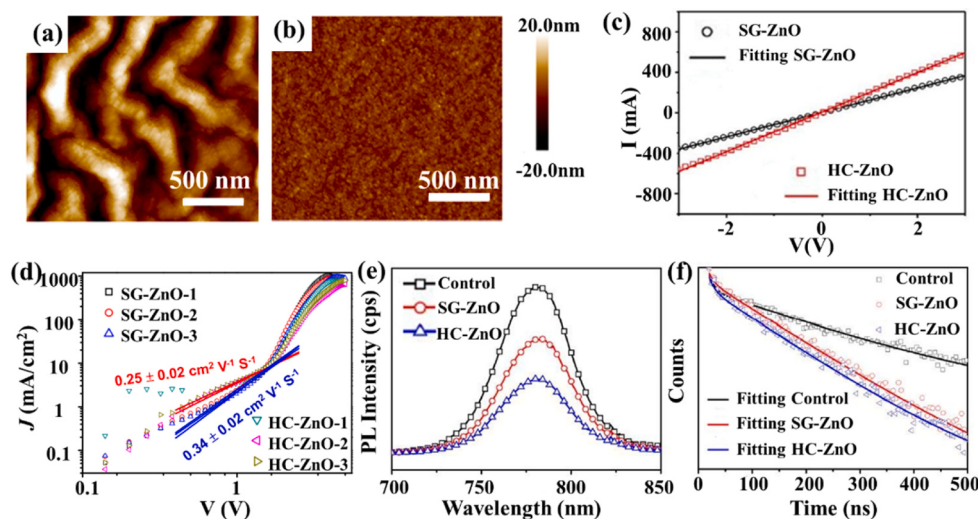


Fig. 7. The atomic force microscopy (AFM) images of (a) SG-ZnO ETM and (b) HC-ZnO ETM; (c) I-V curves of ITO/ZnO/Ag structures; (d) J-V curves of ITO/ZnO/perovskite/PCBM/Li/Al structures; (e) Steady-state and (f) transient-state PL spectra of perovskite on ITO (control), SG-ZnO and SG-ZnO ETMs.^[54] Copyright 2017, American Chemical Society.

annealing temperature < 200 °C should be guaranteed. In 2015, $\text{SnCl}_2 \cdot 2\text{H}_2\text{O}$ was firstly applied by dissolving it in ethanol as precursor.^[56] And then the solution was spin-coated onto substrates and annealed at 180 °C in air for an hour. The SnO_2 coated FTO glass exhibited enhanced light transmission property, possibly because of the reduced roughness of FTO. In addition to thermal annealing treatment, the plasma energy was first employed to activate the sol-gel film to form SnO_2 films.^[57] The Ar/O₂ plasma treatment under a lower temperature of ~ 50 °C gave rise to fully oxidized SnO_2 film with metal–oxygen–metal backbones. To further qualify the superiority of plasma treatment, thermal annealing was also employed to prepare the control samples. As shown in Fig. 8(a), Jang *et al.* firstly spin-coated the SnCl_2 ethanol solution onto the FTO substrate. Then annealing and plasma treatment are separately conducted to form SnO_2 films. Particularly, the annealing treatment was carried out at 180 °C for one hour. And the plasma method needs to set the plasma power as 180 W and treated with Ar/O₂

gas stream for 5 min. There were no significant differences in the composition and morphology, as well as the light transmission property and band gap between above two SnO_2 films as verified by SEM and transmittance spectra. However, the Tafel and J-V curves of the two films indicated that the plasma-treated SnO_2 had higher conductivity and carrier mobility. This phenomenon can be attributed to the reduction of the hydroxyl in plasma-treated SnO_2 . Because the hydroxyl residue in the annealed film seriously impeded the electron transport and decreased the mobility. The XPS analysis further proved the decrease in hydroxyl groups on plasma-treated SnO_2 film. Besides, the tin salt was also applied to prepare SnO_2 NPs or quantum dot (QD). In 2018, Fang *et al.* used $\text{SnCl}_2 \cdot 2\text{H}_2\text{O}$ and $\text{CH}_4\text{N}_2\text{S}$ to prepare SnO_2 QD solution.^[58] After hydrolysis, dehydration and oxidation process, the mixed solution converted to a yellow SnO_2 QD solution within one day. The functional group such as an amino group of thiourea can promote the formation of sulfur to metal bond, and the aggregation of SnO_2 QD can be suppressed

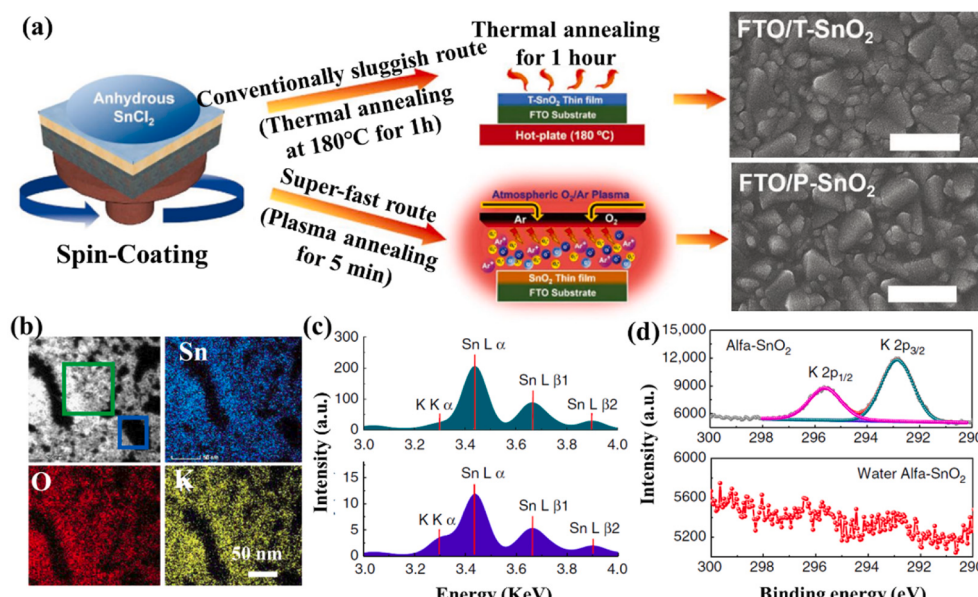


Fig. 8. (a) Schematic diagrams of SnO_2 preparation processes and corresponding SEM images of the films, the upper row is thermal annealed (T-SnO_2), and the lower row is plasma treated (P-SnO_2).^[57] Copyright 2018, Wiley-VCH. (b) The STEM-EDX images and (c) the corresponding EDX spectra of commercial SnO_2 ; (d) The XPS spectra of different SnO_2 films.^[60] Copyright 2018, Springer Nature.

by the protonated amino group. Thus, above SnO_2 QD solution is very stable and can even be stored for months. The spin-coated SnO_2 film based on above QD solution was uniformly and densely covered the FTO surface. The carrier concentration and the electrical conductivity can be tuned by changing the thermal annealing temperature.

In addition to tin slat, SnO_2 colloid solution is another good choice to synthesis SnO_2 films. You et al. purchased the SnO_2 colloid solution from Alfa and simply spin-coated on substrates, following annealing at 150 °C for 30 min to obtain a dense SnO_2 film.^[59] This commercial SnO_2 colloid is highly crystalline and has a uniform particle size of 3–4 nm, which facilitates the formation of uniform film with good electrical conductivity. The crystal structure and composition of SnO_2 colloid solution were also investigated. The electron diffraction rings and the XRD peaks are corresponding to the SnO_2 tetragonal structure. The XPS analysis indicated the single Sn^{4+} chemical state in the SnO_2 . Obviously, the preparation process by using SnO_2 colloid solution is simple and repeatable. However, there is a lack of understanding of the characteristics and preparation details of such commercial SnO_2 colloid. Cheng analyzed the purchased colloids and found that it has strong basicity with pH value of 12.^[60] To analyze the elemental composition and distribution of Alfa- SnO_2 , the scanning transmission electron microscopy and energy dispersive X-ray spectroscopy (STEM-EDX) were employed as shown in Fig. 8(b,c). It clearly demonstrated the presence of potassium ions and further detailed verified the position of K-rich phase. Therefore, researchers concluded that KOH was added to improve the stability of the colloid. Interestingly, the XPS peak of K ion disappeared after washing the coated SnO_2 film with deionized water, which indicated that K ion mainly existed on the surface of the sintered SnO_2 film instead of the crystal lattices. Thus, the modified SnO_2 by KOH demonstrated the similar effect compared with the Alfa- SnO_2 . The PSCs based on SnO_2 ETMs prepared by homemade SnO_2 colloid indeed achieved the hysteresis-free high performance. On this basis, this modified SnO_2 film was also applied to the ITO/PEN flexible substrate with large area of 5 × 6 cm², which further proves the reliability and universality of this strategy as well as solidifies the prospects for future applications.

(4) The low-temperature organic ETMs deposited by spin-coating

Organic ETMs exhibit excellent solubility in various organic solvents, making them suitable for solution processing technology. Specifically, the PFN-2TNDI ETM with excellent electronic properties was spin coated onto perovskite layer.^[43] The effect of coating thickness on the device performance was also evaluated. The optimal thickness of ETM is between 50 and 100 nm, and the average PCE is greater than 15 %. When the thickness is less than 50 nm or greater than 100 nm, the PCE decreases slightly. Even with a thick ETM of 200 nm, the average PCE remained above 14 %. These results show that a wide range of thicknesses of the PFN-2TNDI can be applied to produce highly efficient devices owing to the good electron transport property of the polymer, which provides a more favorable processing window for potential fabrication of PSCs using large-area coating method. Moreover, Choi et al. developed a composite ETM by combining nTi-MOF and PCBM. Initially, the nTi-MOF was synthesized and deposited onto the substrate, followed by spin-coating of PCBM to enhance conductivity and prevent direct contact between the perovskite and substrates. These composites ETMs exhibited exceptional device performance in both rigid (PCE = 18.94 %) and flexible (PCE = 17.43 %) PSC architectures. Recently, Chen et al. spin-coated a chlorobenzene solution of PCBM on top of the FA_{0.98}Cs_{0.02}PbI₃ perovskite films. This inverted PSCs achieved 25.1 % efficiency and improved stability.^[61] He et al. coated the PC61BM on the perovskite layer and constructed a highly efficient inverted PSC with PCE of 25.39 %.^[42]

3.1.2. Hydrothermal growth method

Hydrothermal growth method is the most commonly used to synthesize and grow nanomaterials with nanostructures, such as nanorod

arrays, under specific temperatures and pressures. ZnO nanorod arrays (ZnO NAs) with large surface area and direct electron transport pathway have been widely used in PSCs. Hydrothermal method is the main method to fabricate ZnO NAs. The basic growth principle is the reaction of Zn salt and alkali in the solution. Subsequently, the reaction product Zn(OH)_2 gradually decomposed and dehydrated to form ZnO as temperature and pressure increased.^[62] Similarly the regulation of the composition and concentration, as well as reaction temperature and time could optimize the morphology of ZnO NAs. Park et al. constructed the PSCs based on ZnO NAs prepared by dissolving equimolar zinc nitrate hexahydrate and hexamethylenetetramine.^[63] By tuning the precursor concentration from 20 to 35 mM, the average diameter of the ZnO NAs increased from 54 nm to 61, 73, and 82 nm, as shown in Fig. 9(a). The length of ZnO NAs was also tuned by changing the reaction time, as shown in Fig. 9(b). With the extended immersion time from 90 to 180 min, the average length of ZnO nanorods increased from 440 nm to 620 nm, 820 nm and 1 μm. The ZnO nanorods with high orientation were vertically grown on the substrate. Compared with the ZnO films, one-dimensional single crystal nanorods with excellent electronic transmission capability can significantly alleviate carrier recombination problem. The PSCs based on the long ZnO NAs demonstrated high photocurrent and external quantum efficiency.

Moreover, patterned ZnO NAs have more discrete three-dimensional structure and larger specific surface area, which is beneficial to improve the filling degree of perovskite and improve the light capture ability. Various of strategies have been developed to fabricate the patented ZnO NAs. Among them, optical lithography (OL) and laser interference lithography (LIL) techniques could realize the precisely growth of the ZnO NAs.^[64] The detailed fabrication process of OL method is shown in Fig. 9(c). Specifically, the ZnO seed layer and photoresist (PR) layer are spin-coated on the substrate, respectively. After UV exposure, the geometric pattern of photomask successfully transfers to the PR layer. Then, ZnO NAs are synthetized on the patterned substrate. Finally, the rest PR material is removed and patterned ZnO NAs are prepared. Different from OL, the pattern in LIL method comes from laser interference instead of photomask. PR material can be easily removed at high light intensity. Therefore, regular interference pattern is recorded in the light-sensitive substrates. The interference of three laser beams results in periodic variation of light intensity and induces hexagonal interference pattern on the substrate. The three-beam laser interference lithography (3BLIL) system is illustrated in Fig. 9(d). The shape, diameter, period and distribution of the patterns are also tunable by simply changing the exposure parameters. The patterned ZnO NAs with different period are shown in Fig. 9(e). Generally, the propagation properties of light in ZnO NAs are dependent on the period, size of the nanorods. For instance, the light absorption ability of ZnO NAs with square pattern is significantly higher than that of no-pattern and line-patterned ZnO NAs. Therefore, the highly controllable patterned ZnO NAs with period distribution have a wide application prospect in PSCs.

3.1.3. Chemical bath deposition method

Chemical bath deposition (CBD) is another widely used liquid deposition method.^[65] Chemical bath deposition for film formation is governed by two critical steps, namely, nucleation and particle growth, which is developed for the preparation of oxide films. TiCl_4 was commonly used to form rutile phase TiO_2 nanocrystals at 70 °C via CBD. The film thickness can be adjusted by changing the concentration of TiCl_4 , ranging from 10 nm to several micrometers. Besides, the TiCl_4 precursor solution can be wrapped between preheated substrate and the soft film. It creates a closed environment for hydrolysis and eventually synthesized a uniform and dense large-area TiO_2 film at a low temperature of 75 °C.

In addition, chemical bath deposition method has also been used to prepare SnO_2 ETMs. Correa-Baena and co-workers used a simple, solution-processed method by combining spin-coating and CBD technique to deposit SnO_2 ETMs.^[66] Particularly, the $\text{SnCl}_2 \cdot 2\text{H}_2\text{O}$ was

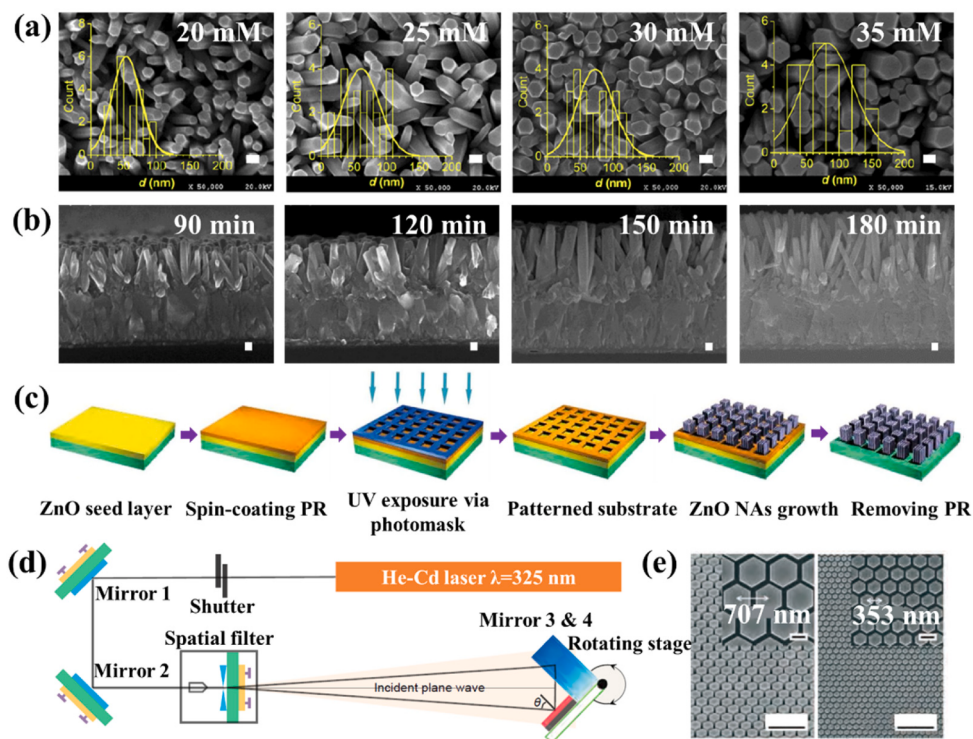


Fig. 9. (a) Surface and (b) cross-sectional SEM images of ZnO NAs grown at different concentration and for different time.^[63] Copyright 2014, American Chemical Society. (c) Diagram of patterned ZnO NAs fabrication by OL method. (d) Diagram of the three-beam interferometer system. (e) SEM images ZnO NAs by 3BLIL technique with different period (Scale bar: 2 μ m), (Inset is the magnified images with scale bar of 300 nm).^[64] Copyright 2017, Springer Nature.

dissolved in aqueous solution mixed with thioglycolic acid, urea and HCl. Then the substrate was immersed in the above solution and deposited in an oven at 70 °C for 3 h. Subsequently, the deposited film was rinsed with deionized water and then annealed at 180 °C. As a result, the SnO₂ ETMs with denser surface topography were obtained. Although this method can effectively improve the surface quality, it is more complicated in the preparation process.

3.1.4. Electrodeposition method

The electrodeposition method is simple and various thin films with grain size between 1 and 100 nm can be obtained. Specifically, electrodeposition is an effective liquid deposition approach to obtain the TiO₂ ETMs at low temperature. Wei *et al.* selected the TiCl₃ aqueous solution to fabricate the TiO₂ ETMs and ingeniously tuned the pH according to the substrate.^[51] The three-electrode electrochemical system was built. The cleaned FTO glass, platinum plate and Ag/AgCl were used as the working electrode, counter electrode, and reference electrode, respectively. Generally, for FTO glass substrates, the pH is controlled to be about 2.5 by continuously titrating Na₂CO₃. For ITO/PEN substrates, it is necessary to control the pH to ~ 4.8 to prevent the corrosion. At the same time, the solubility of TiCl₃ at high pH is improved by the chelation of ethylenediaminetetraacetic acid. Moreover, a stream of nitrogen was continuously introduced into the solution to prevent oxidation of Ti³⁺. The deposition morphology of TiO₂ can be controlled by varying the current density and deposition time. The XRD patterns proved that the electrodeposited TiO₂ was amorphous. The Mott-Schottky analysis indicated that the electrodeposited TiO₂ exhibited lower potential and higher carrier concentration, which facilitated unidirectional charge transport from TiO_x to FTO or ITO. In addition, the hole blocking effect was characterized by cyclic voltammetry. The redox reaction voltammogram of Fe³⁺ and Fe²⁺ was used to simulate charge recombination. The high response of bare FTO showed that it had no inhibitory effect on redox reaction. The shrunk and deformed CV waves of electrodeposited TiO₂ indicated the high blocking

ability. Moreover, an electrochemical deposition method was utilized to prepare SnO₂ ETMs at low temperature about 50 °C. It demonstrated good adhesion and the surface nanostructures can be effectively controlled.^[67]

3.2. Vapor-processed low-temperature ETMs

Vapor-based methods have also been demonstrated as a promising route for the fabrication of low-temperature ETMs. It has high repeatability and the potential of large-scale fabrication. In addition to uniform film formation across large areas, there are also other unique advantages for vapor-based processes compared with solution-processed strategies, such as easy formation of films and conformal coating in textured-structured substrate. Although more and more research work on vapor-based processes for low-temperature ETMs have emerged, the number of works focusing on vapor-process is still small compared to that of the works focusing on solution-based methods. Furthermore, only a very few works have been published in applying vapor-based methods in perovskite solar modules with larger areas.

3.2.1. Atomic layer deposition method

ALD technique, derived from chemical vapor deposition, is frequently used to prepare high-quality electron-transporting films at low temperatures due to the highly reactive nature of ALD precursors. The inherent self-limiting nature of the ALD process can provide high uniformity and conformality over large areas and rough/complex surfaces, with precise control over the thicknesses down to the monolayer level. Generally, one whole cycle of ALD consists of four steps: i the injection of precursor A and formation of single molecule film on substrate by chemical absorption; ii sweep of unreacted precursor by carrier gas; iii the injection of precursor B and reaction with the absorbed precursor A in process i; iv sweep of excess precursor and reaction by-products by carrier gas.^[68] After one deposition cycle, only a single molecule film could be obtained because of the restriction of chemical

absorption. Hence, the thickness and quality of films deposited by ALD technique could be precisely controlled with high surface coverage.

The ALD method has been regarded as a promising approach for preparing the ZnO film at relatively low temperature. Several groups proposed this deposition technique to produce ultrathin, compact, high-quality low-temperature ZnO ETMs. As early as 2016, Zhang *et al.* used ALD technique to deposit dense ZnO film as ETM in PSCs.^[20] The detailed fabrication process was illustrated in Fig. 10(a). Diethyl zinc (DEZ) and water vapor were injected into the reaction chamber in turn. Zinc atoms bonded with oxygen atoms in hydroxyl groups on the substrate. Two ethyl groups react with hydrogen atoms successively to form ethane. Finally, a single layer of zinc oxide films with hydroxyl groups formed.^[22] The process will go on in circles, until the final thickness is obtained. To investigate the surface morphology, the SEM images of both ALD-ZnO and spin-coated ZnO were illustrated in Fig. 10(d). ZnO film deposited by ALD was more homogeneous and flatter than spin-coated ZnO. The ALD-ZnO could precisely follow the surface shape of FTO substrate. While the spin-coated ZnO film looked rough and had many clusters and pin-holes, which acted as recombination path and was detrimental to charge transportation. The surface roughness was also quantized by AFM, as shown in Fig. 10(e). The ZnO film deposited by spin-coating has a high roughness of 23.3 nm, which is twice that of ALD-ZnO. The dense ZnO film with high quality benefits from ALD technique. Specifically, the reaction occurs only in the presence of exposed surface groups and the excess precursors as well as by-products will be taken away after reaction. It makes sure the precise deposition layer by layer and ensures the uniformity of the film. Moreover, Wu *et al.* fabricated the ZnO ETM with different thickness (5–40 nm) by tuning the ALD deposition cycles.^[69] The electron mobility of ZnO was dependent on film thickness as calculated by hall measurement. The thicker film owned the higher electron mobility. However, the series

resistance increased, once the thickness exceeds 30 nm. ALD method could accurately control the thickness of ZnO ETM, which is beneficial to optimize the performance of PSCs. Nowadays, ALD technique has been used to deposit ZnO ETM in PSCs with both p-i-n and n-i-p architectures below or on top of the perovskite absorber layer.^[70] However, the low deposition rate restricts the implementation in large-scale production. Hence an atmospheric ALD method which allowed the deposition of ZnO layers in ambient atmosphere was developed. This technique realizes the precursors separation in space rather than time.^[71] The reaction zones of different precursors are separated by gas bearings and the moving substrate enables the exposure to each precursor, as shown in Fig. 10(b,c). The atmospheric ALD could combine the advantages of conventional ALD (e.g. high flatness, dense, pin-hole free) and compatibility of flexible substrates as well as rapid deposition. For this reason, atmospheric ALD method has been proposed as an innovative film deposition technique and shows the potential application promise in large-scale flexible PSCs.

The ALD as a widely used conformal growth technology has also been proposed to prepare low-temperature SnO₂ with high quality. Due to the self-limiting reactions of ALD, the surface of SnO₂ ETMs are always dense, smooth and pinhole-free. The ALD-SnO₂ usually need thermal or plasma treatment. As for thermal ALD, Sn(NC₂H₆)₄ is the mostly used precursor and ozone treatment is carried out to obtain a SnO₂ film at 118 °C. While, plasma-enhanced atomic layer deposition (PEALD) uses the same precursor but the deposition temperature is below 100 °C. To lowering the processing temperature, Prof. Yan *et al.* employed PEALD to deposit SnO₂ ETM.^[72] The film demonstrated high coverage and exhibit higher light transmission performance than bare FTO. However, the conductivity of SnO₂ prepared by this low temperature method is inferior. They further proposed facile post-annealing method to optimize the material conductivity.^[73] Both the electrical

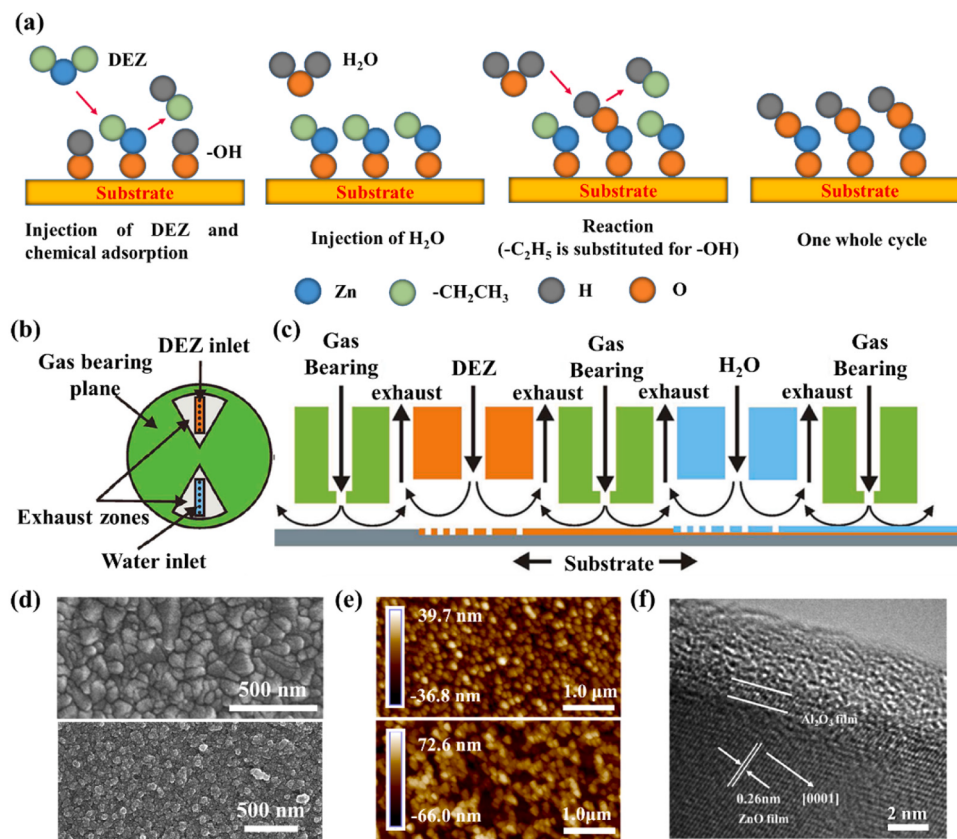


Fig. 10. (a) Schematic illustration of the fabrication of ALD-ZnO film.^[22] (b) The schematic of the atmospheric ALD reactor head and (c) the fabrication process based on atmospheric ALD.^[71] Copyright 2012, American Chemical Society. (d) SEM images of ALD-ZnO film (above) and spin-coated ZnO (below). (e) AFM images of ALD-ZnO film (above) and spin-coated ZnO (below). (f) HRTEM image of ALD-ZnO. ^[20] Copyright 2016, Elsevier.

conductivity and carrier mobility gradually increased after annealing treatment as shown in Fig. 11(a, b). Further analysis shows that the post-annealing process efficiently improved the crystallinity and ordering of SnO_2 . The surface defects such as voids were also eliminated which enhanced the optical absorption and increased the band gap as illustrated in Fig. 11(c). This post-treatment is critical for modification of the quality, but the deposition temperature is increased compared to PEALD. Subsequently, Nazeeruddin et al. fabricated the ALD- SnO_2 ETMs with enhanced photo-electrochemical properties by $\text{Sn}(\text{NC}_2\text{H}_6)_4$ self-passivation and post-annealing.^[74] The reaction process of ALD is shown in Fig. 11(e). To realize the complete reaction, Sn-N bond was broken and then react with O_2 to form SnO_2 . While the residual Sn precursor coexist with SnO_2 and passivate the surface defects. As shown in Fig. 11(d), the ALD- SnO_2 is homogeneous and compact. To investigate the influence of thermal treatment, tip-enhanced Raman spectroscopy (TERS) was applied. The Raman spectra in Fig. 11(f) demonstrated that the peak intensity become stronger with the increased temperature from 100 °C to 300 °C. This indicated an enhanced crystallization and orientation. The bandgap also changed after post-annealing as verified by reflection electron energy loss spectroscopy. As shown in Fig. 11(g, h), the bandgap decreased from 4.38 eV to 4.33 eV and 3.93 eV for the as-deposited, 180, and 300 °C films, respectively. All of deeply analysis implied the importance of surface passivation and post-treatment for low-temperature processed ALD- SnO_2 ETMs. Meanwhile, it is necessary to continuous optimize the ALD technology for preparation of highly crystalline SnO_2 ETMs.

The ALD technique has also been used to deposited low-temperature TiO_2 . Compared to the spin-coating method, ALD is more elaborate deposition technique, which fulfills the requirement of PSCs on highly crystalline ETMs. Chandiran et al. successfully deposited conformal pin-hole free TiO_2 layer with the thickness ranging from 0 to 4 nm to block the charge recombination, as shown in Fig. 12(a). Such sub-nanometer layer was deposited by ALD at a low temperature of 120 °C from tetrakis

(dimethylamido)titanium(IV) and deionized water precursors.^[75] To further improve the film quality, PEALD was applied to form the low-temperature TiO_2 ETMs.^[8] The titanium(IV) isopropoxide (TTIP) and high-purity O_2 were Ti source and oxygen source, respectively. The conventional solution-processed TiO_2 ETMs were also prepared by using ethanal-based TTIP solution (ET- TiO_2) and butanol-based TTIP solution (BT- TiO_2). The Fourier transform infrared (FTIR) and X-ray photoelectron (XPS) spectra were employed to analyze the surface defects and compounds, as shown in Fig. 12(d-e). Both of the ET- TiO_2 and BT- TiO_2 had organic residues as verified by the signal of O-H and C-H. While the low-temperature TiO_2 deposited by ALD shows no residual species. The non-stoichiometric point defects were negligible in LT- TiO_2 , but the solution-processed TiO_2 films contained lots of Ti^{3+} ions and hydroxyl groups. These residues and defects are deleterious to the charge injection and transport. This in turns reflects the superiority of ALD technique.

3.2.2. Magnetron sputtering method

Magnetron sputtering technique is another mature physical deposition-based approach that has a fast deposition rate and the deposited films often show a good uniformity and high binding force with the substrate. Additionally, this technology is easy to achieve industrial production. Currently, the magnetron sputtering technique as an easy-control, physical deposition-based approach, was proposed to fabricate high-quality TiO_2 ETM at low temperature.^[76] Song et al. prepared compact TiO_2 layer upon either FTO/Glass or ITO/PEN substrates by RF magnetron sputtering technique.^[77] The thickness of the film can be controlled by deposition time. With the deposition time extended to 30 min, the surface of the TiO_2 gradually becomes uniform and dense. AFM can realize a real-space visualization of topography coupled with optoelectronic properties on a microscopic scale.^[78] The surface properties of TiO_2 film deposited at different time was investigated by AFM. Notable, the atoms are closely packed along the contour

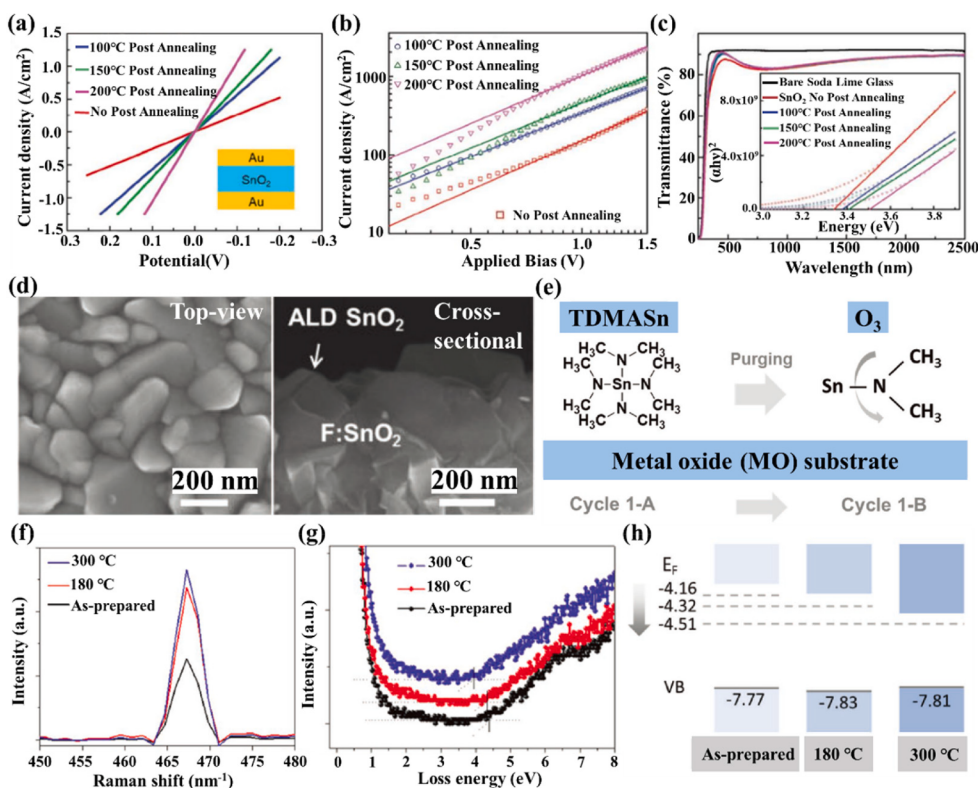


Fig. 11. (a) J-V curves and (b) SCLC curves of PEALD- SnO_2 ; (c) Transmittance and absorption spectra (inset) of different PEALD- SnO_2 .^[73] Copyright 2017, Wiley-VCH. (d) SEM images of ALD- SnO_2 ; (e) Schematic of ALD; (f) TERS spectra; (g) Valence band edge teste; (h) Schematic diagram of band structure.^[74] Copyright 2018, Wiley-VCH.

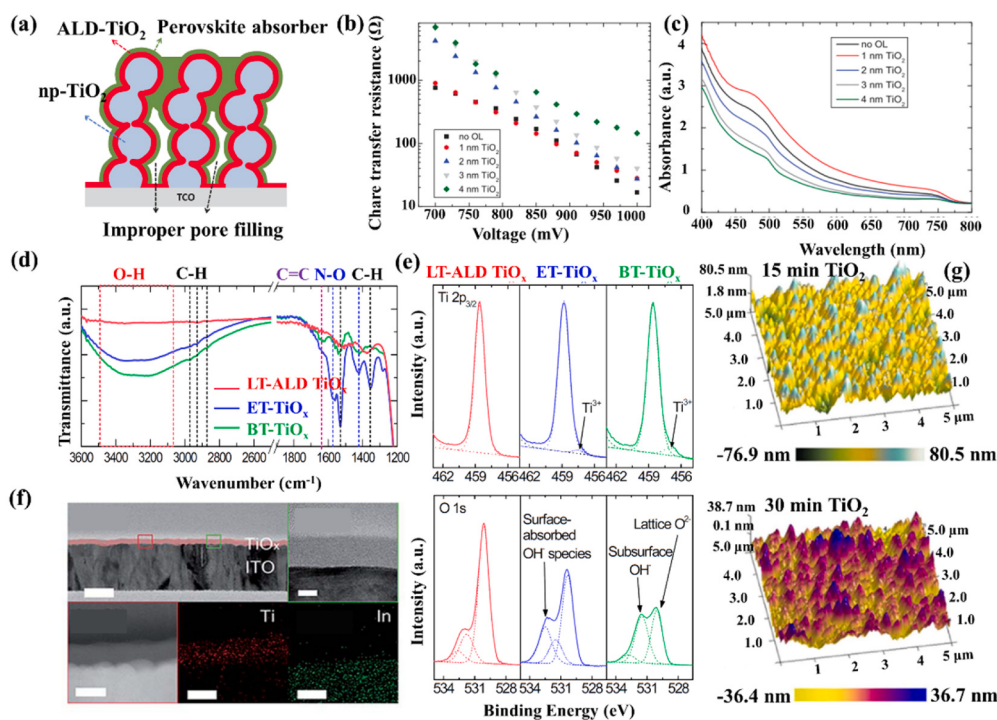


Fig. 12. (a) The diagram of mesoscopic scaffold with ALD-TiO₂, (b) the charge transfer resistance for PSCs with or without ALD-TiO₂, (c) the absorption spectra of perovskite/ETM with different thickness of ALD-TiO₂.^[75] Copyright 2014, Wiley-VCH. (d) FTIR and (e) XPS spectra of LT-ALD TiO₂, ET-TiO₂ and BT-TiO₂. (f) The cross-sectional TEM and EDS images of ALD-TiO₂ (scale bar: 100 nm).^[8] Copyright 2015, Royal Society of Chemistry. (g) AFM images of the surface of TiO₂ on FTO with different deposition time.^[77] Copyright 2015, Springer Nature.

of the substrate, thus maintaining the morphology of the FTO surface. While, the roughness is gradually relieved with the extension of deposition time. The film thickness is uniform and completely covered so that the film surface can achieve good contact with perovskite.

3.2.3. Pulsed laser deposition method

While pulsed laser deposition requires the use of a focused laser pulse to a given target material, resulting in an ablative species of supersonic jet, which then condenses on the substrate. Several parameters such as substrate temperature, laser power, and gas pressure in the chamber influence the ETM film quality and its growth rate. Thus, although this technique has been studied extensively in the laboratory, it is only slowly emerging for industrial applications. Currently, only few researches used pulsed laser deposition technology to deposit low-temperature ETMs, due to the various challenges. However, this conceptually versatile and straightforward technique, applicable even to perovskite deposition, may be cost-effective and ideal for mass production, opening new avenues for translational research. Prof. Fang proposed pulsed laser deposition technique to fabricate SnO₂ at room temperature without any annealing process and demonstrated a 17.29 % PCE on glass and 14 % on flexible substrates.^[79]

3.2.4. Thermal evaporation method

Thermal evaporation is the most widely employed physical vapor deposition technique, in which the raw materials are subjected to thermal heating, resulting in their vaporization and subsequent deposition onto a substrate under vacuum conditions.^[80] C₆₀ and its derivatives as the most widely-used ETMs in n-i-p and p-i-n type PSCs can be deposited by thermal evaporation. In early 2016, Bolink et al. utilized the thermal evaporation method to deposit a double layer of 10 nm C₆₀ and 40 nm C₆₀-PhIm as ETMs. These evaporated ETMs exhibit high conductivity and excellent band alignment, resulting in solar cells with an impressive efficiency of 16.5 %.^[81] The same research group subsequently evaporated a 10 nm C₆₀ interlayer on TiO₂ ETM to mitigate

leakage current and interfacial recombination, resulting in an impressive PCE of 20.8 %.^[82] Recently, Luther et al. utilized a 25 nm thick C₆₀ film deposited via thermal evaporation as the ETM in PSCs, resulting in a PEC of 24.5 %.^[83] Jen et al. also utilized the evaporated C₆₀ as the ETMs of PSCs. This solar cell eventually realized a remarkable efficiency of 24.8 %.^[84] The continuous improvement in the efficiency of PSCs based on thermally evaporated organic ETMs confirms the feasibility and extensibility of thermal evaporation techniques for ETM deposition.

3.2.5. E-beam evaporation method

E-beam evaporation is a related high vacuum process with high material utilization efficiency. Fang et al. fabricated uniform SnO₂ film with low-cost and large-scale e-beam evaporation manufacture technology.^[85] The SnO₂ particles converted to evaporation under the electron beam and then condensed into a compact film on the substrates. This method can obtain over hundreds of SnO₂ ETMs at one time with desired repeatability. However, it always takes a lot of time to deposit high quality SnO₂ with suitable thickness. Although this technology offers relatively high deposition rates, it is generally difficult to control materials composition precisely. Also, X-ray damage on the substrate and low processing rates due to the need for high vacuum are drawbacks of the technique. Currently, there have been some demonstrations employing vapor-processing to deposit low-temperature ETMs. The PCE values of PSCs constructed by low-temperature ETMs prepared by various processing methods are summarized in Table 2.

3.3. Discussion and perspective

To shed light on the current advancements in synthetic strategy improvement and novel synthetic strategy development, a comprehensive analysis and comparative evaluation of cutting-edge synthetic strategies for low-temperature ETMs are specifically presented in Fig. 13. The most commonly used method for depositing ETMs is spin

Table 2

Non-exhaustive survey of preparation methods for low-temperature ETMs.

ETMs	Preparation method	Preparation temperature [°C]	Perovskite layer	V _{oc} [V]	J _{sc} [mA cm ⁻²]	FF [%]	PCE [%]	Ref.
TiO ₂	Spin-coating	120	MAPbI ₃	1.02	18.77	78	14.82	[86]
	Spin-coating	150	MAPbI ₃	1.07	19.51	75	15.76	[51]
	Spin-coating	150	MAPbI _{3-x} Cl _x	1.02	21.5	71	15.9	[47]
	Spin-coating	150	MAPbI _{3-x} Cl _x	1.13	22.75	75.01	19.3	[87]
	Spin-coating	150	FA _{0.85} MA _{0.15} PbI _{2.55} Br _{0.45}	1.17	21.7	79.4	20.1	[88]
	ALD	120	MAPbI ₃	0.969	17.64	67	11.5	[75]
	ALD	80	MAPbI _{3-x} Cl _x	0.95	21.4	60	12.2	[8]
	Magnetron sputtering	RT	MAPbI ₃	1.09	20.6	54	12.1	[77]
	Magnetron sputtering	RT	MAPbI _{3-x} Cl _x	1.03	20.90	70	15.07	[76]
	Magnetron sputtering	RT	MAPbI ₃	1.047	24.19	68.13	17.25	[89]
	Chemical bath deposition	70	MAPbI ₃	1.11	17.41	65.6	13.03	[65]
	Spin-coating	100	MAPbI _{3-x} Cl _x	0.97	21.57	61.9	12.9	[54]
	Spin-coating	60	MAPbI ₃	1.01	21.0	76.0	16.1	[90]
ZnO	Spin-coating	65	MAPbI ₃	1.03	20.4	74.9	15.7	[24]
	Spin-coating	150	MAPbI ₃	1.13	20.1	78	17.7	[91]
	Spin-coating	160	MAPbI ₃	1.08	19.83	38.5	8.25	[52]
	Spin-coating	160	MAPbI ₃	0.99	19.12	63	11.96	[53]
	ALD	70	MAPbI ₃	0.976	20.4	66	13.1	[92]
	ALD	150	MAPbI ₃	1.01	18.90	62	15.55	[20]
	ALD	80	MAPbI ₃	1.03	20.75	77.03	16.5	[93]
	Hydrothermal	90	MAPbI ₃	0.928	18.0	62	10.35	[94]
	Hydrothermal	180	MAPbI ₃	0.965	21.7	70	16.19	[95]
	Hydrothermal	90	MAPbI ₃	0.99	22.7	68	15.3	[96]
	Hydrothermal	90	MAPbI ₃	1.07	20.9	77.58	17.3	[97]
	Chemical bath deposition	90	MAPbI ₃	1.02	16.98	51.11	8.90	[7]
	Electrodeposition	150	MAPbI ₃	0.91	22.6	52.9	10.91	[98]
SnO ₂	Magnetron sputtering	RT	MAPbI ₃	1	21.8	72.6	15.9	[99]
	Spin-coating	180	MAPbI ₃	1.11	23.27	67	17.21	[56]
	Spin-coating	150	MAPbI ₃	1.15	21.74	80.9	20.23	[55]
	Spin-coating	50	Cs _{0.056} FA _{0.76} MA _{0.15} PbI _{2.42} Br _{0.48}	1.147	20.03	77.4	19.56	[57]
	Spin-coating	200	Cs _{0.05} (MA _{0.17} FA _{0.83}) _{0.95} Pb(I _{0.83} Br _{0.17}) ₃	1.11	20.94	73	16.97	[58]
	Spin-coating	150	(FAPbI ₃) _x (MAPbBr ₃) _{1-x}	1.09	24.88	75.73	20.54	[59]
	PEALD	100	MA _{0.7} FA _{0.3} PbI ₃	1.131	22.69	79.53	20.41	[73]
	PEALD	100	MAPbI ₃	1.074	21.17	75.48	17.16	[72]
	ALD	100	(FAPbI ₃) _{0.85} (MAPbBr ₃) _{0.15}	1.13	22.67	78	20.03	[74]
	ALD	118	(FAPbI ₃) _{0.85} (MAPbBr ₃) _{0.15}	1.14	21.3	74	18.4	[100]
	ALD	180	MAPbI ₃	1.07	22.6	75.6	18.3	[101]
	CBD	55	MAPbI ₃	1.05	21.3	66.3	14.8	[102]
	CBD	180	FA _{0.83} MA _{0.17} Pb(I _{0.87} Br _{0.17}) ₃	1.14	22.07	75	18.8	[103]
WO _x	CBD	180	Cs/MA/FA perovskite	1.17	22.59	75	20.73	[66]
	E-beam evaporation	180	Cs ₅ (MA _{0.17} FA _{0.83}) ₉₅ Pb(I _{0.83} Br _{0.17}) ₃	1.095	22.75	73	18.2	[85]
	Electrodeposition	50	MAPbI ₃	1.08	19.75	65	13.88	[67]
	Print	100	MAPbI _{3-x} Cl _x	0.797	20.2	57	9.3	[104]
	Spin-coating	150	MAPbI _{3-x} Cl _x	0.71	21.77	58	8.99	[28]
CeO _x	Spin-coating	50	(FAPbI ₃) _{1-x} (MAPbBr ₃) _x	1.06	24.82	79.13	20.77	[31]
	Spin-coating	150	MAPbI ₃	1.04	21.93	62.79	14.32	[32]
Nb ₂ O ₅	Magnetron sputtering	RT	MAPbI ₃	1.04	22.9	72	17.1	[30]
Zn ₂ SnO ₄	E-beam evaporation	RT	MA _{2/6} FA _{4/6} Pb(Br _{1/6} I _{5/6}) ₃	1.06	24.69	71.1	18.59	[33]
	Spin-coating	RT	CsPbI ₂ Br	1.06	14.13	78.4	11.74	[34]
	Sputtering	200	(MA,FA)Pb(I,Br) ₃	1.10	21.8	63	15.1	[105]

Ref. reference, RT:room temperature.

coating. However, this method is generally limited to a scale of less than 10 cm and results in a significant waste of precursor ink (over 90 %) during the process. While modules can be fabricated by spin coating on a substrate area of up to about 10 cm × 10 cm, their efficiency is considerably lower compared to smaller-area counterparts. In spin coating, the thinning and smoothing of wet-solution films rely on continuous centrifugal force from spinning, which is challenging to replicate in scalable deposition processes. The hydrothermal growth method facilitates the synthesis of multi-dimensional nanostructures, allowing for convenient adjustment of their shape and size through a straightforward process. Previously, this approach was commonly employed to fabricate patterned ZnO and SnO₂ with diverse structures. However, this method is frequently associated with undesirable side effects due to their relatively lengthy growth cycles, posing challenges in terms of the separation and purification of reaction products. The chemical bath deposition technique is also a simple and cost-effective method for depositing high-quality films. However, the bath needs frequent replacement and generates a significant amount of solution

waste, making it unsuitable for large-scale fabrication. In addition to the commonly employed solution-phase deposition methods, thermal evaporation technology is extensively utilized for the fabrication of organic low-temperature ETM owing to its notable advantages including a high film deposition rate, minimal substrate damage, and exceptional purity of targeted films. However, it is not suitable for depositing ultra-thin layers with sub-nanometer control. The ALD technique is a self-limiting vapor deposition method that offers exceptional uniformity and conformality over large areas, precise control over thicknesses down to the monolayer level, and compatibility with rough or complex surfaces. However, it exhibits a low deposition rate and incurs high fabrication costs.

Scalable deposition methods for various ETMs with large-area and high-quality has become a research hotspot. Solution-based scalable deposition methods have the advantage of low cost, which is very important for the popularization and application of perovskite cell modules. It is worth mentioning that slot-die-coating is a proven method for a large-area thin-film deposition since this method enables uniform



Fig. 13. Summary of the main state-of-the-art synthetic strategies for low-temperature ETMs.

deposition of films with high yield, reproducibility, and adjustable film thickness. Consequently, it possesses significant potential for future application in roll-to-roll fabrication processes. Spray-coating is another industrially viable deposition route, combining a high fabrication speed and relatively low material consumption with high conformality. While the photovoltaic performance of device fabricated using spray coating is found to be inferior compared to those prepared by slot-die coating techniques, indicating the need for further understanding and development of the spray-coating method for large-area ETM coatings. Vapour-based deposition is a solvent-free process that has been studied for large-area low-temperature ETMs coatings. The magnetron sputtering technique exhibits a rapid deposition rate and is readily scalable for industrial production. Furthermore, the resulting deposited films demonstrate exceptional uniformity and high adhesion strength, which are crucial for ensuring the mechanical stability of flexible PSCs. Despite the potential of vapor-phase deposition for large-scale ETM deposition, these methods typically necessitate advanced vacuum equipment and prolonged processing times, potentially impeding their suitability for cost-effective fabrication of PSCs. Advancing our comprehension of the factors influencing thin-film formation and enhancing our ability to control thin-film formation in various deposition processes are pivotal for upscaling PSCs.

4. Optimization strategies of Low-Temperature ETMs

The properties of low-temperature ETMs are highly dependent on the processing methods and conditions. Some cryogenic processing methods or conditions could lead to the inferior-quality films. These will lead to poor device performance due to serious interface recombination and charge barriers. If so, modifications or post-treatments of low-temperature ETMs are necessary. To optimize the electron extraction and transport processes and also to enhance the device stability, low-temperature ETMs have always been further functionalized. In this chapter, we systematically discuss the universal optimization strategies

including element doping, surface modification, nanostructure management, bilayer engineering and strain regulation.

4.1. Element doping

Doping of metal oxides with alio/isovalent metal cations is an effective and proven method to regulate the electronic properties of inorganic materials, thereby reducing contact resistance and recombination at the ETM/perovskite interface, provided through an energy level modulation modification. As this results in enhanced PSC performance, this strategy has been extensively studied, as shown in Fig. 14. As for low-temperature processed ETMs, the inadequate conductivity and surface defects ineluctably induced the electron-hole recombination, charge accumulation or stability issues. So far, it has been observed that the introduction of impurities into target ETMs is conducive to get out above dilemma so as to fulfill the requirement of high-efficiency PSCs.

In particular, some shortcomings have been exposed in the long-term applications of TiO₂ ETMs. Its electron mobility is relatively lower than that of other ETMs, especially the holes transport materials. This drawback can cause unbalanced transportation between electrons and holes, resulting in recombination and efficiency loss. Some researchers have tried to use element doping method to improve the performance of the low-temperature TiO₂ based PSCs. For instance, Y-doping could enhance carrier concentration and improve carrier extraction and transport of TiO₂, thereby reducing the carrier recombination. On the basis, the PSCs based on Y-TiO₂ ETM acquired an enhanced efficiency of 19.3 %. [87] Recently, the cations of transition metal Co and Fe were selected to dope the TiO₂ ETM in inverted PSCs. [106] The nanoscopic feature of doped TiO₂ ETM was illustrated in Fig. 15(a). The metal doping could adjust optoelectronic properties without changing the crystal phase and physical dimensional feature. The composite of TiO₂ NAs filled with fullerene was used to construct inverted PSCs, as shown in Fig. 15(c). Such composite ETM exhibited superior surface

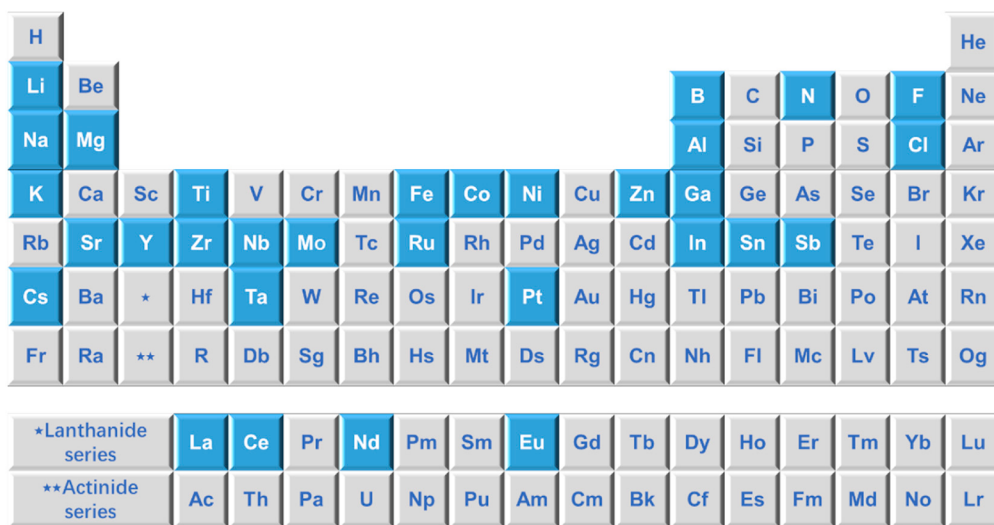


Fig. 14. Non-exhaustive summary of the elements in periodic table used as dopant in ETMs for PSCs (highlighted in blue).

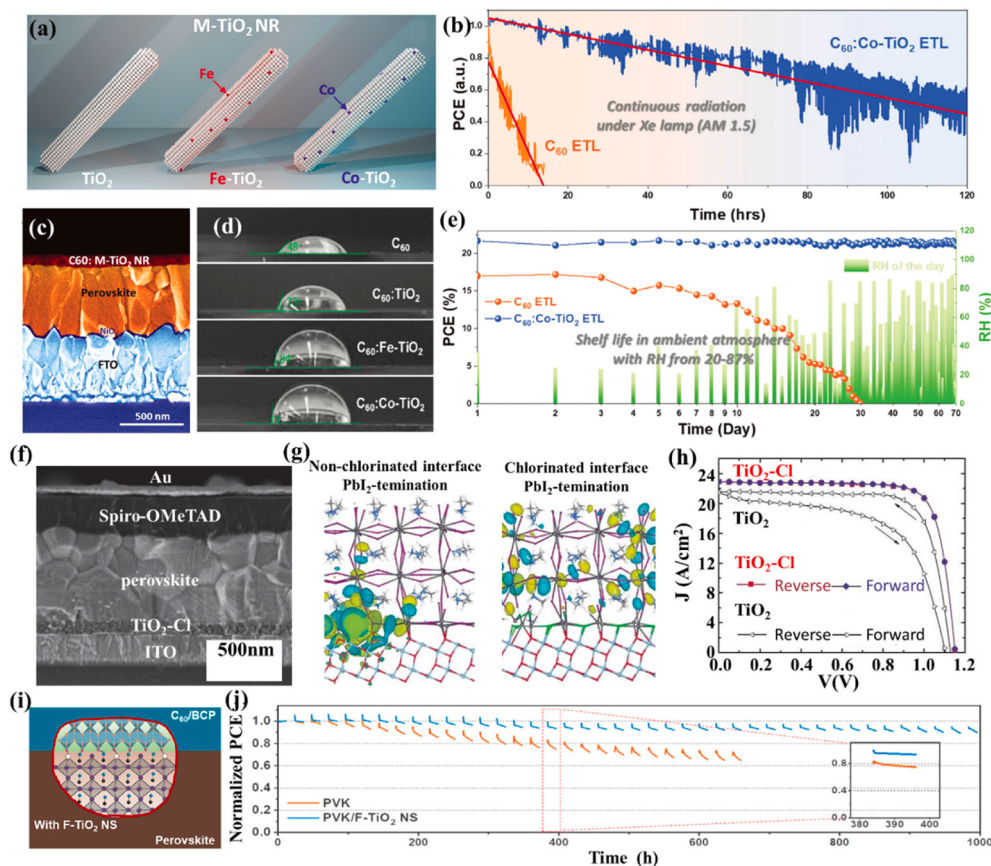


Fig. 15. (a) Schematic diagram of doped TiO_2 NR. (b) Stability test under continuous illumination. (c) Cross-sectional SEM image of PSC. (d) Contact angle images. (e) Device shelf life.^[106] Copyright 2020, Wiley-VCH. (f) Cross-sectional SEM image of PSC; (g) DFT analysis for the passivation effect of Cl; (h) J-V curves of PSCs with or without Cl passivation.^[88] Copyright 2017, The American Association for the Advancement of Science. (i) Schematic illustration of interaction between F- TiO_2 NSs and perovskite; (j) MPP tracking of PSCs under repeated 24-h day/night cycles.^[107] Copyright 2021, Elsevier.

topography as well as efficient electron extraction and transfer ability. Because of the metal doping, the quasi-Fermi-level of ETMs also changed from -3.83 eV for $\text{C}_{60}:\text{TiO}_2$ to -4.04 eV and -4.09 eV for $\text{C}_{60}:\text{Fe}-\text{TiO}_2$ and $\text{C}_{60}:\text{Co}-\text{TiO}_2$, respectively. The decreased energy level offset favored the transfer of photoelectrons cross the ETM/perovskite interface. Besides, the doped TiO_2 shown an improved electron mobility and increased carrier density at even high temperature. Moreover, the

composite materials displayed different hydrophobicity property, as investigated by contact angle measurement in Fig. 15(d). The contact angle of C_{60} , $\text{C}_{60}:\text{TiO}_2$, $\text{C}_{60}:\text{Fe}-\text{TiO}_2$ and $\text{C}_{60}:\text{Co}-\text{TiO}_2$ were 48° , 73° , 84° and 90° , respectively. The higher contact angle indicated the strong hydrophobicity ability. Indeed, both of the working lifetime under continuously illumination and storage stability were significantly enhanced for $\text{C}_{60}:\text{Co}-\text{TiO}_2$ based PSCs, as shown in Fig. 15(b,e). This

study forebodes the materials modification by element doping is expected to excavate the potential of target materials to achieve high efficiency as well as open up more opportunities in extending device stability to new time scale. In addition, focused on the interface defects between perovskite and TiO_2 , chlorine doped TiO_2 ETM was used to fabricate the PSCs.[88] The cross-sectional image of PSCs was illustrated in Fig. 15(f). Particularly, Cl- TiO_2 nanocrystals were prepared and dispersed in a mixed solution of methanol and chloroform to maintain Cl ligands on the surface. The effect of defects passivation was firstly examined by density functional theory (DFT) as shown in Fig. 15(g). The Pb-X ($X = \text{I}$ or Cl) anti-bonding state acting as non-radiative recombination center was difficult to form after Cl doping. Transient photovoltage measurements indicated slower charge recombination at the interface between Cl- TiO_2 and perovskite, in accordance with DFT results. The transient photocurrent test illustrated a similar charge transfer process, indicating that the performance improvement was primarily due to decreased charge recombination. The device based on Cl- TiO_2 has mitigate carrier recombination and improved interfacial contact, achieving 20 % efficiency and negligible hysteresis, as shown in Fig. 15(h). Recently, Alex K.-Y. Jen et. al. used hydrofluoric acid to modify the TiO_2 surface.[107] The robust fluoroterminated TiO_2 nanosheets (F- TiO_2 NSs) effectively passivated the perovskite surface defects by interact with uncoordinated lead and MA/FA ions, as shown in Fig. 15(i). As a result, the F- TiO_2 NSs-based PSCs exhibited superior operational stability compared with control devices, which can maintain over 90 % of their initial PCEs after 1000 h of day/night MPP tracking, as illustrated in Fig. 15(j).

Furthermore, the yttrium was used to improve the optoelectronic properties of SrSnO_3 by n-type doping.[108] The SrSnO_3 (SSO) is ABO_3 perovskite structure. Further TEM and HRTEM analysis show that the yttrium-doped SrSnO_3 (YSSO) NPs were also pure orthorhombic phase with the size of 2.9 ± 1.8 nm, as illustrated in Fig. 16(a). The Y cations were successfully incorporated in SSO as verified by EDS mapping. Then the YSSO NPs were dispersed to form stable and highly transparent

colloidal solution, as shown in Fig. 16(b). The optical absorption peak centered at 257 nm and PL emission peak is located at 435 nm with a large Stokes shift. The well-dispersed YSSO solution was spin-coated on substrate as ETMs in PSCs, which eventually achieved a PCE of 19.0 % with negligible hysteresis and well stability. The boost photovoltaic performance is mainly due to the following factors, i. The doping successfully narrowed the band gap and downshift the conduction band position, which enhanced the light absorption and modified the interface energy alignment. ii. The YSSO has a higher electron concentration and conductivity. The dependence of open-circuit voltage (V_{oc}) on incident light intensity (P) in Fig. 16(c) confirmed the less recombination due to the small slope value of YSSO. Not only the experiment results but also theoretical calculation verified the improved optoelectronic properties by Y doping. Moreover, metal atoms doping is also widely used to modify the ZnO ETM properties. Jang et al. synthetically inquire into the alkali-metal doped ZnO ETMs.[109] Specifically, the energy levels were analyzed by UPS and the corresponding schematic illustrations were shown in Fig. 16(d). The K-doped ZnO illustrated a largest E_F increase of ~ 0.21 eV. Additionally, the PL spectra successfully confirmed the decreased defects density, due to the reduced defect-related PL emission at about 550 nm, as shown in Fig. 16(e). The doping effectively improved the electron mobility from $0.65 \times 10^{-3} \text{ cm}^2/\text{V}\cdot\text{s}$ for pristine ZnO to $1.45 \times 10^{-3} \text{ cm}^2/\text{V}\cdot\text{s}$ for ZnO-K . Also, the capacitance–voltage (Cp-V) analysis and Mott-Schottky plots as illustrated in Fig. 16(f) indicated the ZnO-K ETM shown a high built-in potential than pristine ZnO , which put down to the up-shift E_F . On the basis, the PSCs achieved higher efficiency of 17.80 %, 18.90 %, 19.90 % for ZnO-Li , ZnO-Na , ZnO-K based PSCs respectively, which all were superior to pristine ZnO based device and in turn validated the modification effect of metal doping. Analogously, in view of the surface hydroxyl groups induced defects, Sargent et al. used NH_4F to modify the surface of SnO_2 .[110] NH_4^+ with weak acidity could react with terminal-hydroxyls (OH_T) and release NH_3 and water vapor. Meanwhile, fluorine successfully doped the SnO_2 surface as shown in Fig. 16(g). The DFT

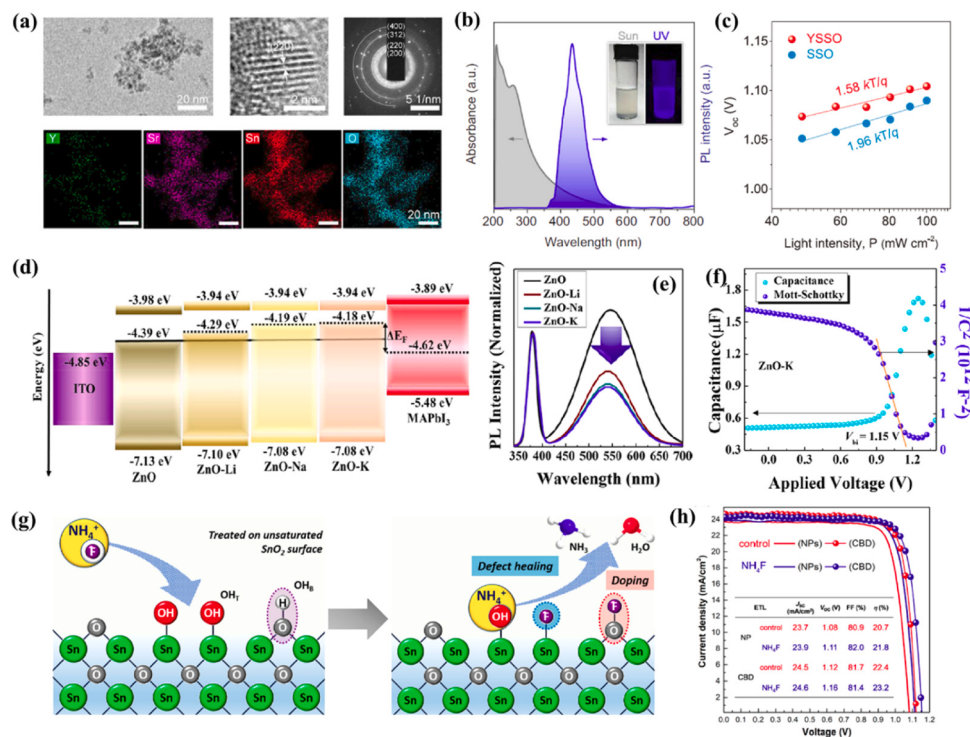


Fig. 16. (a) (HR)TEM and elemental mapping images. (b) Optical absorption and PL spectra. (c) $V_{\text{oc}}\text{-}P$ curves.[108] Copyright 2019, Elsevier. (d) Schematic illustrations of energy levels for doped ZnO ETMs. (e) PL spectra of doped ZnO . (f) $C_p\text{-}V$ and Mott-Schottky curves of ZnO-K based PSC.[109] Copyright 2018, American Chemical Society. (g) Schematic illustration of NH_4F modified SnO_2 . (h) J-V curves.[110] Copyright 2020, American Chemical Society.

calculation indicated that the F atom reacted with OH_T to form F_T by anion exchange. Also, the bridge oxygen may be substituted by F to realize n-type doping. Therefore, the NH₄F treatment effectively realized the defect passivation and energy level modification, which dramatically decreased the interface energy loss and eventually contributed to a high efficiency of 23.2 %, as shown in Fig. 16(h). Moreover, the NH₄Cl induced coagulated SnO₂ also demonstrated the optimized electronic property and decreased defects.[111] Recently, Tan et al. selected K⁺ and Cl⁻ to optimize the SnO₂ ETM, which simultaneously modified ETM/perovskite interface contact and enlarged the grain size of perovskite superstratum.[112].

So far, there are several elements such as Cl, Al, Y, Ru have been proven to be effective dopants tuning the optoelectronic performance of ETMs. By elemental doping, the interface recombination is decreased and FF is effectively increased, thereby leading to a high efficiency as shown in Table 3. Notably, the low-temperature ETMs doped with Fe, Co, KCl, NH₄F, NH₄Cl achieved a high PCE values over 21 %. Indeed, chemical doping could effectively tune the CBM and modify the work function to match the perovskite. However, the doping processing parameters especially the stoichiometric amount should be carefully regulated to optimize the performance.

4.2. Surface modification

Surface modification can significantly influence the surface energy levels of low-temperature ETMs and ideally, this should facilitate efficient charge extraction. Several strategies have been reported in the literature to mitigate the presence of surface defects in the low-temperature ETMs, which can either take place during materials synthesis or as a post-treatment. Moreover, the surface of low-temperature ETMs often has an important role in determining the nucleation and growth process of upper perovskite layer, which is beneficial to improve device performance and long-term stability.[133] The series of issues about surface defects, energy level aligning, interfacial contract still remain the major obstacle to progress. Surface modification therefore is regarded as one of the most popular strategies currently to push the device performance development.

In particular, the carbon materials with strong designability, adjustable electronic structure, such as carbon nanotubes, graphene, graphene oxide, carbon quantum-dots, fullerenes and their derivatives, have already been used to modify the surface of ETMs. For example, the carboxylic acid- and hydroxyl-rich red-carbon quantum dots (RCQs) was synthesized to optimize the surface property of low-temperature SnO₂ ETM.[134] On the basis, the modified SnO₂ exhibited a dramatically increased electron mobility to $1.73 \times 10^{-2} \text{ cm}^2 \text{V}^{-1} \text{s}^{-1}$. At the same time, the surface hydrophilia was improved, which facilitate the heterogeneous nucleation of perovskite and thereby improved the crystal quality, as verified before.[135] The PSCs based on the novel ETM successfully acquired a high efficiency of 22.77 % and improved the environmental endurance, simultaneously. Nevertheless, the chemical interaction between ETM and carbon materials is always neglect. In 2019, Janssen et al. employed XPS depth profile measurement to monitor the distribution and investigate the chemical bonds of PCBM, C₆₀, PCBA materials on SnO₂ ETM.[136] Compared with PCBM and C₆₀, the PCBA could react with surface hydroxyl groups and is more likely to bond with SnO₂. While, for PCBM, only the monolayer at SnO₂/perovskite interface is important for electron transfer and thermal post-treatment is indispensable to bonding. As for C₆₀, it can't bond with SnO₂ ETM and thereby exhibited inferior passivation effect. Recently, Chen et al. analyzed the modification effect of C₆₀ pyrrolidine tris-acid (CPTA) and 6,6-phenyl C₆₁-butyric acid methyl ester (PC₆₁BM) on SnO₂ ETM.[137] The COOH-group of CPTA could anchor at the SnO₂ surface by chemical interaction. While, the PC₆₁BM only covered SnO₂ surface by physisorption. Such surface cases were simplified by two functional groups (Sn-COO-H and [Sn-OH, COOCH₃-H]). The charge plots of above models are illustrated in Fig. 17(a). Obviously, the charge density of SnO₂

increased gradually from inside to outside, due to the formation of Sn-O bond. The interfacial dipole moments effectively screened the holes in perovskite and in turns prevented the back recombination. In contrast, there was no obvious charge redistribution for the PC₆₁BM modified SnO₂. Therefore, the PSCs based on CPTA-modified ETM exhibited a higher PCE. To gain insight into the interface carrier dynamics, the ultrafast pump-probe technique was proposed and carrier transfer behaviors were illustrated in Fig. 17(b). Compared with the pristine SnO₂, the use of fullerene-derivatives reduced the electron injection times (τ_{inj}), because of the passivation of surface defects and regulation of band alignment. While, due to the surface dipoles induced by chemisorption, the back-recombination time ($\tau_{1h, \text{rec}}$) of CPTA/SnO₂ is larger PC₆₁BM-SnO₂ and pristine ETM. Meanwhile, the non-radiative recombination times of electrons and holes ($\tau_{e, r}$ and $\tau_{2h, \text{rec}}$) within perovskite were also prolonged, followed the same trend with $\tau_{1h, \text{rec}}$. Recently, the new carbon allotrope, graphdiyne, with sp and sp₂ hybridization, high π -conjugated and rigid structure was employed to maximize the matching between ETM and perovskite.[19] To dissect the influence of graphdiyne on SnO₂, a series of measurements and theoretical calculation were conducted. As shown in Fig. 17(c,d), the conduction band of modified SnO₂ was elevated and the C-O σ bond was formed, both of which promoted the efficient charge extraction and transfer. Furthermore, the use of graphdiyne also provided a nice platform to guide the perovskite growth. From the dark J-V curves illustrated in Fig. 17(e), the decreased trap density of perovskite deposited on graphdiyne-SnO₂ was calculated ($\sim 4.46 \times 10^{15} \text{ cm}^{-3}$), which verified the positive function of graphdiyne for perovskite quality. So far, both experimental results and theoretical calculations tamp the coordinate regulation role on both lower ETM and upper perovskite layer.

Moreover, aiming at the high series resistance of TiO₂, graphene was used to modify the conductivity of ETM and tune energy barrier at ETM/perovskite interface, which eventually contributed the improved performance, as shown in Fig. 17(h). The EIS spectra clearly reveal that series resistance of graphene/TiO₂ is significantly decreased. In addition, an increase in recombination resistance indicates a decrease in charge recombination, explaining the enhancement of J_{SC} .[138] In regard to the current-voltage hysteresis issue, the C₆₀ interfacial layer was introduced to rearranging the ion gradient, as shown in Fig. 17(f,g). Without C₆₀, the photo-generated electrons were blocked by ions induced electric field at interface, and the holes were inclined to move forward opposite direction of extraction.[139] While, the ions at TiO₂/C₆₀/perovskite interface could redistribute under illumination, thereby changing the internal electric fields. Thus, the C₆₀ modification layer favors the carrier extraction and in turn, improving the device performance with negative hysteresis.

Except for carbon materials, polymers are also widely applied to optimize the ETM/perovskite interface states. For instance, a zwitterion was used to modify SnO₂ surface and obtained a high PCE of about 20 % by forming interface dipole layer, as shown in Fig. 18(a,e).[140] The zwitterion material, 3-(1-pyridinio)-1-propanesulfonate, increased the energy band position of SnO₂, thereby raising the built-in potential and V_{OC} , as illustrated in Fig. 18(b,c). Moreover, the interface dipole enhanced the electron transport capability and prevented the reverse transfer of electrons, which effectively suppressed charge recombination at interface. Besides, positively charged atoms in the interface layer successfully passivated Pb-I defects, thereby improving the stability of the device, as verified by DFT calculation in Fig. 18(d). Thereafter, an amino-functionalized polymer (PN4N) was employed to modify the SnO₂ and CsPbI₂Br perovskite interface and achieved a 16 % efficiency for all-inorganic PSCs.[141] The availability of highly efficient and stable devices benefits from the following contributions: i) The dipole formed by the PN4N at the interface reduces the work function of SnO₂, and the improved energy level matching results in a significant increase in the V_{OC} . ii) PN4N can improve the wettability of SnO₂, realizing the controllable fabrication of perovskite with large grains. iii) The strong interaction between PN4N and perovskite favors the charge transfer at

Table 3

Non-exhaustive summary of elemental doping for low-temperature ETMs.

ETMs	Dopant	CBM ^{a)} [eV]	CBM of perovskite	R _{rec} ^{b)}	PCE ^{c)} [%]	Voc [V]	J _{sc} [mA cm ⁻²]	FF [%]	Ref.
TiO ₂	Control	-3.83	-4.0		20.89	1.08	23.85	81.1	[106]
	Fe doped	-4.04			21.63	1.10	24.25	81.1	
	Co doped	-4.09		↓	22.13	1.10	24.38	82.5	
TiO ₂	Control	-4.0	-3.75		13.8	1.06	19.90	65.44	[87]
	doped	-4.0		↓	16.5	1.07	22.80	67.47	
TiO ₂	Control	-4.1	-4.2		18.5	1.129	21.6	76.0	[88]
	doped	-4.4	-4.4	↓	20.9	1.151	23.0	78.9	
ZnO	Control	-3.98	-3.89		16.10	1.07	21.10	71.5	[109]
	Li doped	-3.94		↓	17.80	1.10	22.00	73.3	
	Na doped	-3.94		↓	18.90	1.11	22.50	75.4	
	K doped	-3.94		↓	19.90	1.13	23.00	77.1	
SnO ₂	Control	n/a	-3.9		15.7	1.01	22.3	69.6	[113]
	Sb doped	n/a		n/a	17.7	1.06	22.5	74.2	
SnO ₂	Control	-4.05	-4.06		20.2	1.077	24.0	77.9	[112]
	doped	-4.19		↓	22.2	1.137	24.2	80.7	
SnO ₂	Control	-4.22	-3.95		15.29	1.084	21.98	64.17	[114]
	doped	-4.35		↓	18.20	1.106	23.27	70.71	
SnO ₂	Control	n/a	n/a		22.4	1.12	24.5	81.7	[110]
	NH ₄ F doped	n/a		↓	23.2	1.16	24.6	81.4	
SnO ₂	Control	-3.91			18.71	1.10	23.22	73.47	[111]
	doped	-4.34		↓	21.38	1.15	24.28	76.83	
SnO ₂	Control	-4.04	-3.95		15.80	0.99 ± 0.04	21.72 ± 0.52	73.62 ± 1.50	[115]
	doped	-3.96		↓	18.2	1.06	22.78	75.41	
SnO ₂	Control	-4.15	-3.9		17.35	1.089	23.06	69.1	[116]
	doped	-4.02		↓	19.19	1.105	24.39	71.2	
SnO ₂	Control	-4.28	3.8		17.30	1.06	24.8	66	[117]
	doped	-3.93		↓	19.54	1.08	25.3	72	
SnO ₂	Control	-4.06	-3.88		18.95	1.11	22.72	75.1	[118]
	Zn doped	-3.85		↓	20.16	1.12	23.41	77.3	
SnO ₂	Control	n/a	n/a		19.69	1.144	21.43	75.20	[119]
	doped	n/a		n/a	20.47	1.157	22.77	74.70	
SnO ₂	Control	-4.45	-4.15		18.08	1.074	22.44	75.04	[120]
	doped	-4.26		↓	20.71	1.130	23.56	77.78	
SnO ₂	Control	-4.30	-3.90		20.2	1.10	24.10	76	[121]
	doped	-4.03		↓	22.0	1.15	24.60	78	
SnO ₂	Control	-4.41	-3.95		16.25	1.03	21.74	72.28	[122]
	doped	-4.15		↓	20.2	1.13	22.92	78.05	
SnO ₂	Control	-4.15	-4.01		15.07	1.0	22.7	66.1	[123]
	doped	-4.04		↓	18.1	1.1	23.6	69.2	
SnO ₂	Control	n/a	-3.95		8.09	0.77	20.33	52	[124]
	doped	↓		↓	10.01	0.76	22.18	59	
SnO ₂	Control	-4.23	-3.93		17.73	1.110	21.53	74.19	[25]
	Mg doped	-4.89		↓	19.21	1.112	22.80	75.78	
SnO ₂	Control	-4.08	-3.79		17.21	1.07	21.64	73.96	[125]
	Al doped	-3.91		↓	18.45	1.09	21.82	77.61	
	La doped	-3.92		↓	18.36	1.08	21.61	78.17	
SnO ₂	Alla doped	-3.93		↓	19.13	1.11	21.92	78.08	[126]
	Control	-4.43	-4.20		18.23	1.124	23.29	70	
SnO ₂	Sb doped	-4.54		↓	20.73	1.173	23.90	74	[127]
	Control	n/a	-3.9		8.47	0.948	14.99	59.59	
SnO ₂	Mo doped	n/a		↓	10.52	0.972	15.20	71.10	[128]
	Control	-4.25	-3.93		16.11	1.032	23.51	66.4	
SnO ₂	Ga doped	-4.17		↓	18.18	1.068	23.90	71.4	[129]
	Control	n/a	n/a		19.48	1.158	21.65	77.7	
SnO ₂	Ta doped	n/a		↓	20.80	1.161	22.79	78.6	[130]
	Control	-4.09	-3.9		14.21	1.06	20.67	65	
SnO ₂	La doped	-4.02		↓	17.08	1.09	21.77	72	[131]
	Control	-4.40	-3.93		19.12	1.098	22.77	76.5	
SrSnO ₃	Nd doped	-4.14		↓	20.92	1.122	23.85	78.2	[108]
	Control	-3.92	-4.15		16.9	1.13	22.3	67	
BaSnO ₃	Y doped	-4.17		↓	19.0	1.14	22.7	74	[132]
	Control	n/a	n/a		19.4	1.07	23	77.9	
ZnO	Sr doped	n/a		↓	21.0	1.13	23	81.0	[109]
	Control	-3.98	-3.89		16.10	1.07	21.10	71.5	
Li	doped	-3.94		↓	17.80	1.10	22.00	73.3	[109]
	doped	-3.94		↓	18.90	1.11	22.50	75.4	
Na	doped	-3.94		↓	19.90	1.13	23.00	77.1	[109]
	K doped	-3.94		↓	19.90	1.13	23.00	77.1	

^{a)} Conduction band minimum; ^{b)} recombination rate; ^{c)} device efficiency acquired at reverse-scan bias; direction..

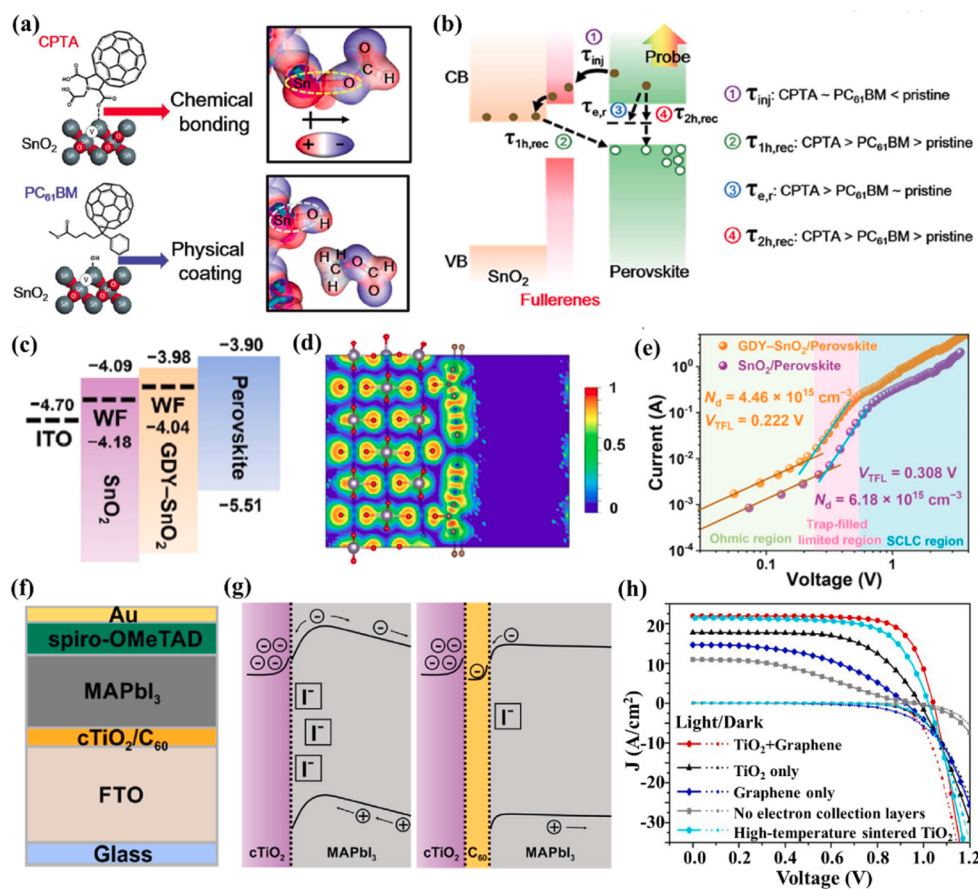


Fig. 17. (a) Schematic illustrations of the interaction between SnO₂ ETM and CPTA/ PC₆₁BM (left) and charge plot images (right). (b) Schematic diagram (left) and corresponding photocarrier dynamics (right). [137] Copyright 2020, Royal Society of Chemistry. (c) Energy band alignment for ITO/ETM/perovskite. (d) The calculated electron localization function of graphdiyne-SnO₂ ETM. (e) Dark J-V response of electron-only devices based on different ETMs. [19] Copyright 2020, Wiley-VCH. Schematic diagram of (f) PSCs architecture and (g) energy level. [139] Copyright 2020, American Chemical Society. (h) J-V curves of devices based on various ETLs. [138] Copyright 2014, American Chemical Society.

the interface and also inhibits photo-induced halide segregation. More than above mentioned materials, ethylene diamine tetraacetic acid (EDTA) has been used repeatedly to modify the surface of ETMs. For example, the EDTA-SnO₂ complex was synthesized to construct planar-structured PSCs, which achieved over 21 % certification PCE and over 18 % PCE on flexible devices. The successful combination of SnO₂ and EDTA was proved by XPS results shown in Fig. 18(f). The introduction of EDTA significantly improved the conductivity of SnO₂, which facilitated the electron extraction from perovskite to ETM and prevented the electrons accumulation at the interface. Also, the EDTA-SnO₂ demonstrated a wetted interface, which was conducive to the formation of highly crystalline perovskite with large grain size, as analyzed in Fig. 18(g). All of these resulted in higher efficiency as well as negligible hysteresis. Not only the device efficiency, but also the long-term stability has been optimized by interface modification.

Furthermore, a variety of inorganic materials have been incorporated at the interface between the ETM and perovskite to effectively modify the intricate surface of ETMs. [143,144] Specifically, with regards to ZnO, its Lewis basic nature and presence of surface defects can lead to deprotonation of perovskite, resulting in significant performance degradation of PSCs. Zhang et al. focused on the service behavior of ZnO based PSCs and innovatively designed the device structure by inserting an ultra-thin Al₂O₃ layer. [20] The Al₂O₃ layer with a thickness of less than 10 Å has little effect on electrons injection, according to the quantum tunneling calculation. While, the ultra-thin insulating layer significantly blocked the interfacial recombination between electrons in ZnO and holes in perovskite. The PL spectra in Fig. 18(h) indicated that

the metal layer with thickness of 4 Å exhibited an optimum charge blocking effect. More than that, the metal layer protected the perovskite from degradation by isolating the ETM and perovskite. The XRD results illustrated the elevated resistance to decomposition of perovskite deposited on the thicker Al₂O₃ layer, as shown in Fig. 18(i). Taken together, the inserting of Al₂O₃ modification layer simultaneously realized the improvement of efficiency and stability for ZnO-based PSCs. Moreover, Zheng et al. proposed a novel strategy to convert ZnO surface into ZnS at the ZnO/perovskite interface by sulfidation. [145] The device structure diagram and the cross-sectional SEM image of the typical PSC based on ZnO-ZnS-450 ETM are illustrated in Fig. 19(a, b). The XRD patterns indicated the formation of ZnS with wurtzite structure and the elemental maps confirmed the uniform distribution of S on the ZnO-ZnS surface, as shown in Fig. 19(b, d). The S atoms on the ZnO-ZnS surface exhibited strong binding affinity towards Pb²⁺ ions, thereby creating a novel pathway for electron transport that accelerated electron transfer and reduced interfacial charge recombination. Meanwhile, the ZnS interlayer functioned as a cascade ETM, effectively suppressing charge recombination between the ZnO and perovskite layers. On the basis, the ZnO-ZnS-450 device exhibited improved performance, with an increase in J_{sc} from 22.22 mA cm⁻² to 24.10 mA cm⁻², V_{oc} from 1.072 V to 1.121 V, FF from 71.93 % to 76.66 %, and ultimately PCE from 17.14 % to 20.71 %, as shown in Fig. 19(e). The efficiency statistics of 25 individual devices depicted in Fig. 19(f) demonstrated a significant enhancement in the performance of PSCs following the sulfidation process of ZnO. Moreover, ZnS effectively inhibited the deprotonation of protonated organic amine in the perovskite layer, thereby enhancing overall

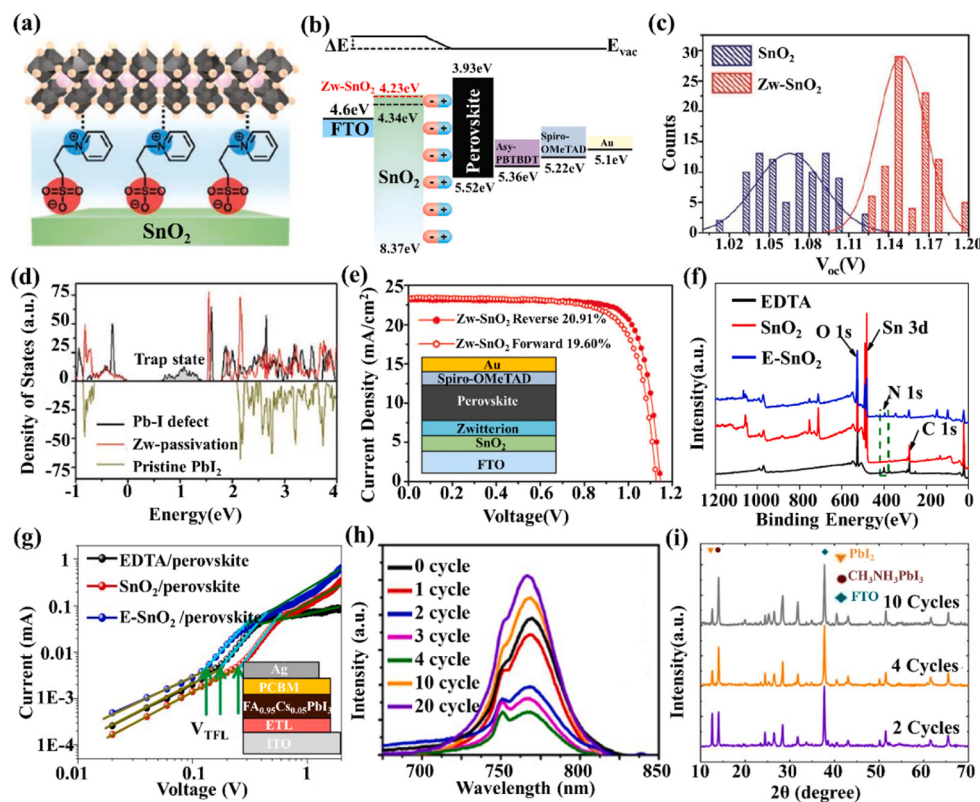


Fig. 18. (a) Schematic diagram of introducing zwitterions at SnO_2 /perovskite interface; (b) Device band structure before and after modification; (c) Histogram of V_{oc} with and without interface layer ; (d) Density of states to analyze defect passivation effect; (e) J-V curves of PSCs based on modified SnO_2 .^[140] Copyright 2018, American Chemical Society. (f) XPS test proves the combination of EDTA and SnO_2 ; (g) Dark state J-V curve of the device whose structure is shown by inset.^[142] Copyright 2018, Springer Nature. (h) PL spectra of ETM/perovskite structure with different Al_2O_3 cycles; (i) XRD of the perovskite aging at 65 °C for 170 min.^[20] Copyright 2016, Elsevier.

stability under both storage and UV radiation conditions. Subsequently, Daoud et al. utilized a thioacetamide solution to transform the surface of ZnO NAs into ZnS, as depicted in Fig. 19(g) for the detailed fabrication process. The flexible PSCs based on core-shell $\text{ZnO}@\text{ZnS}$ NRs demonstrated an impressive efficiency of 12.94 %, representing an increase of more than 8 %.^[146] Additionally, Lu et al. introduced Pb(II)-ion-based salts into ZnO ETMs, which not only promoted the growth of all-inorganic perovskite with improved morphology and orientational order, but also formed a favorable energy level alignment with the perovskite, thus facilitating charge extraction and suppressing charge recombination. The PCE of the $\text{PbX}_2:\text{ZnO}$ -based PSC was boosted from 17.64 % to 20.04 % with an improved fill factor of 84.14 % and a V_{oc} of 1.28 V, being the highest V_{oc} among highly efficient (>20 %) all-inorganic PSCs at that time.^[147]

The simultaneous use of organic and inorganic components to passivate the surface of the electron transport layer can effectively combine their advantages, resulting in a better surface passivation effect.^[148] Considering the weak chemical compatibility between ZnO and perovskite, some researchers utilized ethanolamine (EA) as a passivation agent for the sensitive ZnO surface.^[149] However, although the presence of EA molecules on the surface of ZnO enhanced electron extraction and transport, it did not result in a charged surface. To address this issue, Zheng et al. proposed an innovative approach that utilized both inorganic MgO and organic EA to effectively passivate the ZnO surface.^[150] The introduction of Mg onto ZnO surface could change the binding structure of EA from neutral chelation into charged monodentate form, resulting in improved electrostatic interaction with perovskites. In addition, MgO effectively mitigated charge recombination at the ZnO/perovskite interface. Fig. 20(a) demonstrated the PSC device modified with ZnO-MgO-EA⁺. The energy-dispersive X-ray

spectroscopy mapping in Fig. 20(b) verified the coexistence of Zn and Mg elements. The XRD patterns illustrated in Fig. 20(d) also confirmed the formation of ZnO together with MgO. Temperature-programmed decomposition/mass spectrometry analysis checked on the organic species belongs to EA, as shown in Fig. 20(e). The IR spectra in Fig. 20(g, h) of ZnO-MgO-EA⁺ sample shown that the –OH absorption peaks at 3687 and 1382 cm⁻¹ were disappeared. The new peak at 1509 cm⁻¹ indicated the transform of –NH₂ to –NH₃⁺. All of the results confirmed the successful modification of ZnO by MgO and protonated EA. As shown in Fig. 20(e, f), the PSCs based on ZnO-MgO-EA⁺ achieved a higher efficiency of 18.3 % compared to the ZnO-based device with an efficiency of 15.1 %. Notably, the modified devices exhibited no hysteresis. Moreover, the synergistic modification of ZnO surface significantly enhanced the device stability. As shown in Fig. 20(i), the ZnO-based cell rapidly decomposed within 1 h under illumination, whereas the modified devices demonstrated an impressive retention of over 60 % of their original efficiency after 4 h. In 2022, Yang et al. modified ZnO surfaces by introducing colloidal PbS QDs and tetrabutylammonium iodide (TBAI). The resulting PbS-TBAI films served as a surface wetting control layer and electric dipole layer to regulate the crystal growth of perovskite films and charge behavior in PSC. As a result, the PCE of the optimized ZnO/PbS-TBAI-based PSCs reached 20.53 %, which was the highest among all ZnO PSCs with MAPbI₃ as an absorption layer at that time.^[151]

4.3. Nanostructure management

The structuring low-temperature ETMs is also conducive to boosting the performance of PSCs. Generally, the surface topography is closely related to nucleation and growth of perovskite as well as the charge

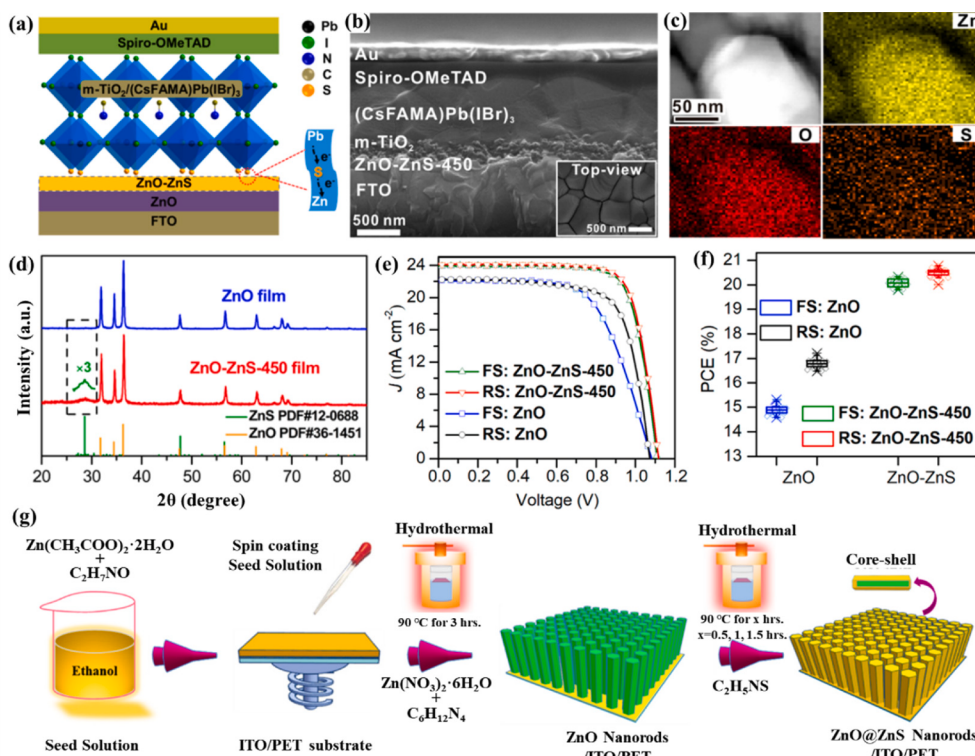


Fig. 19. (a) Schematic diagram of ZnO-ZnS-based PSC device; (b) Cross-sectional SEM image of PSC device; (c) HAADF-STEM image and elemental maps of ZnO-ZnS-450 nanoparticles; (d) XRD patterns of ZnO and ZnO-ZnS-450 samples; (e) Best J-V curves of ZnO and ZnO-ZnS-450 based PSC; (f) PCE of 25 individual ZnO and ZnO-ZnS-450 devices.[145] Copyright 2019, American Chemical Society. (g) Schematic illustration of the fabrication process for the core-shell ZnO@ZnS NAs.[146] Copyright 2021, Elsevier.

transporting property. At the initial stage, the PSCs continued the design idea of dye-sensitized solar cells and always contained mesoporous ETMs. Shortly thereafter, the planar PSCs also achieved high efficiency. So far, the both planar type and mesoporous type PSCs are dominant. While, for PSCs based on low-temperature ETMs the planar structure always presented a lower efficiency than mesoporous type, due to the difference of electron transporting capacity. Nowadays, diverse nanostructures of low-temperature ETMs have been designed to meet the requirement of efficient electron transporting in PSCs, especially in flexible devices. For instance, inspired by mesoporous structure, Seo et al. prepared a porous structure at low temperature and successfully constructed the record-efficiency flexible PSC.[152] The group detailed compared the slight deposition differences at three type structures, as shown in Fig. 21(a). The mesoporous and porous structures illustrated rough surface and pores, which induced lots of air pockets. Compared to planar structure, such pockets tuned the contact interface to composite solid-liquid-interface, which gave rise to a more hydrophobic surface with higher contact angle and lower surface energy. Based on these mesoporous and porous structures, the deposited perovskite films always have enlarged grain size. While the mesoporous layer often needs high temperature and deposits on rigid substrate, which greatly restricts the application in flexible devices. Therefore, the porous planar structure was selected to construct highly efficient flexible PSCs. Fig. 21(b) shows the HR-TEM morphologies of compact planar layer composed of SnO₂ NP and porous planar layer composed of Zn₂SnO₄ NP. Besides, the densely distributed Sn and sparsely distributed Zn mapping images further verified the compactness of SnO₂ layer and porosity of Zn₂SnO₄ layer. The PSCs based on above designed structures eventually obtained a high efficiency of over 23 %, as shown in Fig. 21(c). More importantly, the flexible PSCs using the porous planar ETM achieved the highest record PCE of 20.75 % with superior reproducibility. The 400 cm² large-area flexible PSC module also realized a high efficiency of over 11 %. The nanostructuring of ETMs offers a novel pathway for promoting the

performance and popularizing commercial application.

Core-shell structure ETMs have also been widespread used as ETMs in PSCs to integrate the strength of both core materials and shell materials. Aiming at the problem of imperfect surface properties of ZnO, Jen et al. ingeniously designed a ZnO core-shell structure by grafting fullerenes onto ZnO NPs.[153] The schematic diagram of such complex structure was shown in Fig. 21(d). The fullerene shell effectively passivated the trap states, lifted the Fermi level, and blocked the ions/water diffusion. The PSCs based on the fullerene-anchored ZnO nanoparticle exhibited a higher PCE of over 21 %. Most noteworthy is the improved tolerance to environmental stresses. As shown in Fig. 21(e), the PSCs based on the core-shell structure shown a slight attenuation of initial PCE at RT and even high temperature of 65 °C.

Apart from above mentioned granule structure, the 0D ZnO QD, 1D Zn₂SnO₄ NAs, 3D ZnO nano-walls and unusual Fe₂O₃ nano-islands have been synthesized as the ETMs in PSCs.[22,154] Recently, Zhang et al. systematically analyzed the electric-field distribution difference of usual ETM structures and prepared the highly oriented anatase TiO₂ nanoparticle arrays by facile hydrothermal approach.[155] As shown in Fig. 22(a), in the planar PSCs, the contact area at compact layer/perovskite interface is smaller than in other types of PSCs. However, the electric field between compact layer and perovskite layer is uniform and perpendicular to the substrate, so as to the efficient and immediate collection of photo-generated electrons. On the basis, the charge recombination within planar PSCs was effectively restrained and excellent device performance was thereby achieved. While for mesoscopic PSCs, the mesoporous TiO₂ acts as the electron's extraction and transporting roles. Obviously, the contact area of ETM and perovskite is large, thereby making for the fast electron's extraction. Nevertheless, the random or even offset electric-field distribution at perovskite/TiO₂ NPs interface is not conducive to electrons transfer and collection. More than above common structures, the 1D nanostructure is deemed to potential excellent ETMs due to the theoretically outstanding charge

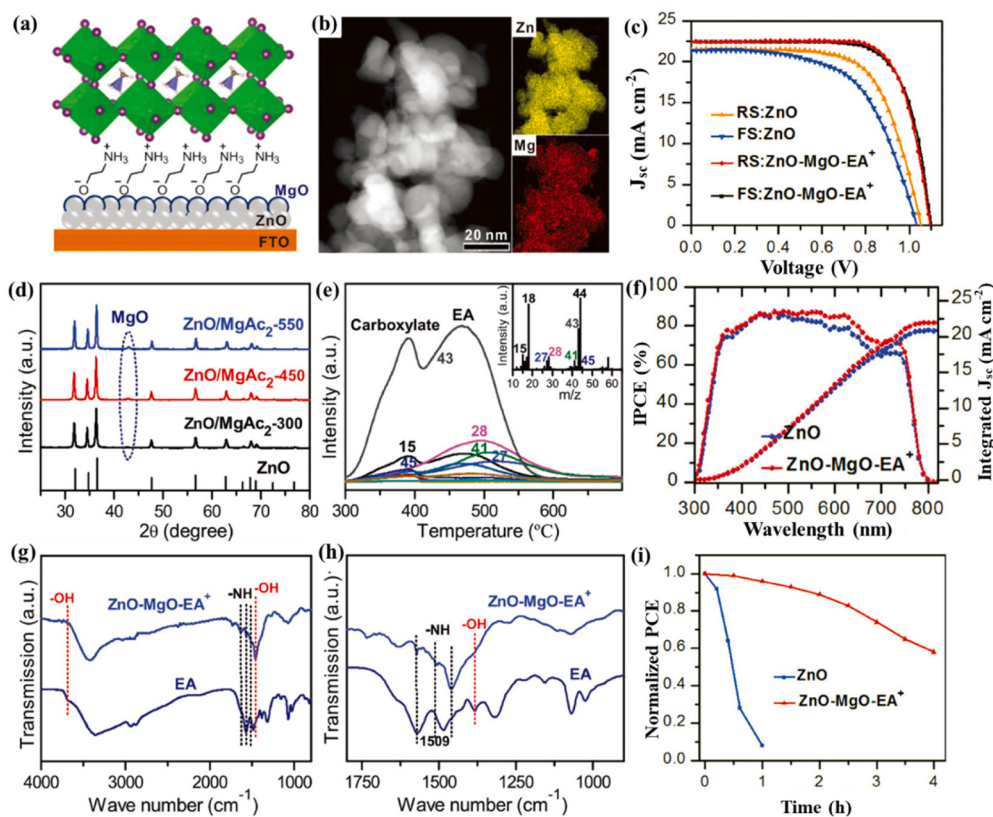


Fig. 20. (a) Schematic illustration of the PSC device modified with ZnO-MgO-EA⁺; (b) HAADF-STEM image and elemental maps of ZnO-MgO-EA⁺ sample; (c) The best J-V data of ZnO and ZnO-MgO-EA⁺ based PSCs; (d) XRD patterns of precursor samples annealed under different temperatures; (e) Temperature-programmed decomposition/mass spectrometry analysis of ZnO-MgO-EA⁺; (f) IPCE and corresponding integrated J_{sc} of the PSCs; (g) IR spectra of the ZnO-MgO-EA⁺ sample and (h) the enlarged spectra; (i) Stability of the different PSCs.[150] Copyright 2018, Wiley-VCH.

transport and light transmission capability. However, although the 1D structure has a larger contact area with perovskite materials than planar structure, the performance is still far behind that of planar devices. Because the overlong charge-transport distance and substandard electric-field distribution like mesoporous structure. Moreover, the sharp tips favor the separation of photo-generated carriers as shown in the schematic diagram of electric field distributions. The nanocone NAs has both sharp tips and long backbone thereby giving rise to the high efficiency. However, the 1D structured ETMs perform worse than mesoscopic and planar structures in most cases, due to the disordered distribution. Hence the patterning technology has been used to modify the growth orientation, so as to tuning the optical properties and electric-field distribution.[156] As shown in Fig. 22(b), the two-dimensional finite difference time domain (FDTD) simulation images show that the ZnO NAs with line pattern and square pattern enhanced the light absorption and illustrated different electric-field distribution because of the reflection and interference of incident light within periodic NAs.[157] Similarly, the highly oriented TiO₂ nanopyramid-like NAs could uniformly distribute on substrate and have the potential to effectively transport charges. By theoretical analysis, the electric field at nanopyramid-like NAs/perovskite interface is a branch which is oriented to the conductive substrate. This field distribution dramatically improves the charge separation efficiency and significantly facilitates the transporting of photo-generated carriers towards opposite direction. At the same time, this structure successfully combines outstanding light transmittance and large contact area, which promote the charge generation and separation as well. To investigate the charge transfer property, the electrostatic fields of nanopyramid was simulated by COMSOL software, as shown in Fig. 22(c,d). The electrostatic potential is getting weaker from the center of nanopyramid to the TiO₂/perovskite interface, which indicated the electrostatic force could actuate the

electrons to the nanopyramid and expel the holes. Meanwhile, the electrostatic field represented by blue solid line is perpendicular to the surface of ETM, which can be resolved into two components, parallel to Z axis and perpendicular to substrate, respectively. This branched electrostatic field is conducive to the transfer of electrons to conductive substrate and holes to HTM, which in turns decrease the charge recombination and contribute to an outstanding performance. No more than above theoretical analysis, a series of photoelectric measurements were proposed to gain insight into the different properties of structured ETMs. The PL spectra in Fig. 22(e) shown that the nanopyramid structure had the lowest PL intensity, indicative of the highest electron extraction ability, compared with other structured-ETMs. The UV-vis transmission spectra and SCLC test also verified the higher optical properties and lower electron trap density of nanopyramid structure than that of nanocone structure, as illustrated in Fig. 22(f,g). The PSCs based on compact TiO₂, mesoporous TiO₂ scaffold, nanocone TiO₂ and nanopyramid TiO₂ ETMs were constructed and achieved the efficiency of 19.73 %, 20.83 %, 21.31 % and 22.48 %, respectively. In all, the structuring of ETMs offers a new way to modify the carrier transfer pathway as well as the optical properties.

4.4. Bilayer engineering

Beyond the aforementioned approaches, bilayer design is also an underlying strategy to optimize the low-temperature ETMs for highly efficient and hysteresis-free PSCs. Obviously, bilayer ETMs remedy the weakness of one ETM by combining the merits of two ETMs. Also, a bilayer electron-transporting layer may enable a graded band alignment, which could boost carrier extraction, open-circuit voltage, as well as the overall surface morphology. More importantly, this design realizes the isolation of interfacial contact and charge transport function. For instance, Zhang

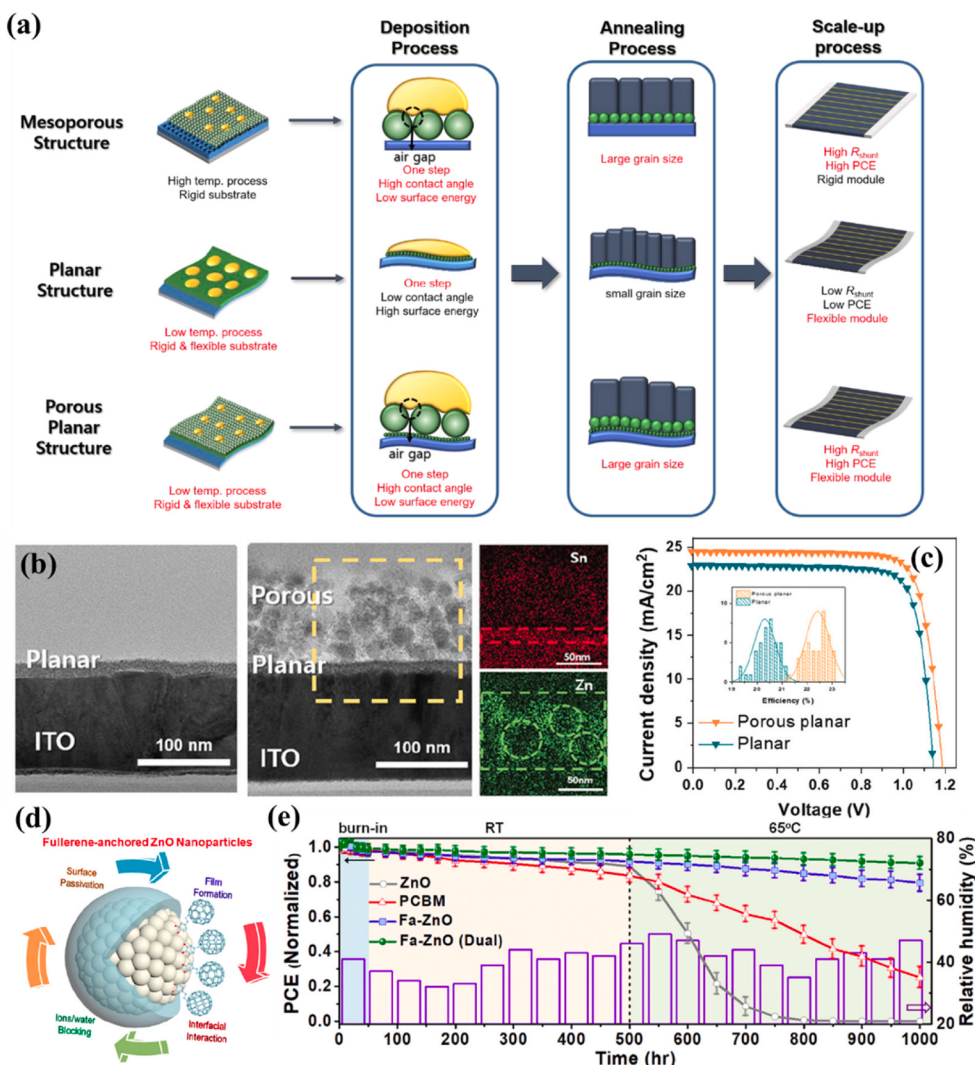


Fig. 21. (a) Illustration of the deposition characteristics at three type structures, (b) HR-TEM images of planar layer and porous planar layer and EDS mapping of Sn (red) and Zn (green), (c) J-V curves of PSCs.^[152] Copyright 2020, Royal Society of Chemistry. (d) Schematic diagram of fullerene-anchored ZnO nanoparticle. (e) the long-term stability of PSCs based on different ETMs.^[153] Copyright 2019, Elsevier.

et al. revealed the defect-induced carrier extraction losses for single layer SnO_2 in PSCs.^[158] As shown in Fig. 23 (b), the single layer ETM prepared by SnO_2 colloids ineluctable formed some pinholes and cracks. The subsequently deposited perovskite materials permeated in and contacted with conductive substrate. They acted as shunt pathways and resulted in seriously charge recombination. To address this issue, bilayer ETMs have been designed to eliminate the shortcoming and in turns enhance the device performance. In 2019, Zhang's group selected the amorphous WO_x (a-WO_x) as the bottom ETM to construct hybrid ETMs at low temperature. The device structure was shown in Fig. 23(a). The a-WO_x/ SnO_2 bilayer ETMs play an important role in blocking holes and transporting electrons. The a-WO_x effectively separated the unfavorable perovskite/ITO contact, which conspicuously suppressed the electron-hole recombination losses. More than that, the hybrid ETMs facilitated the electron extraction by providing two electron transport channels, as shown in Fig. 23(d). The channel 1 of electrons is from perovskite to SnO_2 to a-WO_x. While the channel 2 is from perovskite to a-WO_x. The hybrid ETMs formed a cascade energy level sequence (channel 1), which offer a better transport pathway compared with single layer ETM. All of the photoelectric characterization validated above analysis. As the TRPL spectra shown in Fig. 23(c), the a-WO_x/ SnO_2 ETMs demonstrated shorter lifetime than TiO₂/ SnO_2 due to the outstanding electron transporting property. Consequently, the PSCs based on this bilayer ETMs

demonstrated a higher efficiency of 20.52 %. Recently, Yang et al. initiatively designed a bilayer ETM consist of amorphous WO_x and mesoporous TiO₂ (a-WO_x/m-TiO₂).^[159] The a-WO_x covering on TiO₂ induced a large free energy change to drive the efficient charge transfer. Moreover, the surface wettability was tuned by covering a-WO_x on m-TiO₂, which thereby optimized the perovskite crystal quality. As shown in Fig. 23(e), the PSCs based on a-WO_x/m-TiO₂ ETM demonstrated a high Voc of 1.16 V and PCE of 20.98 %. At the same year, Jung et al. constructed a SnO_2 /ZnO bilayer ETM and optimized the electronic properties by tuning the thermal treatment conditions. The AFM analysis shown the SnO_2 deposited on un-annealing ZnO has low roughness and defect density, which significantly suppressed the interface recombination. Eventually, the PSCs based on above bilayer ETM yielded a higher PCE of 20.43 %.^[160]

Apart from combing different materials to design the bilayer ETMs, the SnO_2 bilayer (Bi-SnO₂) ETM was prepared to conquer the bottleneck of single layer ETM.^[161] Recently, Kang et al. used facile solution route to design an efficient ETM composed of amorphous-crystalline hetero-phase Bi-SnO₂.^[162] The detailed influence of different SnO_2 on ETM-perovskite interface was systematically analyzed. Specifically, AFM was employed to visualize the surface topographies of sol-gel based SnO_2 (SG-SnO₂), nanoparticle based SnO_2 (NP-SnO₂) and Bi-SnO₂ ETMs, and ETM/perovskite interfacial morphology, as shown in Fig. 24 (a-c).

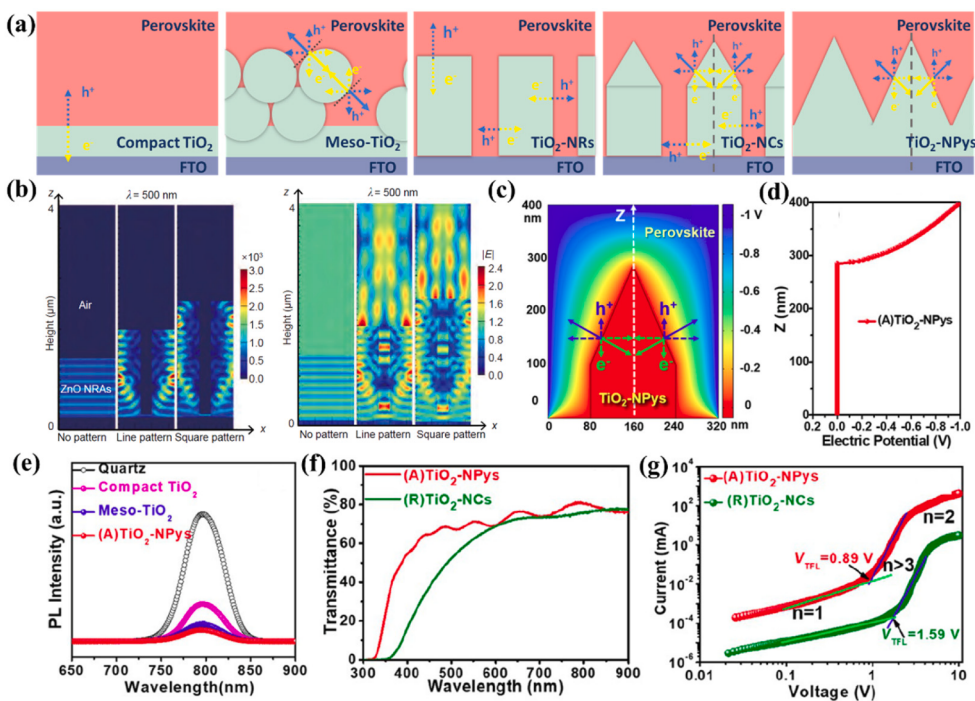


Fig. 22. (a) The schematic diagram of electric field distributions in PSCs based on different ETM structures. (b) FDTD simulations of cross-sectional optical absorption and electric-field intensity $|E|$ distributions of ZnO NAs.^[157] Copyright 2015, American Chemical Society. (c) The COMSOL simulation image of electrostatic potential and (d) calculated potential variation at center line. (e) PL spectra of structured ETM and perovskite. (f) UV/Vis transmittance spectra and (g) SCLC spectra of TiO_2 nanocone and nanopyramid.^[155] Copyright 2020, Wiley-VCH.

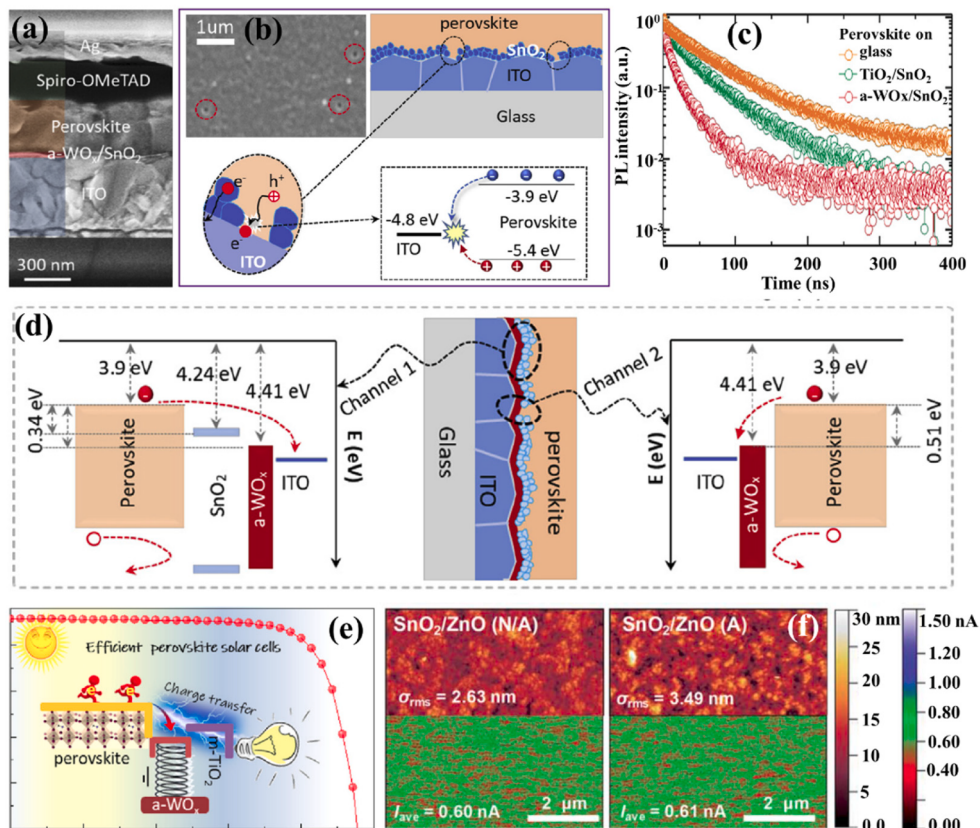


Fig. 23. (a) Cross-sectional SEM image of a-WO_x/SnO₂-based PSCs. (b) SEM of single-layer SnO₂ and the schematic diagram of charge recombination. (c) TRPL of perovskite on different substrates. (d) Schematic diagram of the electron transport channels.^[158] Copyright 2019, Elsevier. (e) The J-V curve of PSCs based on a-WO_x/m-TiO₂ ETM and schematic diagram of hetero-interface.^[159] Copyright 2020, Elsevier. (f) AFM images of different bilayer ETMs.^[160] Copyright 2020, Royal Society of Chemistry.

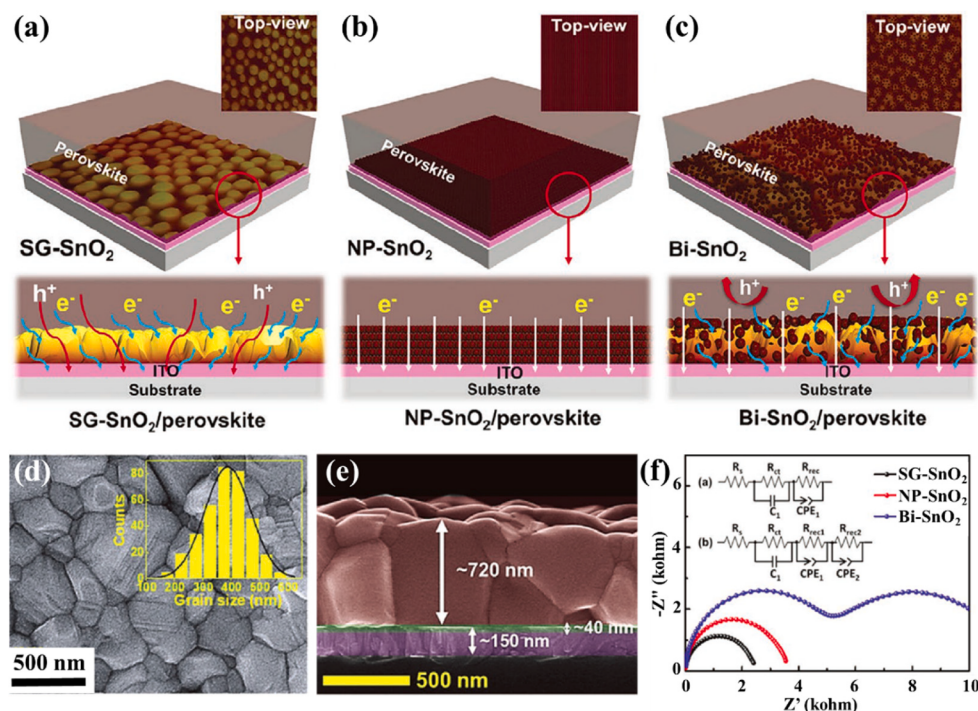


Fig. 24. The 2D- and 3D- schematic illustration of the charge transfers at (a) SG-SnO₂/perovskite interface, (b) NP-SnO₂/perovskite interface and (c) Bi-SnO₂/perovskite interface; (d) top-view and (e) cross-sectional SEM images; (f) EIS curves of PSCs based on different ETMs.^[162] Copyright 2020, Wiley-VCH.

The surface of SG-SnO₂ is full of dome-shaped nanostructures with the size ranging from 0.1 to 1.0 μm. While the surface roughness is 7.55 nm. The high surface-to-volume ratio of nanodomes in SG-SnO₂ are in favor of the charge transfer. However, the coarse-textured surface and high void density lead to the unfavorable recombination. For the NP-SnO₂, the surface is pinhole-free and ultra-smooth with a roughness of only

1.33 nm. Such surface morphology could successfully avert the contact of perovskite and electrode, as well as offer more direct electron transport pathway. But the effectively ETM-perovskite contact area shrink, which is adverse to the charge extraction. Thus, it is inferable that the application of SG-SnO₂ contributes to carrier concentration benefiting by the large ETM-perovskite contact, while the employment of NP-SnO₂

Table 4
Non-exhaustive survey of bilayer configurations for PSCs using low-temperature ETMs.

ETM structure	Sample	CBM ^{a)} [eV]	CBM of perovskite [eV]	HI ^{b)} [%]	R _{rec} ^{c)}	PCE ^{d)} [%]	V _{oc} [V]	J _{sc} [mA cm ⁻²]	FF (%)	Ref.
SnO ₂	Control	-4.41	-3.9			17.67	1.06	21.78	76.58	[158]
a-WO _x /SnO ₂	target	-4.24		↓	↓	20.52	1.11	23.01	80.34	
a-ZTO	Control	-4.38	-3.92			17.10	1.07	21.08	75.8	[163]
a-ZTO/SnO ₂	Target	-4.25		↓	↓	20.04	1.12	22.49	79.6	
SnO ₂	Control	-4.33	-3.60	3.34		18.09	1.03	23.4	75	[164]
SnO ₂ /TiO ₂	Target	-4.10		6.05	↓	20.50	1.10	24.2	77	
Sb: SnO ₂	Control	-4.54	4.20	6		19.15	1.131	23.83	0.71	[126]
Sb: SnO ₂ / SnO ₂	Target	-4.43		2.46	↓	20.73	1.173	23.90	0.74	
SnO ₂	Control	-4.68	-4.36			19.65	1.09	24.39	73.9	[165]
SnO ₂ /2D TiS ₂	Target	-4.63		↓	↓	21.73	1.11	24.57	79.4	
SnO ₂	Control	-4.2	-3.85			21.42	1.13	24.26	78.14	[166]
In ₂ O ₃ / SnO ₂	Target	-4.55		↓	↓	23.24	1.17	24.45	81.09	
ZnO	Control	n/a	-3.8			18.31	1.09	2286	73.52	[150]
ZnO/MgO-EA ⁺	Target	-4.18		↓	↓	21.08	1.12	23.86	78.91	
SnO ₂	Control	-4.2	-3.85			15.2	1.10	21.3	64.9	[167]
SnO ₂ /MgO	Target	-4.55		↓	↓	19.0	1.13	22.1	75.7	
TiO ₂	Control	-4.18	n/a			14	0.99	22	64.5	[168]
SnO ₂	Control	-4.54				19	1.14	22.1	75.4	
SnO ₂ -TiO ₂	Target	n/a		↓	↓	21.1	1.20	22.9	76.4	[169]
TiO ₂	Control	n/a	n/a	14.7		12.02	0.974	22.22	56	
SnO ₂ -TiO ₂	Target	n/a		10.8	↓	18.08	1.01	22.53	79	
ZnO	Control	4.4	3.75			10.23	0.849	21.15	57.3	[170]
ZnO-SnO ₂	Target	↓		↓	↓	12.17	0.909	23.31	57.4	
SnO ₂	Control	-4.5	-3.9			16.43	1.07	21.63	71	[171]
MgO-SnO ₂	Target	n/a				18.23	1.10	22.70	73	
SnO ₂	Control	-4.5	-3.9			11.65	1.10	20.8	65.8	[172]
SnO ₂ -C ₆₀	Target	-3.9		↓	↓	18.8	1.12	21.8	77	

^{a)} Conduction band minimum; ^{b)} Hysteresis index, HI:ΔPCE = |(PCEreverse - PCEforward)|; ^{c)} Recombination rate; ^{d)} device efficiency acquired at reverse-scan bias; direction.

is conducive to carrier mobility due to the direct transport pathway. Notably, Bi-SnO₂ simultaneously demonstrated the special topography of both nanodome morphology of SG-SnO₂ and densely nanoparticle morphology of NP-SnO₂ with a relative smooth surface. Therefore, the Bi-SnO₂ has both advantages of effective charge extraction and hole blocking, simultaneously. Additionally, the EIS test was used to study the charge transfer dynamics, as shown in Fig. 24(f). The Bi-SnO₂ demonstrated the decreased charge transfer resistance and enlarged charge recombination resistance compared with other SnO₂ ETMs, which indicated the enhanced charge extraction and transfer, as well as the suppressed interfacial recombination. In conjunction with this, the morphology of ETM/perovskite was also investigated. The compact, pinhole-free perovskite has an average grain size of 389 nm and a thickness of over 700 nm, as shown in Fig. 24(d, e). Based on such Bi-SnO₂/perovskite film, the PSCs yield a high efficiency of 20.39 %.

Overall, the stacks of different ETMs provide a good surface morphology and enable a graded band alignment, which are beneficial to carrier extraction and contribute to the high performance, as listed in Table 4. Notably, the PSC based on In₂O₃/SnO₂ ETM achieved an outstanding PCE value of over 23 %. However, from the perspective of scalability, the bilayer configuration has less advantage.

4.5. Strain regulation

Apart from above mentioned modification strategies, strain regulation is also introduced into flexible PSCs to boost device performance. On account of the centrosymmetric structure, ZnO as the n-type semiconductor also has piezoelectric properties. The strain-induced piezoelectric polarization charges could effectively regulate the carrier dynamic behavior at ZnO/perovskite interface. For instance, two types of prototype devices were fabricated on flexible substrate according to the direction of c-axis: pointing away from perovskite (ZPSC-I) and pointing towards perovskite (ZPSC-II). [173] The external strain was firstly proposed to investigate the performance change. Specifically, as for ZPSC-I, the V_{oc} and I_{sc} were enhanced accompanied with increased compressive strain. While, above parameters were decreased accompanied with increased tensile strain. The FF demonstrated a strain independent phenomenon. As for ZPSC-II, the V_{oc} and I_{sc} showed a reverse variation trend to ZPSC-I. While, FF of ZPSC-II was improved with increasing compressive strains and has no obvious change under tensile strains. All of above variation confirmed effectiveness of external strain for performance regulation. Recently, the flexible PSCs based on ZnO NAs were constructed. [174] By strain regulation, the device performance achieved ~ 40 % enhancement. Because of the device structure (ITO/ZnO/MAPbI₃/Spiro-OMeTAD/Au), the ZnO NAs underwent tensile strain when the device is bent upward. On the contrary, the ZnO NAs underwent compressive strain when the device is forced downward. Then the static tensile and compressive strain could induce positive and negative potential at ZnO/perovskite interface, respectively, which further tuned the energy-level structure at interface. Specifically, the tensile strain introduced positive piezoelectric potential and thereby pulled down the energy level of ZnO, which further reduced the potential height for electron transfer. Conversely, if the device was bent downward, the ZnO NAs experienced a compressive strain, which produced negative piezoelectric potential to elevate the energy level of ZnO. Obviously, it increased the electron transport barrier and resulted in the bad performance. Therefore, strain regulation pointed out a new direction to realize energy level matching as well as photovoltaic performance modulation, especially in flexible PSCs.

4.6. Discussion and perspective

The quality and optoelectrical property of low-temperature ETMs are critical factors that significantly impact the overall efficiency of PSCs. As such, they require careful consideration during the design and development process. To move forward, it is imperative to focus efforts on

exploring innovative modification strategies that can enhance the electrical properties of low-temperature ETMs, as shown in Fig. 25. By identifying new materials with improved charge transport capabilities or developing effective modification techniques to optimize their energy levels alignment with perovskite absorbers, researchers can bridge the performance gap between low-temperature and high-temperature ETMs. In general, element doping provides a direct approach to enhance the electrical properties of ETM, enabling effective control over its electrical behavior. However, the accuracy of doping and its underlying action mechanism requires further investigation for a comprehensive understanding. Furthermore, nanostructure management not only allows for the modification of the ETM/perovskite contact interface but also enables light management to enhance the performance of PSCs. In addition, for low-temperature ZnO ETMs with piezoelectric effect, the strain-induced piezoelectric polarization charge can effectively modulate the dynamic behavior of charge carriers at the interface between ZnO and perovskite. However, it must be acknowledged that strain regulation has certain limitations and poses challenges in operation for large-area ETMs. The implementation of bilayer engineering effectively compensates for the photoelectric property deficiencies exhibited by a single ETM, thereby not only addressing the inherent limitations of ETMs but also optimizing the interface contact characteristics between ETM and perovskite. The surface modification is currently the most effective and widely utilized technique, playing an indispensable and vital role in suppressing interfacial charge recombination while promoting charge extraction/transport. This approach significantly enhances the chemical compatibility of the interface, thereby empowering low-temperature ETM-based PSCs to achieve their theoretical efficiency limits.

While various regulatory strategies developed in recent years have led to significant improvements in efficiency, majority of the aforementioned optimized designs and modulation strategies rely on treatment schemes that differ considerably from current industrial techniques. This disparity poses a considerable obstacle to rapid and widespread industrial adoption. In this context, future efforts should focus on developing optimization strategies for large-scale ETMs that are compatible with low threshold upgrades for manufacturing low-temperature ETMs. The most direct approach to achieve this is by incorporating dopants into the preparation process of ETMs, leveraging existing production facilities for electrical control implementation. Considering the remarkable efficacy of surface optimization, it is

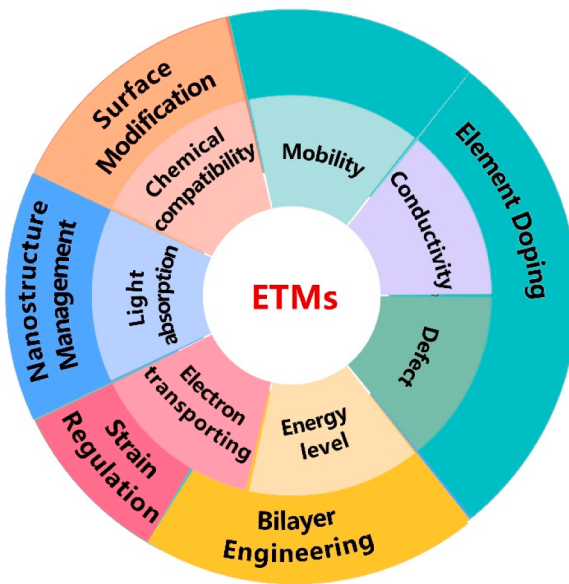


Fig. 25. Schematic diagram of low temperature ETM electrical performance control strategy.

imperative to explore a surface modification material that address both surface regulation and large-scale preparation techniques from the perspective of solvent chemistry. The advantages of high solvent compatibility and facile anchoring of functional groups make organic molecules a promising choice for candidate materials, despite the additional process steps involved.

5. Progress of Low-Temperature ETMs for flexible PSCs

Flexible PSCs are manufactured by replacing traditional rigid glass substrates with flexible substrates such as polyethylene terephthalate (PET) and polyethylene naphthalate (PEN). However, the thermal and chemical fragility of most organic materials makes it challenging for flexible substrates to withstand excessively high temperatures without losing their elastic properties.^[175] This poses multi-scale challenges to ETM, which can potentially hinder device performance. First of all, the quality and electrical property of the ETM often suffer due to constraints imposed by the substrate's temperature tolerance. In Chapter 4, we have delved into this problem extensively and provided a comprehensive review of mainstream regulation strategies. Secondly, organic-inorganic hybrid perovskites often exhibit poor adhesion to adjacent ETMs or substrates due to their low adhesion energy.^[176] Additionally, the thermal expansion/contraction of flexible substrates during annealing treatment can further weaken this interfacial adhesion.^[177] Consequently, the mechanical durability become critical concerns in flexible PSCs. Moreover, this heterogeneous interface with inherent structural brittleness becomes even more fragile when subjected to mechanical deformation.^[10] These challenges significantly impede the stability and flexible application of the device. Especially for low-temperature inorganic ETMs, the disparity in physical properties (e.g. thermal expansivity) among organic perovskite, polymer substrate, and inorganic ETM results in interface residual stresses.^[178] At the molecular level, the accumulated strain results in compromised phase stability of perovskite, while non-releasable lattice stress also contributes to accelerated material degradation. Upon mechanical deformation, discernible faultage emerge at the macroscopic level in the functional layers adjacent to the ETM.

Flexible PSCs have gradually demonstrated the efficiencies needed for technoeconomic competitiveness, based on the low-temperature ETM regulation strategy discussed in Chapter 4.^[179] Considering the unique requirements for the mechanical tolerance of low-temperature ETM in the production and use environment of flexible photovoltaic cells, various technologies have been employed to enhance their mechanical robustness, and significant progress has been made in recent years.^[180] Nevertheless, compared to those with rigid substrates, flexible PSCs still face more severe challenges regarding mechanical stability. In this Chapter, we highlight various prominent strategies aimed at enhancing mechanical stability, including interlayer engineering, interface structural design, process optimization, and ETMs functionalization.

5.1. The ETMs/perovskite interface

The perovskites exhibit extreme mechanical fragility due to their brittle, salt-like crystal structure.^[181] The mismatch in thermal expansion coefficient between the low-temperature ETM and perovskite results in significant residual stress, which impacts the structural integrity of perovskites and consequently influences their optoelectronic properties and stability. Under stress, active defects and exposed facets may appear on the surface of the ETM, which could potentially react with perovskite and accelerate its deformation.^[176] Therefore, the interface between ETMs and perovskite is crucial for ensuring the mechanical stability of flexible PSCs. Several interface-enhancing strategies have been developed to modify the ETM/perovskite interface, such as adding mechanical buffer layer and building interpenetrating structure, etc.

(1) Interlayer engineering

For the strain accumulation issue at low-temperature inorganic ETMs/perovskite interface, a liquid crystal elastomer (LCE) interlayer is intercalated into the flexible PSCs.^[182] The LCEs are lightly cross-linked polymer networks that synergistically interact with functional inorganic materials, thereby enhancing the mechanical and electrical properties of such hybrid composites. As illustrated in Fig. 26(a), the LCE interlayer is inserted between the perovskite and the ETM. To synthesis the LCE, the LC oligomer with terminated dithiols is initially prepared in the lab by reacting a diacrylate monomer and a dithiol (1,3-propanedithiol) at a molar ratio of 1:2 with basic catalysis. Then, LCE can be obtained through an oxygen-mediated thiol-acrylate click reaction upon UV exposure of the LC prepolymer containing the lab-made LC oligomer and diacrylate monomer, as shown in Fig. 26(b). Such synthesized LEC exhibited a periodic morphology and inserted to the perovskite/ETM interface. The flexible PSCs with a PEN/ITO/SnO₂/LCE/CsFAMAPbI₃/Spiro-OMeTAD/Ag structure achieved a champion PCE of 22.10 %, which was among the highest efficiencies reported for flexible PSCs at that time. To investigate the recovery ability, bending angle test was performed. The reference device lost 7 % of its initial PCE due to perovskite/ETL interface delamination when recovering from a bending angle of 60° to 0°. The flexible PSC with LCE only lost 4 % of the initial PCE after deformation, highlighting the enhanced mechanical tolerance of the perovskite/ETL interface due to the LCE interlayer. Moreover, the relationship between the normalized PCE and various curvature radii for such flexible PSCs after 500 bending cycles as shown in Fig. 26(c), demonstrated that the LCE-based flexible PSC exhibits superior mechanical endurance compared to the reference device. The variation of efficiency with the bending cycles is illustrated in Fig. 26(c). The average PCE of the LCE-based flexible device can maintain 86 % of its initial value, while the reference device shown a significant drop to only 34 % after 5000 bending cycles. Fig. 26(d) was an Internet of Things (IoT) ecosystem based on flexible PSC. The reliability of the integrated device was investigated by tracking continuous photovoltaic under ambient light, as shown in Fig. 26(e). The mechanical bending test was also conducted under continuous illumination to simulate real-life operation, as shown in Fig. 26(f). All of these results verified the excellent stability of LCE-based device. To further inquire into the residual stress caused by the coefficient of thermal expansion mismatch, the depth-dependent grazing incident X-ray diffraction with the 20-sin2φ method was performed. The residual stress of the perovskite on LCE was calculated to be 12.01 MPa, significantly smaller than the reference film's 25.52 MPa. The morphology analysis revealed that the perovskite films detached from SnO₂ after 2500 bending cycles, while the SnO₂/LCE sample exhibited minimal morphological changes. Therefore, anchoring elastic polymer chains of aligned LCE effectively realized the tough adhesion between SnO₂ and perovskite. The presence of LCE can effectively alleviate the interfacial residual stress at the perovskite/ETM interface through aligned molecular stacking and reduce the overall stress distribution of ITO and perovskite by creating elastic interfaces.

Furthermore, silane serves as a widely utilized coupling agent in semiconductor devices to connect inorganic and organic materials. Inspired by this, Wang et al. utilized a protonated amine silane coupling agent (PASCA-Br) to selectively grasp both components by forming the structural unit of a lattice.^[183] The PASCA-Br with R-NH₃Br terminal interlayer was deposited on TiO₂ film by chemical bath deposition method. The schematic diagram of PSCs based on TiO₂/PASCA-Br is shown in Fig. 27(a). The flexible PSCs achieved exceptional device performance by incorporating protonated silane coupling agents, resulting in a remarkable maximum PCE of 17.45 %. Then the mechanical stability was assessed by bending test. From the SEM images illustrated in Fig. 27(b), perovskite films deposited on TiO₂/PASCA-Br showed larger grain size than films deposited on TiO₂. Additionally, after bending test three times, the perovskite on TiO₂/PASCA-Br

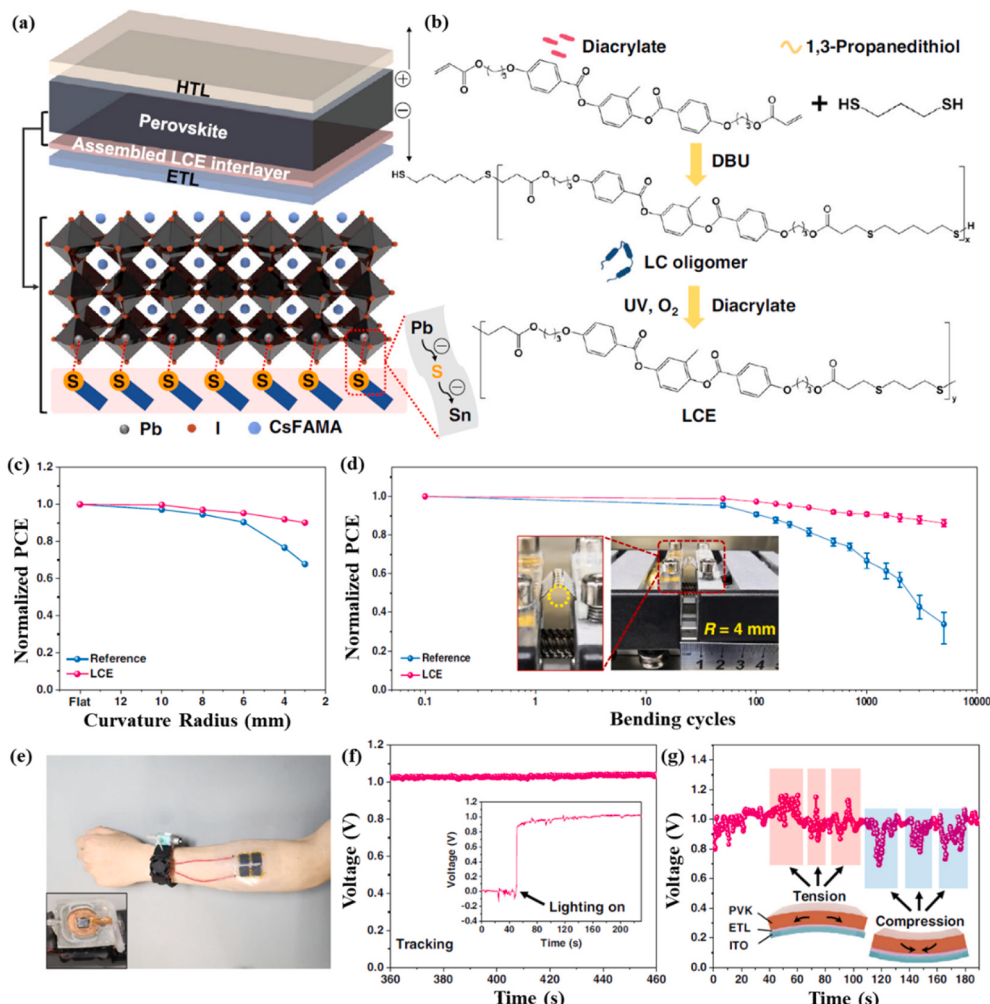


Fig. 26. (a) Schematic illustration of PSC with an assembled LCE interlayer inserted at perovskite/ETM interface; (b) synthetic process of LCE; (c) the normalized PCE of flexible PSCs after 500 cycles of bending with various radii (ranging from flat to 3 mm); (d) the normalized average PCE for flexible PSCs as a function of bending cycles (bending radius: $R = 4$ mm); (e) photograph of the IoT system using flexible PSCs in ambient light; (f) the time dependent voltage for continuous tracking of the IoT system; (g) Mechanical bending test of the wearable device under continuous illumination.^[182] Copyright 2023, Springer Nature.

exhibited only minimal cracking in comparison to the perovskite on TiO₂, thereby confirming its exceptional resistance to bending. The PCE values as a function of bending angles are depicted in Fig. 27(d). Similarly, the PASCA-Br included device demonstrated low sensitivity to bending angles. Even when subjected to a 60° bend, the PCE remained at 98 % of its initial value. Furthermore, the Young's modulus of perovskite films on TiO₂ and TiO₂/PASCA-Br were calculated to be 3000 MPa and 3770 MPa, respectively. The significant released mechanical deformation was attributed to the molecular-level PASCA-Br interlayer, which provided effective mechanical buffering. The alkyl chain PASCA-Br imparted enhanced flexibility to the interfacial connection, enabling it to effectively withstand external mechanical forces and making it suitable for various inorganic and organic layers in flexible devices. Moreover, in rigid PSCs, the iodine-terminated self-assembled monolayer (I-SAM) has been proven to increase adhesion toughness at the interface between ETMs and perovskite thin film.^[184] Subsequently, Padture et al. employed the SAM to mechanically reinforce the ETM/perovskite interface in flexible PSCs.^[185] The interfacial toughness values, G_C , of the perovskite on different charge transporting layer were measured, as shown in Fig. 27(c). The ETM/perovskite interface was relatively tough, with a fracture energy of 1.91 ± 0.48 J m⁻². Incorporation of SAM at this interface leads to an approximate 50 % increase in the fracture energy, resulting in a value of 2.83 ± 0.35 J m⁻². To further investigate the mechanical reliability, finite element modeling (FEM) was

performed to estimate the strain-energy-release rate (G) between the adjacent layers. Fig. 27(e) was the schematic diagrams of flexible PSC with an initial surface crack (left) and channel and interfacial cracks (right) after bending. The functional relationship between the interface crack size c and G was illustrated in Fig. 27(f). From above calculation, the steady-state G of ETM/perovskite layers (3–4 layers) was specified as 1.11 J m⁻². According to fracture criteria, the ETM and perovskite interface may crack when $G \geq G_C$. The introduction of SAM increased the G_C , thereby rendering the channel cracking and subsequent interfacial cracking more challenging, consequently enhancing the mechanical reliability of the device.

(2) Interface structure design

Apart from the interlayer engineering, the perovskite/ETM contact interface structure also influence the mechanical robustness of flexible PSCs. Zhou et al. successfully synthesized an interpenetrating perovskite/ETM interface. The detailed formation process was illustrated in Fig. 28(a). The as-prepared SnO₂-nanocrystals colloidal solution with excess organic halide was spin-coated on the substrate to form the FAI-incorporated SnO₂ (FI-SnO₂) ETM. Then the perovskite film was deposited, followed by annealing process. During thermal treatment, the excess PbI₂ in perovskite reacted with the organic halide in the FI-SnO₂, leading to a partial infiltration of the perovskite phase into FI-SnO₂. The

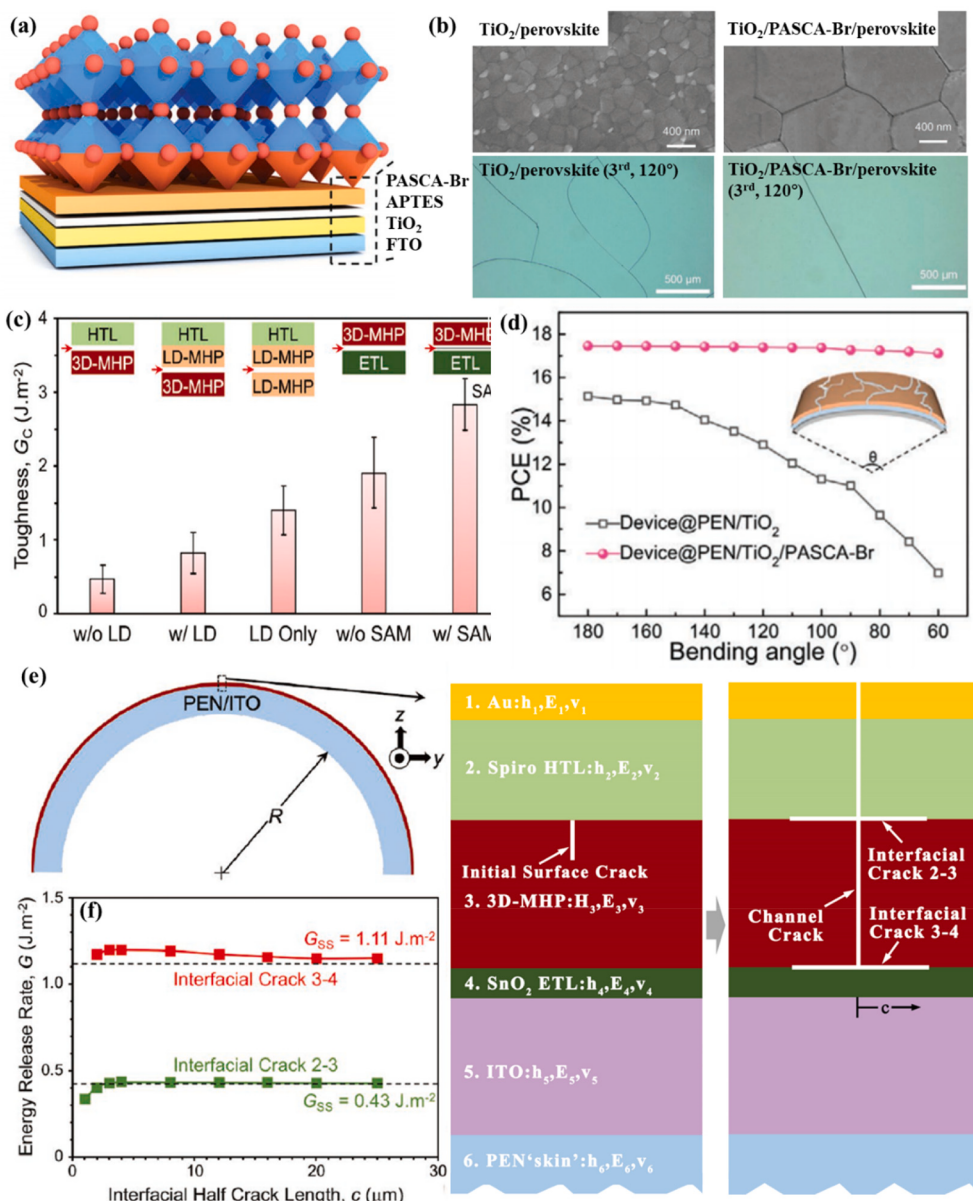


Fig. 27. (a) A schematic of PSCs based on TiO_2 and PASCA-Br layers; (b) Top SEM morphologies of perovskite films on different substrates (top) and optical images of different perovskite films after bending test for three times (bottom).^[183] Copyright 2020, Wiley-VCH. (c) Measured interfacial toughness of different interface.^[185] Copyright 2022, Wiley-VCH. (d) PCE changes under different bending angles.^[183] Copyright 2020, Wiley-VCH. (e) The schematic illustrations of flexible PSC with an initial surface crack (left) and channel and interfacial cracks (right) after bending (hi: values of thickness, E_i : isotropic Young's modulus, v_i : Poisson's ratio); (f) FEM calculated $G(c)$ for charge transporting layer and perovskite interfacial cracks.^[185] Copyright 2022, Wiley-VCH.

cross-sectional SEM images in Fig. 28(b) illustrated the dense polycrystalline microstructures of perovskite deposited on FI- SnO_2 and pristine SnO_2 ETMs. To prove the interpenetration of perovskite and ETM, the cross-sectional transmission electron microscope characterization and energy-dispersive X-ray spectroscopy analysis were performed, as shown in Fig. 28(c). The thickness of the FI- SnO_2 film was approximately double that of the pristine SnO_2 , consistent with the cross-sectional SEM images (~ 95 nm vs ~ 45 nm). The Pb element, representing perovskite, is uniformly observed in FI- SnO_2 , indicating the interpenetration between SnO_2 and perovskite. In contrast, in the perovskite/pristine SnO_2 structure, there was a sharp transition in element distribution between each layer without notable interpenetration. Based on these observations, it can be reasonably deduced that an interfacial reaction occurred between excess PbI_2 and organic halide in perovskite and FI- SnO_2 respectively, resulting in the formation of the interpenetrating interfaces. On the basis, the operational stability and

mechanical endurance of flexible PSCs were assessed by cyclic-bending fatigue test. Fig. 28(d) illustrated that the device based on FI- SnO_2 exhibited a high mechanical tolerance. The schematic illustrations of perovskite/ETMs/ITO structure under different bending states and bending cycles were illustrated in Fig. 28(e). The compressive strain in the concave state will transform into a peel-off stress perpendicular to the perovskite/ETM interface. Thus, the interface morphology changes of flexible PSCs after bending cycles served as an analysis index. Fig. 28(f,g) were cross-section SEM images of flexible PSCs based on different ETMs after undergoing bending. After 1000 bending cycles, the perovskite film began to exhibit delamination from the pristine SnO_2 layer, while the film on FI- SnO_2 ETM remained structurally unchanged. Upon reaching 2500 bending cycles, noticeable delamination was observed in the pristine perovskite/ SnO_2 film, whereas the interface between perovskite and FI- SnO_2 remained intact except for some cracks appearing in the perovskite. The improved mechanical durability is due

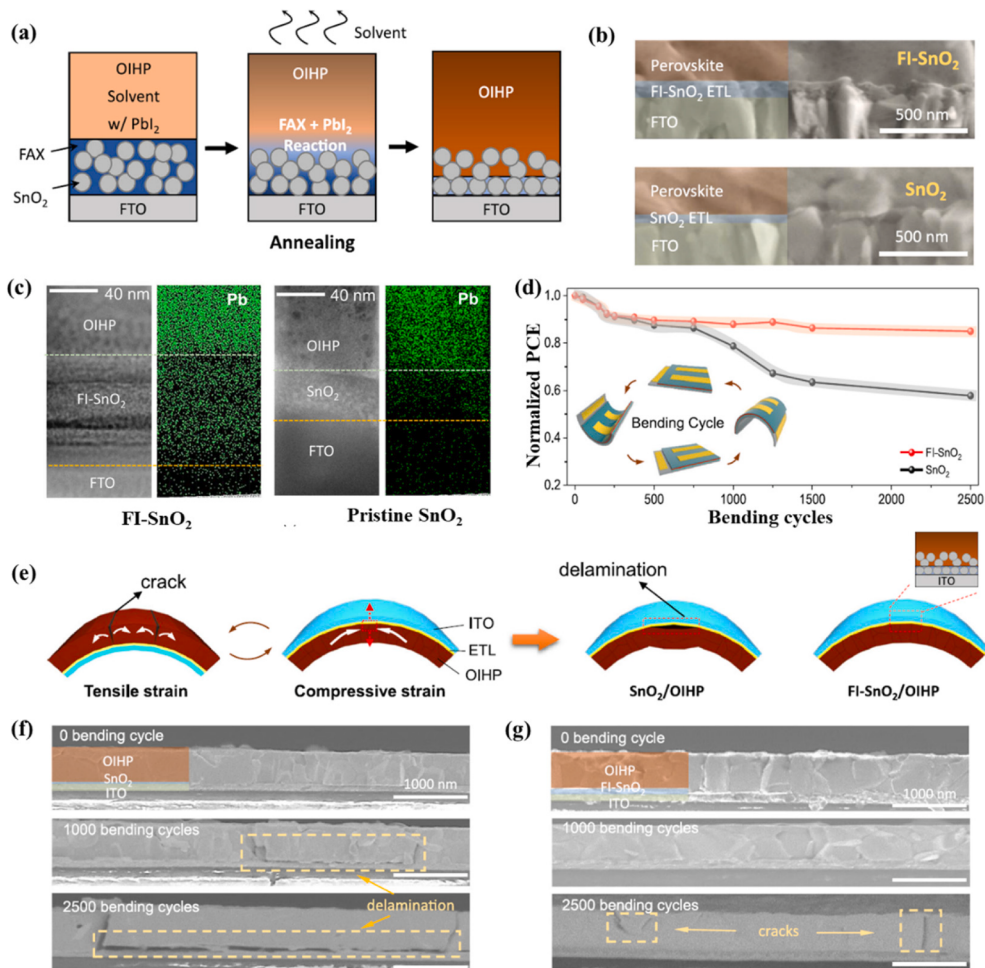


Fig. 28. (a) Formation process diagram of perovskite/FI-SnO₂ interface; (b) cross-sectional SEM images of perovskite on FI-SnO₂ and pristine SnO₂ ETMs; (c) cross-sectional STEM image and EDX Pb-element mapping of perovskite on FI-SnO₂ and pristine SnO₂ ETMs; (d) durability test of flexible PSCs; (e) schematic illustrations of perovskite/ETMs/ITO structure under different bending states (left panel) and bending cycles (right panel); cross-section SEM images of flexible PSCs based on (f) pristine SnO₂ and (g) FI-SnO₂ ETMs after different bending cycles.^[186] Copyright 2021, Springer Nature.

to the interpenetrating structure of perovskite/ETM interface, which exhibited a higher level of damage tolerant compared to sharp interfaces between two materials.

5.2. The ETMs/substrate interface

As mentioned above, for flexible PSCs, the soft substrate not only necessitates a low production temperature but also poses challenges in terms of production complexity.^[187] The pliability and malleability of flexible substrates result in bending or distortion when they are suctioned onto the vacuum chuck of a spin-coater or the vacuum baseplate of a bar-coater, leading to nonuniform deposition and compromising various post-treatment effects. The attachment of a flexible substrate to a rigid substrate can mitigate these issues. However, the presence of an air gap between the flexible and rigid substrates impedes heat transfer behavior, while disregarding the distinct thermal expansion coefficients of the flexible substrate. Consequently, this leads to poor mechanical resistance at the ETM/substrate interface and adversely affects the subsequent film formation quality of perovskite and other layers. Jung et al. reported a van der Waals stacking (vdWS) process that enabled the production of uniform and highly crystalline films on flexible substrates through consistent heat transfer during the annealing procedure.^[188] The step-by-step procedures of the vdWS-induced lift-off process were illustrated in Fig. 29(a). The use of PDMS, which has a higher thermal conductivity than air, facilitated the adhesion of rigid glass and flexible

PEN substrates, thereby promoting efficient heat transfer. The ETMs, along with the subsequently deposited perovskite, can effectively evaporate the solvent uniformly across all areas. The vdWS process optimized the contact between the ETM/substrate interface, thereby enhancing the mechanical stability of flexible PSCs. Moreover, a type of inverted nanocone (i-cone) structures were designed to construct efficient, flexible and mechanically robust PSCs.^[189] The device fabrication process by two-step evaporation was illustrated in Fig. 29(b). Based on the i-cone structured substrate, the PCE of PSCs improved by 37 %. The flexibility of the i-cone based PSCs was also analyzed. Fig. 29(c) illustrated the bending setup photograph. The dependence of the device PCE on the bending cycles was shown in Fig. 29(d). Notably, the efficiency of the i-cone device remained unchanged after 200 cycles, retaining 95 % of its initial value, while the device based on flat substrate experienced a significant decrease to approximately 70 % of its initial value. The Jsc and PCE were also assessed at different incident angles, as shown in Fig. 29(e). Compared to the flat device, the i-cone device exhibited an 80 % improvement in efficiency when subjected to a 60° incident angle. The stresses and strains of the device were analyzed by COMSIL software. The maximum stress in the flat device was specifically 900 Pa, whereas the i-cone device only experienced a maximum stress of 500 Pa. Therefore, the three-dimensional nanostructured substrate could effectively reduce stress and strain between ETMs and the substrate layer.

The strain release strategies mentioned above should not be the sole

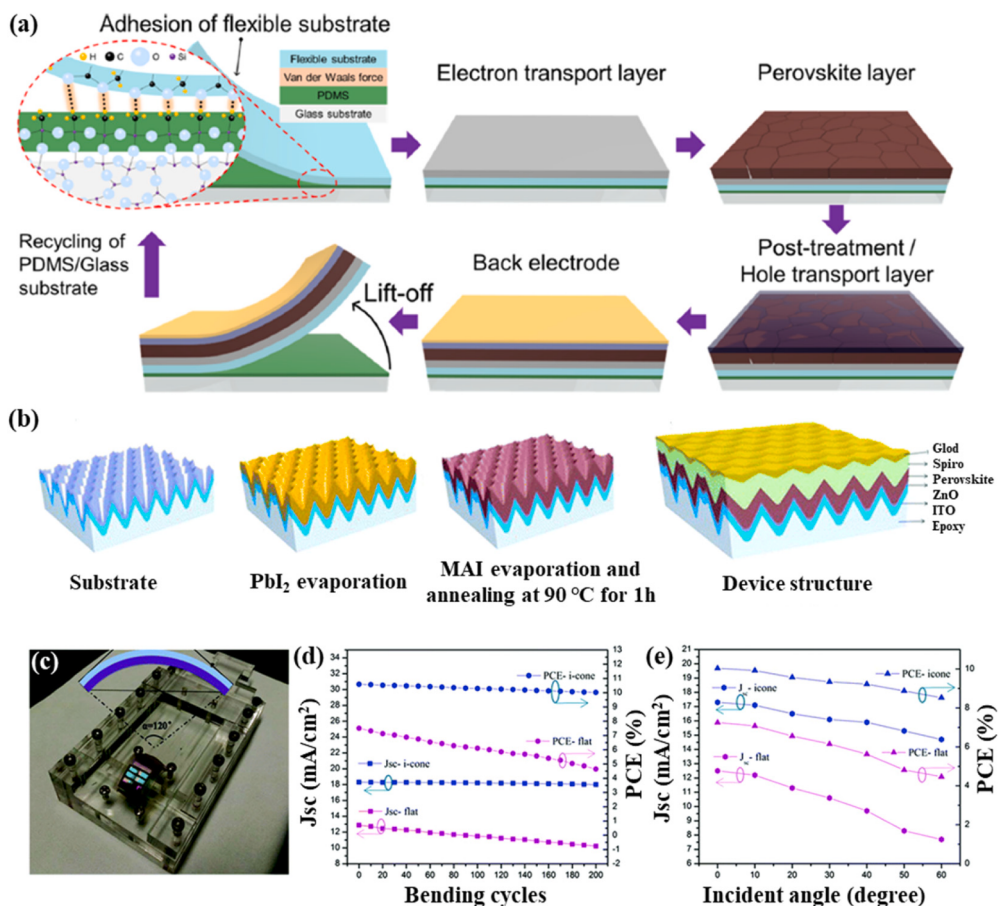


Fig. 29. (a) Schematic diagram of van der Waals lift-off process.^[188] Copyright 2022, American Chemical Society. (b) Schematic fabrication process of PSCs based on the i-cone-epoxy substrate; (c) photograph of the bending setup; (d) efficiency stability of PSCs depending on bending cycles; (e) angular PV measurements of PSCs based on different substrates.^[189] Copyright 2016, Royal Society of Chemistry.

focus; attention should also be given to the adhesion between ETMs and flexible substrates. The inadequate bonding strength at the interface of ETM/substrate can lead to severe mechanical damage in flexible PSCs. Seok et al. prepared a SnO₂-TiO₂ hybrid ETM by incorporating a specific quantity of TiO₂ nanosol, serving as an inorganic binder, into a colloidal solution of SnO₂.^[190] Due to the presence of peroxide functional groups on the surface of TiO₂ nanosols, the hybrid ETM demonstrated a robust adhesion strength, thereby enhancing the mechanical reliability of flexible PSCs.

5.3. The ETMs functionalization

Due to the mismatch in thermal expansion coefficients between the ETM, substrate, and perovskite, the mechanical stability of flexible PSCs is compromised. To address these challenges, extensive efforts have been dedicated to optimizing the fundamental mechanical properties of ETMs. Colloidal SnO₂ has become the mostly used ETM in n-i-p PSCs. Zhang et al. proposed a simple and effective strategy to modify SnO₂ by incorporating halide anions.^[191] As shown in Fig. 30(a), a series of different potassium halide additives (KF, KCl, KBr, and KI) were incorporated into the colloidal SnO₂ precursor. Based on the F-SnO₂ ETM, the devices exhibited excellent PCE of 22.1 %. The mechanical stability of flexible PSCs was evaluated by applying bending cycles with a radius of 4.71 mm, as illustrated in Fig. 30(b). The F incorporating devices demonstrated exceptional mechanical stability, with over 86 % of the initial PCE retained after 10,000 cycles. This could suggest that the application of F-SnO₂ in PSCs can effectively mitigate the mismatch in thermal expansion coefficient, thereby reducing residual stress and

suppressing stress-induced device decomposition.

Not only can inorganic functionalized ETMs enhance the mechanical stability of flexible devices, but organic materials have also demonstrated their ability to improve the mechanical tolerance of ETMs. Specifically, the PM6: CH1007: PCBM ternary blend organic ETM was deposited on perovskite to construct the p-i-n PSCs. The hybrid bulk heterojunction layer exhibited enhanced mechanical robustness compared to single PCBM. The PCE evolution of flexible PSCs in bending tests, including parallel, vertical, and diagonal orientations, confirmed the aforementioned conclusion. As shown in Fig. 30(c), the devices exhibited no significant decrease in efficiency after undergoing 1000 cycles of bending in various directions. The efficiencies remained at approximately 97 %, 94 %, and 98 % of their initial values for the respective bending directions. This ternary organic blend ETM had an amorphous network of polymer chains, thus potentially strengthening the intermolecular connections and thus tolerating greater mechanical deformation. Moreover, the 3-aminopropionic acid hydroiodide (3AAH) additive was used to modify the SnO₂ ETM.^[176] As shown in Fig. 30(d), the device with ITO/3AAH-SnO₂/FAPbI₃/Spiro-OMeTAD/Ag structure was constructed. To analyze stress of device, the depth-resolved grazing incident X-ray diffraction was performed. Fig. 30(e) was the linear fit of $20\sin^2(\Psi)$ for perovskite films deposited on SnO₂ and 3AAH-SnO₂ ETMs. The diffraction peaks shifted towards higher degrees as Ψ increased, indicating a transition in the perovskite from tensile stress to slight compressive strain, which benefits device stability. The mechanical properties were also evaluated by Peak Force Quantitative Nanomechanical Mapping (PFQNM). As illustrated in Fig. 30(f), the average Derjaguin-Muller-Toporov (DMT) modulus of 3AAH-SnO₂/perovskite

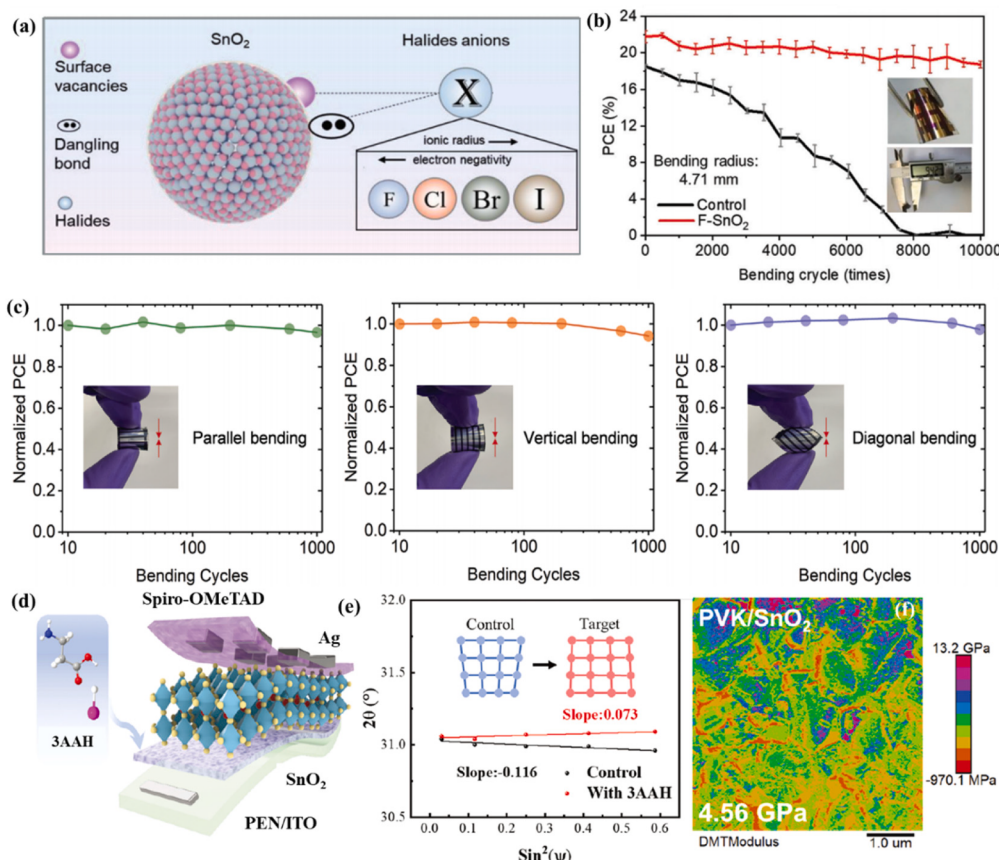


Fig. 30. (a) Schematic of the chemical interaction between SnO_2 and halides; (b) mechanical stability of the flexible PSCs with control and F- SnO_2 .^[191] Copyright 2023, Wiley-VCH. (c) Efficiency evolution of flexible PSCs as a function of varying bending directions and cycles.^[192] Copyright 2021, Wiley-VCH. (d) Illustration of flexible PSCs; (e) linear fit of $2\theta - \sin^2(\Psi)$ for perovskite deposited on SnO_2 and 3AAH- SnO_2 ETMs (0: diffraction; ψ : tilting angles). (f) DMT modulus of perovskite based on 3AAH- SnO_2 ETM.^[176] Copyright 2023, Wiley-VCH.

film was 2.89 GPa, which was lower than that of the pristine SnO_2 /perovskite (4.56 GPa), indicating a higher level of mechanical flexibility for 3AAH- SnO_2 /perovskite film. The addition of 3AAH into SnO_2 ETM enlarged the thermal expansion coefficient, thereby alleviating the interface mismatch issue. As a result, the 3AAH-based flexible PSCs achieved excellent mechanical stability.

The latest research has revealed that the structural design of ETM is anticipated to enhance its mechanical properties. For instance, Zhang et al. designed a core@dual-shell structure based on SnO_2 nanoparticles and constructed a highly efficient flexible PSCs with strong mechanical endurance.^[193] The prepare process of the core@dual-shell SnO_2 was shown in Fig. 31(a). The additives of potassium thiocyanate (KSCN) and (polyethylene oxide) PEO was introduced in the SnO_2 colloidal solution, then resulting in the formation of sea urchin shaped SnO_2 particles with core–shell structure. The influence of KSCN and PEO on the particle size distribution of SnO_2 in colloidal solution was analyzed using dynamic light scattering (DLS) (Fig. 31(b)). The original SnO_2 colloid showed three Gaussian distributions: 79.6 % consisted of small particles (10 ± 10 nm), 13.8 % consisted of medium-sized particles (0.2 ± 0.1 μm), and 6.6 % consisted of large particles (4 ± 2 μm). The single-shell SnO_2 formed by adding only PEO or KSCN to the colloidal solution had minimal impact on the proportion of medium and large clusters observed. However, when forming the double-shell structure using KSCN-PEO, a bimodal distribution in cluster sizes emerged with 97 % composed of small clusters and only 3 % comprising medium-sized clusters. The small particles induced the dense ETM layer and the mechanical durability for core@dual-shell SnO_2 was enhanced. The bending test was performed as shown in Fig. 31(c). The devices based on KSCN-PEO functionalized SnO_2 exhibited remarkable mechanical

durability, maintaining over 83 % of their initial PCE even after undergoing more than 4700 bending cycles. The perovskite film showed minimal morphological changes, further confirming the enhanced mechanical durability, even after being subjected to 1000 bending cycles. Such excellent mechanical endurance can be attributed to the unique structure of ETM, in which PEO served as a bridging agent between SnO_2 and the perovskite bottom layer, ensuring optimal interface contact. Additionally, Dong et al. designed an amorphous F-doped TiO_x (F-TiO_x) caulked crystalline SnO_2 composite ETM.^[194] As shown in Fig. 31(d), the F-TiO_x filled the voids between SnO_2 particles, which not only enhanced the electron mobility, but also enlarged the surface roughness of ETM. Then the repeated cyclic-bending fatigue tests were performed to analyze the mechanical reliability. As shown in Fig. 31(e), after 1000 cycles, both of SnO_2 and F-TiO_x- SnO_2 ETM based flexible PSCs demonstrated exceptional mechanical durability. However, during the continuous bending test, flexible PSCs based on composite ETM exhibited noticeable resistance to bending. Due to the interfacial enhancement by F-TiO_x caulked SnO_2 composite ETM, flexible PSCs demonstrated a remarkable mechanical reliability, maintaining 82.11 % of their initial PCE after 4000 bending cycles.

5.4. Discussion and perspective

The mechanical stability of flexible PSCs is a critical bottleneck in determining their future commercial application. Currently, the focus lies on enhancing the mechanical tolerance at the perovskite and its adjacent functional layers. However, it is important to note that all layers and interfaces within PSCs have to pass IEC 61646 standard test protocols, which places significant demands on the mechanical

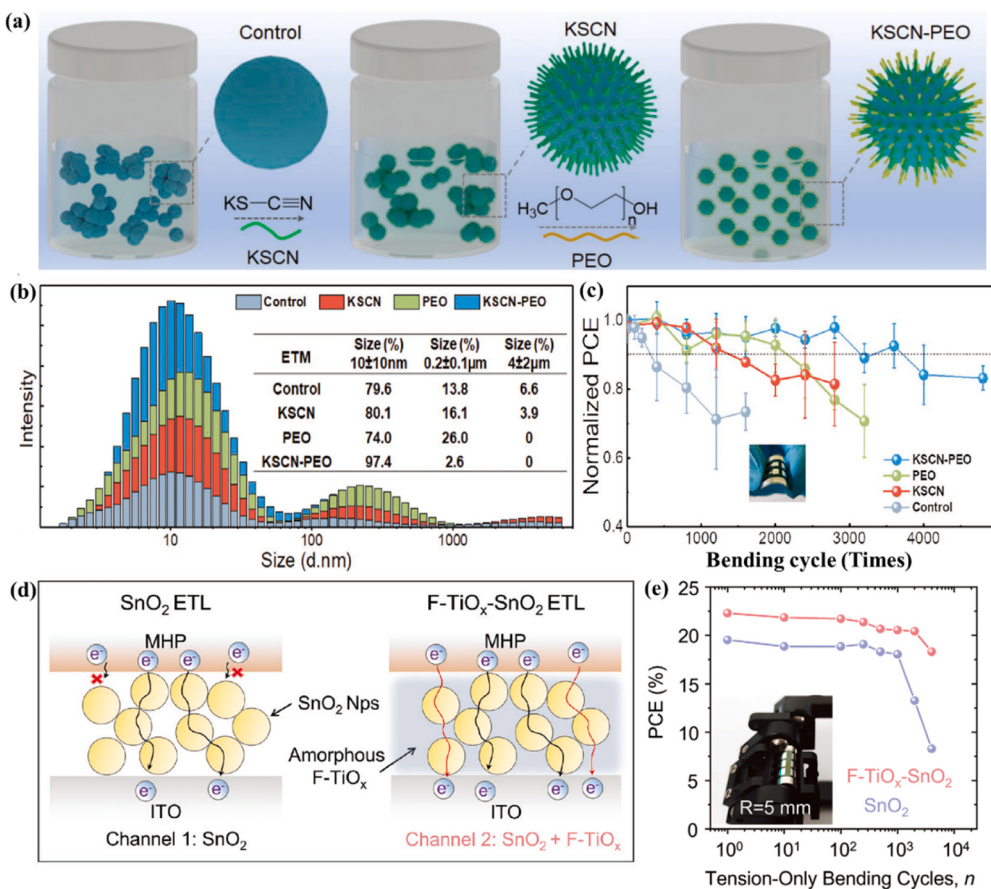


Fig. 31. (a) Schematic illustration of the synthetic process of the core@dual-shell nanostructured SnO_2 ; (b) The Dynamic light scattering (DLS) characterization of colloidal solution based on control, KSCN, PEO, and KSCN-PEO- SnO_2 ; (c) mechanical bending stability of the flexible PSCs. [193] Copyright 2022, Wiley-VCH. (d) Schematic of photogenerated electrons transport within different ETMs; (e) the PCE change as a function of bending ($R = 5$ mm). [194] Copyright 2023, Wiley-VCH.

tolerance of low-temperature ETMs. To provide enlightenment on the improvement of current strategies for controlling mechanical reliability and invention of new optimization schemes, a comprehensive analysis of the mechanical challenges is specifically listed in Fig. 32. Due to their ionic solid nature, perovskites inherently differ from commonly used ETMs; interfaces pose the main challenge towards addressing the mechanical failure issue. The mechanical stability would be enhanced by employing multifunctional materials at the interface to establish chemical bonds between the two layers. Organic molecules function as highly effective “molecular adhesives”, binding tightly to the ETMs and perovskite layers. This effectively addresses the issue of out-of-plane delamination. Concurrently, interfacial modifier should also alleviate stresses generated within the perovskite by absorbing and releasing compressive and tensile stresses throughout thermal cycling. In general, the anchoring groups of these materials lead to covalent interactions with the ETM surface, which can provide flexibility for in-plane stresses. In addition, the weak adhesion of low temperature ETM to the substrate interface not only affects its mechanical toughness but also hinders its overall performance. The optimization of the fabrication process has been proven to improve surface adhesion. Analogously, surface treatments can be applied to modify interfacial properties such as roughness or chemical interaction, leading to improved adhesion. Despite its significance, the mechanical stability of the ETM/substrate interface has been somewhat oversight. Actually, optimizing the mechanical properties (e.g., coefficient of thermal expansion, flexibility) of the low-temperature ETMs themselves hold immense potential in improving device’s mechanical tolerance.

Considering that the importance of mechanical reliability for the low-temperature ETMs is increasingly moving in the focus, a further and

deeper understanding of its origin, impacts, and means for control are essential to pursue more stable and push flexible PSC closer to commercialization.

6. Large-Area Low-Temperature ETMs toward industrial modules

6.1. Strategic significance of large-area low-temperature ETMs

Perovskite photovoltaic technology toward commercialization relies on high PCE, long lifetime, and low-toxicity in addition to development of large-area fabrication protocols, and a positive cost-performance assessment. The past decade, small-scale ($\sim 0.1 \text{ cm}^2$) PSCs, constructed by the favored lab-scale solution-processed techniques, have yielded outstanding PCEs over 25 %. Indeed, the facile synthesis superiority of perovskite materials is well established, which promotes the interest to bring PSCs closer to commercialization. Moreover, leveraging existing industrial processes can facilitate the transition from the laboratory to the industry line. Therefore, PSCs have great potential to achieve large-scale industrial production, which will ultimately facilitate their rapid deployment. However, a large efficiency gap still exists between small- and large-area PSC devices. Worldwide research efforts have been directed toward developing scalable fabrication strategies for perovskite solar modules with emphasis focused on perovskite absorber layer. While the large-area low-temperature ETMs is also one of the crucial issues toward industrial modules, which directly affect module efficiency and interface stability, and have important strategic value for reducing cost and mitigating energy and environmental problems.

From the perspective of industrialization, ‘cost reduction and

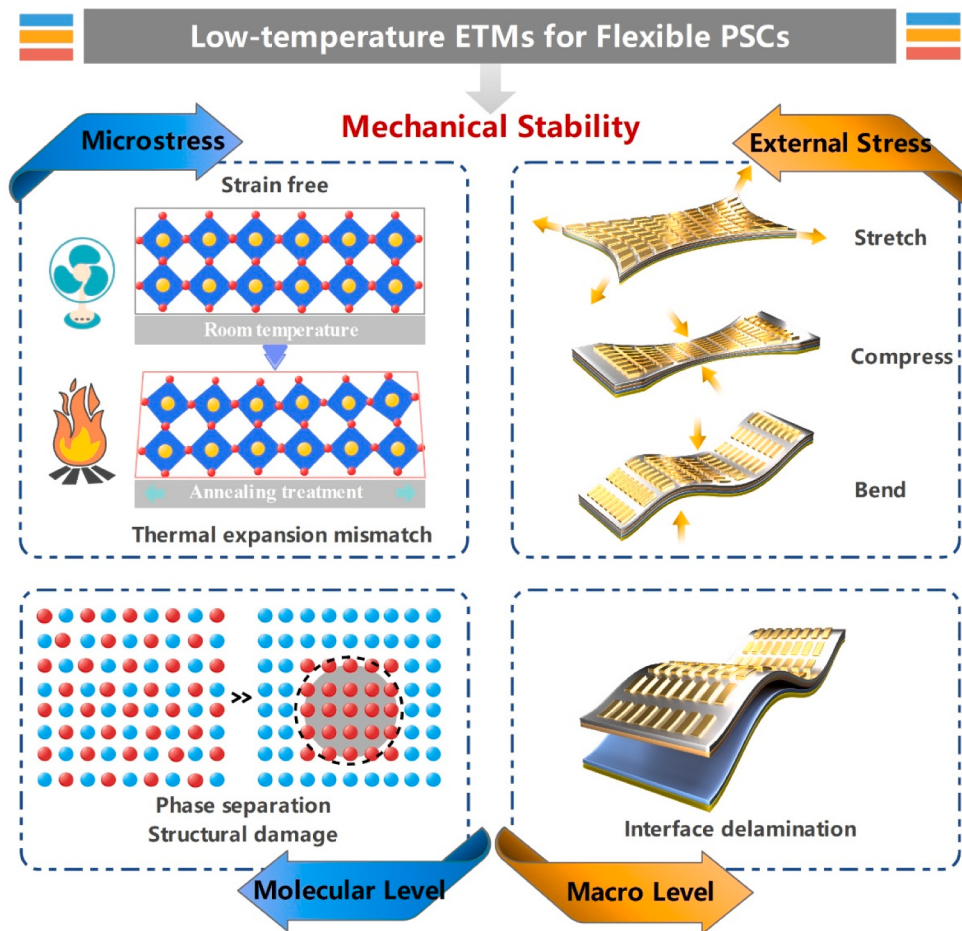


Fig. 32. Schematic diagram of stress origin and mechanical stability issue.

efficiency increase' is the core essence of photovoltaic industrialization, and also the ultimate pursuit of photovoltaic enterprises. Generally, the successful preparation of perovskite modules depends not only on the perovskite light absorption layer but also on the large-scale charge transport layer, especially ETMs. The complete cost analysis for rapid spray plasma processing shown in Fig. 33 indicates that the cost of electron transporting layer is high, comparable to ITO.^[195] Although the low temperature synthesis process of perovskite material greatly reduces the construction cost of large-size components, the introduction of low-temperature ETMs not only simplifies the preparation process, but also makes the processing of large-area modules more convenient, which further reduces the cost. The cost-performance analysis of perovskite solar modules proposed by Prof. Han pointed out that the

low-temperature process of PSCs gives potential for ultra-low-cost production. For this reason, the low-temperature ETMs are preferable for upscaling purposes.

The environmental impact of low-temperature ETMs in perovskite modules throughout their life cycle is also the focus of current attention. Considering the environment, energy consumption and carbon footprint, the ETMs of low-temperature processing is more favorable. The energy profile of 1 m² of the lanthanum (La)-doped BaSnO₃ (LBSO) perovskite module is shown in Fig. 34. The gray part represents ETL calcining process. It is obvious that the high-temperature calcining step is the most pronounced, which is the most significant contributor for climate change (68.2 %), fossil depletion (69.8 %), ozone depletion (69.2 %), marine eutrophication (60.8 %), human health effects (59.9

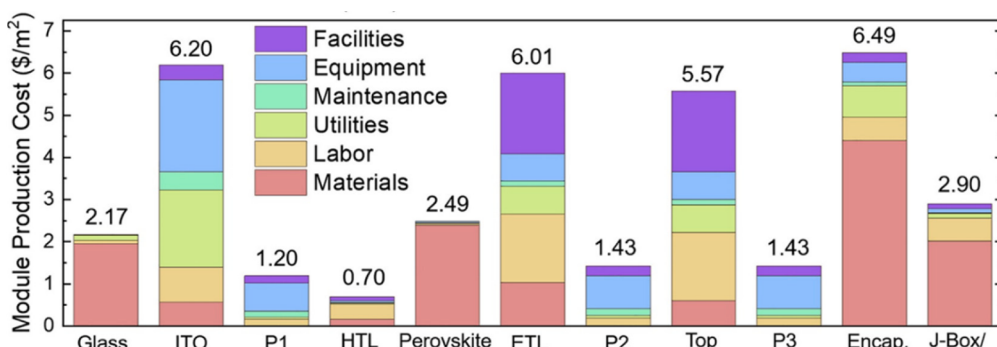


Fig. 33. The cost analysis for perovskite module production process. ^[195] Copyright 2020, Elsevier.

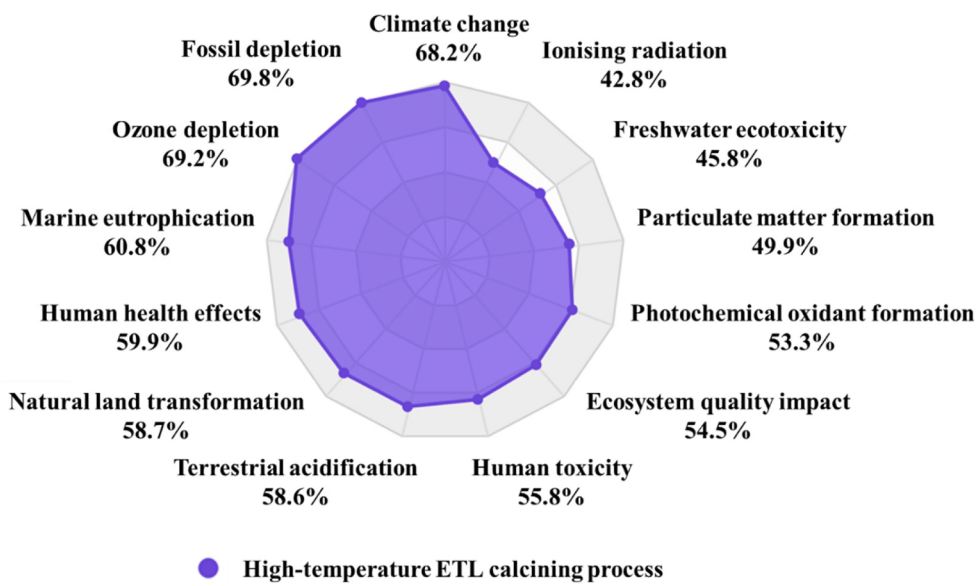


Fig. 34. The energy profile of 1 m² of LBSO perovskite module.

%), natural land transformation (58.7 %), terrestrial acidification (58.6 %), human toxicity (55.8 %), ecosystem quality impact (54.5 %), photochemical oxidant formation (53.2 %), particulate matter formation (49.9 %), freshwater ecotoxicity (45.8 %), ionising radiation (42.8 %) during PSC production.[196] While SnO₂-based perovskite module has better environmental performance than other typical perovskite modules, including metal oxide module, mixed-cation module, defect-engineered module, semi-transparent module and so on. Because it circumvents the high-temperature and lengthy heating processes.

In addition, the primary energy consumption and the carbon footprint are also important concerns for large-area photovoltaic modules. Fig. 35 illustrate the primary energy consumption and the carbon footprint as well as their distributions for TiO₂ perovskite module and ZnO perovskite module. When considering the primary energy consumed in the manufacturing process, the long-time and high-temperature annealing process results in the highest energy demand for TiO₂ modules.[197] Therefore, the application of low-temperature ETMs could avoid the sintering process and effectively reduce the primary energy consumption. When we consider the carbon footprint caused by the manufacture process, the high-temperature treatment steps similarly occupy a large proportion. The resemblance manufacturing distribution in the primary energy consumption and the carbon footprint demonstrates the importance to change the manufacturing procedure. The perovskite modules with low-temperature ETMs could eliminate the annealing step and close to the requirements of environmentally sustainable photovoltaic modules. Therefore, development of large-area low-temperature ETMs is of paramount importance toward industrialization.

6.2. Current status of large-area low-temperature ETMs

Over the past several years, many scalable solution-based and vapor-phase strategies have been developed. Advances have also been made in improving ETM quality, interface contacts, and module manufacturing processes. These efforts have led to rapid progress in the development of perovskite modules. To date, the highest certification efficiency of perovskite modules is 17.9 % at 804 cm² scale.[198] Although the specific preparation details are not publicly available, statistics of published perovskite module literature listed in Table 5 show that the small-size perovskite module based on the low-temperature SnO₂ ETM has a high efficiency of 18.13 % on an area of 21 cm² with a Glass/FTO/SnO₂/PCBM/MAPbI₃/Spiro-OMeTAD/Au structure.[199] Low-temperature

SnO₂ ETM shows unique advantages in terms of preparation methods (i.e., solution processing, sputtering), cost and stability. As can be seen from the Table 5, low-temperature SnO₂ ETM has become the preferred electron transport layer for perovskite modules so far.

Generally, the perovskite modules need the series connections of multiple subcells and the P1, P2 and P3 interconnection, when perovskite cells are scaled up to larger areas, as shown in Fig. 36(a). Fortunately, the complex device structure does not introduce additional high-temperature processing, which make it possible to realize flexible perovskite cell modules.[202] Flexible cells prepared on ultra-thin and lightweight substrates could fully meet the needs of the emerging flexible electronics market and find application scenarios that cannot be realized by traditional photovoltaic devices. Moreover, flexible cells can be prepared by roll-to-roll printing process and suitable for mass production, as shown in Fig. 36(c).[201] Various low-temperature ETMs have been used to construct the flexible perovskite modules. In 2015, the first ever flexible perovskite photovoltaic modules with low temperature processed TiO₂ scaffold and low temperature plasma assisted ALD compact layer was demonstrated. Prof. Qi and co-workers used low-temperature TiO₂ as ETM to fabricate fully low temperature process flexible perovskite modules with a size of 5 × 5 cm².[203] Moreover, the low-temperature solution-processed SnO₂/mesoporous-TiO₂ composite ETM was also applied to construct fully laser-patterned flexible perovskite solar cells and modules, which obtained a PCE of 8.8 % with active area over 12 cm².[204] In the same year, a low-temperature pre-synthesized crystalline SnO₂ was used as an electron transport layer for a 5 × 5 cm² flexible PSC module, which achieved a PCE of 12.31 %. On the basis, these researchers introduced K ions in SnO₂/perovskite interface and obtained a high PCE of 15.22 % for a flexible perovskite module based on slot-die-coated Alfa-SnO₂ substrate.[60] Nowadays, remarkable progress has been achieved in the development of flexible perovskite modules due to the successfully exploration of low-temperature processed charge transport layers. It is worth mentioning that due to its excellent stability and suitable band gap structure, SnO₂ may be the best choice for electron transport layer for flexible perovskite modules.

6.3. Development tendency of large-area low-temperature ETMs

Rapid development of PSCs during the past several years has made this photovoltaic technology a serious contender for industrial application. To push PSC technology from the laboratory to industry scale, the future development tendency may focus on scalable fabrication of large-

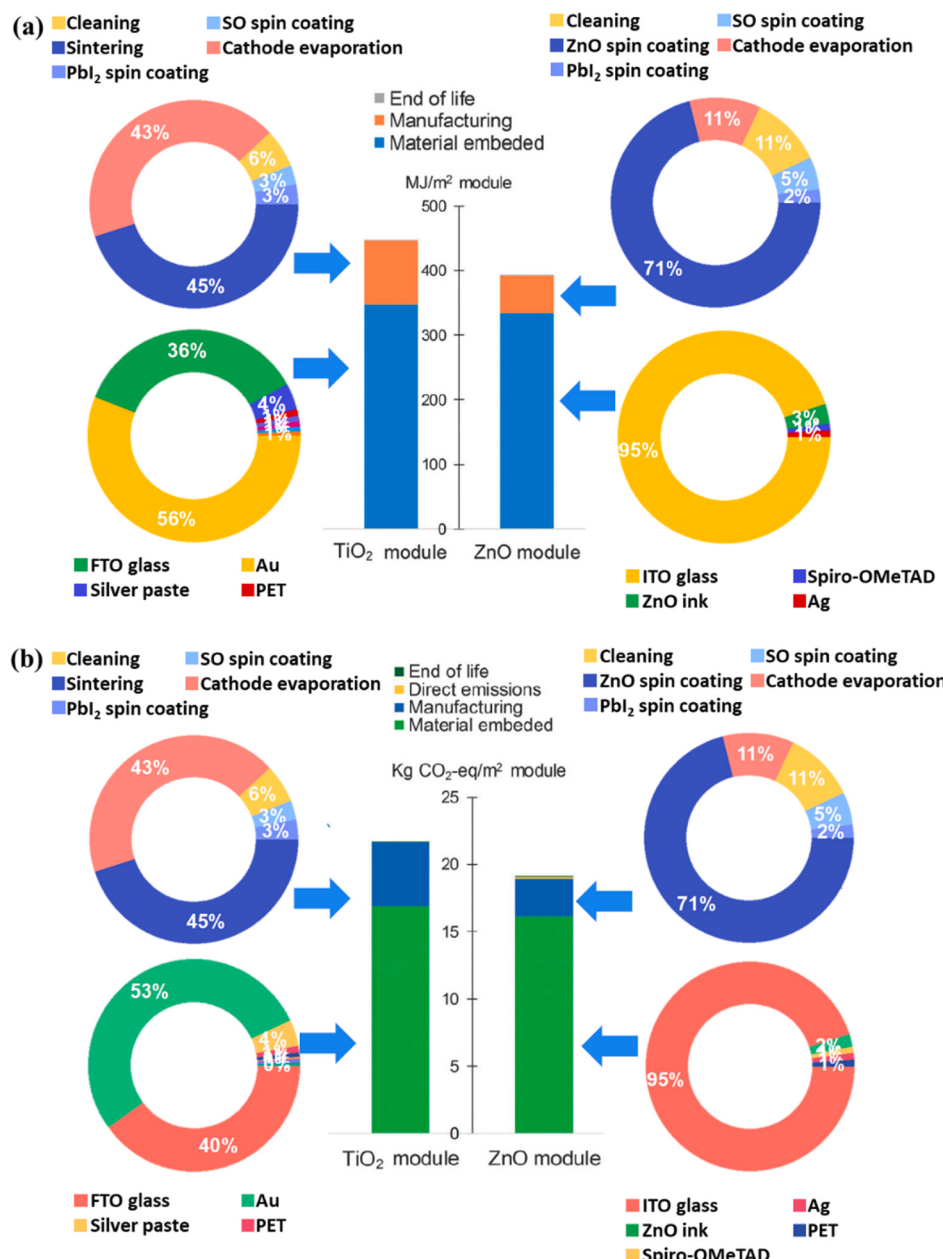


Fig. 35. (a) The distributions of the primary energy consumption for fabricating two perovskite modules, (b) the distribution of the carbon footprint of two perovskite modules. The pie charts don't show the items with the contribution less than 1%. [197] Copyright 2015, Royal Society of Chemistry.

area low-temperature ETMs with excellent crystal quality and minimum negative environmental impact. The details are summarized below.

- *Diversified large-scale preparation technology with high deposition quality.* The first and foremost factor for successful scaling up of PSCs from laboratory-scale cells to industry-relevant modules is to uniformly coat a compact ETMs over a large area with high homogeneity and good optoelectrical properties. Therefore, further advances toward practical application require continuous innovations in developing inks and processes for ETMs in the device stack, particularly in low temperature.
- *Environmentally friendly materials and processes.* Reducing the negative environmental impact from large-area ETMs and processing steps should also be considered carefully for perovskite module to be adopted by industry. For example, the various solvents used during production should better to rigorously evaluated, but it is

challenging to form a standard green chemistry for ETMs deposition. Even with a greener solvent, the use of a toxic solute may also alter the hazard level of the precursor solution.

- *Large-scale and high-precision material property assessment.* Besides the aforementioned aspects, the characterization techniques compatible with large-area ETMs would be of concern, which may provide useful feedback to these recent advances. On the basis, the large-scale film uniformity and chemical composition distribution of the low-temperature ETMs could be systematically evaluated, and the spatial structural defects or dust/particles as recombination centers can be overall identified.

7. Service behavior of Low-Temperature ETMs

It is universally acknowledged that the ETMs play important roles to the performance of PSCs due to the particular responsibility for charge

Table 5

Non-exhaustive summary of reported perovskite solar modules.

ETM	Device architecture	Interconnection	Cell Efficiency	Module Active Area Efficiency	ModuleArea (cm ²)	Deposition methods	Temperature (°C)	Ref.
SnO ₂	Glass/FTO/SnO ₂ /PCBM/MAPbI ₃ /Spiro-OMeTAD/Au	laser P1, manual P2, mask P3	20.28	18.13	21	spin-coating	180	[199]
	Glass/ITO/SnO ₂ /Cs _{0.05} FA _{0.54} MA _{0.41} Pb(I _{0.98} Br _{0.02}) ₃ /Spiro-OMeTAD + P3HT/Au	laser P1, laser P2, mechanical P3	21.8	16.6	22.4	spin-coating	150	[205]
	Glass/FTO/SnO ₂ @TiO ₂ /FAPbI ₃ -MAPbI ₃ /Spiro-OMeTAD/Au	laser P1, manual P2, mask P3	20.40	16.81	10.56	CBD	140	[206]
	Glass/FTO/SnO _x /Cs _{0.05} (FA _{0.85} MA _{0.15}) _{0.95} Pb(I _{0.85} Br _{0.15}) ₃ /Spiro-OMeTAD/Au	laser P1, P2, P3	19.17	16.16	16.07	blade coating	–	[207]
	Glass/FTO/SnO ₂ /FA _{0.85} MA _{0.15} Pb(I _{0.85} Br _{0.15}) ₃ + KI/Spiro-OMeTAD/Au	–	18.20	14.71	16.07	sputtering	–	[208]
	Glass/FTO/SnO _x [(CsPbI ₃) _{0.05} (FAPbI ₃) _{0.85} (MAPbBr ₃) _{0.15}) _{0.95} /Spiro-OMeTAD/Au	–	19.40	15.30	100	spin-coating	150	[209]
	Glass/FTO/SnO _x /MAPbI ₃ /Spiro-OMeTAD/Au	laser P1, P2, P3	17.3	13.1	13.8	spin-coating	180	[210]
	PET/ITO/SnO ₂ /MAPbI ₃ /Spiro-OMeTAD/Au	–	16.50	12.40	10	spin-coating	120	[211]
	FTO/SnO ₂ /Cs _x FA _{1-x} PbI _{3-y} Br _y /Spiro-MeOTAD/Au	–	17.29	12.24	41.25	Soaking	70	[212]
	Glass/FTO/SnO _x /MAPbI ₃ /Spiro-OMeTAD/Au	laser P1, laser P2, mechanical P3	17.8	12.03	22.8	sputtering	room temperature	[213]
	FTO/SnO ₂ /C ₆₀ /Cs _{0.1} FA _{0.9} PbI ₃ /Spiro-MeOTAD/Au	laser P1, laser P2, mechanical P3	13.30	10.37	91.8	sputtering	–	[214]
	Glass/FTO/SnO _x /MAPbI ₃ /Spiro-OMeTAD/Au	laser P1, P2, P3	16.7	9.37	15	spray coating	120	[215]
	PET/ITO/SnO ₂ /meso-TiO ₂ /MAPbI ₃ /Spiro-OMeTAD/Au	laser P1, P2, P3	14.8	8.8	12	spin-coating	150	[204]
	FTO/SnO ₂ /(FAPbI ₃) _{0.875} (CsPbBr ₃) _{0.125} /Spiro-OMeTAD/Au	laser P1, P2, P3	19.58	17.01	18.66	spin-coating	185	[216]
	FTO/SnO ₂ /K _{0.03} Cs _{0.05} (FA _{0.85} MA _{0.15}) _{0.92} Pb(I _{0.85} Br _{0.15}) ₃ /Spiro-OMeTAD/Au	laser P1, P2, mask P3	–	17.82	53.64	CBD	180	[217]
	PET/ITO/SnO ₂ /Cs _{0.05} (FA _{0.85} MA _{0.15}) _{0.95} Pb(I _{0.85} Br _{0.15}) ₃ /Spiro-OMeTAD/Au	laser P1, P2, P3	20.50	15.22	16.07	slot-die	140	[60]
TiO ₂	Glass/ITO/TiO ₂ /MAPbI ₃ /Spiro-MeOTAD/MoO ₃ /Ag	–	17.43	14.19	25.2	spin-coating	100	[218]
	Glass/FTO/TiO ₂ /MAPbI ₃ /Spiro-OMeTAD/Au	laser P1, P2, P3	17.09	14.01	16	soft-cover-assisted hydrolysis method	75	[219]
	Glass/FTO/TiO ₂ /MAPbI ₃ /Carbon + CuPc	laser P1, laser P2, mechanical P3	14.80	7.20	22.4	Sputtering	–	[203]
	PET/ITO/c-TiO ₂ /m-TiO ₂ /MAPbI ₃ /Spiro-OMeTAD/Au	etch P1, manual P2, mask P3	8.40	3.10	7.9	ALD	150	[220]
	Glass/FTO/TiO ₂ /FAPb(I _{0.85} Br _{0.15}) ₃ /Spiro-OMeTAD/Au	–	–	14.7	12	Sputtering	–	[221]
ZnO	Glass/ITO/c-TiO ₂ /CH ₃ NH ₃ PbI _{3-x} Cl/Spiro-OMeTAD/Au	laser P1, P2, P3	16.8	11.1	151.88	E-beam	–	[222]
	ITO/ZnO/MAPbI ₃ /doped-P3HT/Ag	–	–	4.56	47.3	Spin	140	[223]
	ITO/ZnO/MAPbI ₃ /P3HT/Au	–	11.96	9.30	40	Slot-die	120	[201]

separation, electron transfer and hole blocking. Beyond that, the quality and stability of perovskite materials as well as the lifespans of photovoltaic devices strongly depend on the surface/interface situation. [26,224] As for low-temperature ETMs, the surface properties and crystal quality issues are even more obvious because of the low-temperature processes. [225] In view of this, we will comprehensively and thoroughly explore the degradation mechanisms proposed thus far and their implications for solar cells and modules, together with some corresponding solutions. Fig. 37 illustrates potential failure routes at perovskite/low-temperature ETMs interface. Upon illumination, the ions in perovskites may decompose, migrate, volatilize and escape from the inside. Unfortunately, the low-temperature ETMs with lots of defects would cause photocarrier recombination and even degrade perovskite at the interface.

Common inorganic ETMs usually suffer from the photostability issue, because of the photocatalysis effects. Under UV illumination, the widely used ETMs could form reactive superoxide and then trigger the reaction with perovskite materials, especially the TiO₂. Specifically, the TiO₂ surface have oxygen vacancies and Ti₃₊ sites (Ti³⁺-V_O) with unpaired outer electrons. Low-temperature TiO₂ may have more defects than high-temperature processed TiO₂. [226] These defects as an electron donor could interact with O₂ and then form the O₂[·]. When the PSCs is

working under UV light, the photogenerated holes and the electrons trapped at defects would recombine and release O₂, which bond breaking with perovskite and thereby induce defects and decomposition. More recently, the degradation mechanism of TiO₂-based PSC has been thoroughly analyzed. [227] As shown in Fig. 38 (a), the electrons in valance band transfer to the conduction band under UV illumination (step ①). Meanwhile the unpaired electrons at the Ti³⁺-V_O site are inclined to recombine the free holes leaving in the valance band (step ②). On the basis, the free electrons accumulate in the conduction band and the Ti⁴⁺-V_O defect states are formed. Then the Ti⁴⁺-V_O defect states capture the photoelectrons from perovskite layer (step ③), reverting Ti⁴⁺-V_O to Ti³⁺-V_O, as shown by green arrow in Fig. 38(b). At the same time, the accumulated free electrons induced extra recombination with perovskite layer (step ④, ⑤) and HTM layer (step ⑥). With the prolongation of UV irradiation time, the Ti⁴⁺-V_O defect states constantly increase, which lead to the continuous decay of device performance as described by stage I in Fig. 38(c). More than that, the UV-induced Ti⁴⁺-V_O states lead to rapid failure of perovskite. Specifically, the Ti⁴⁺-V_O states can convert back to Ti³⁺-V_O states by oxidizing the I[–], which result in the formation of I₂ or I₃. The dissociation of I[–] from Pb₂I₆²⁻ octahedral structure caused the release and migration of CH₃NH₃⁺. Subsequently, the free soft acid CH₃NH₃⁺ and free soft base I₃ neutralized

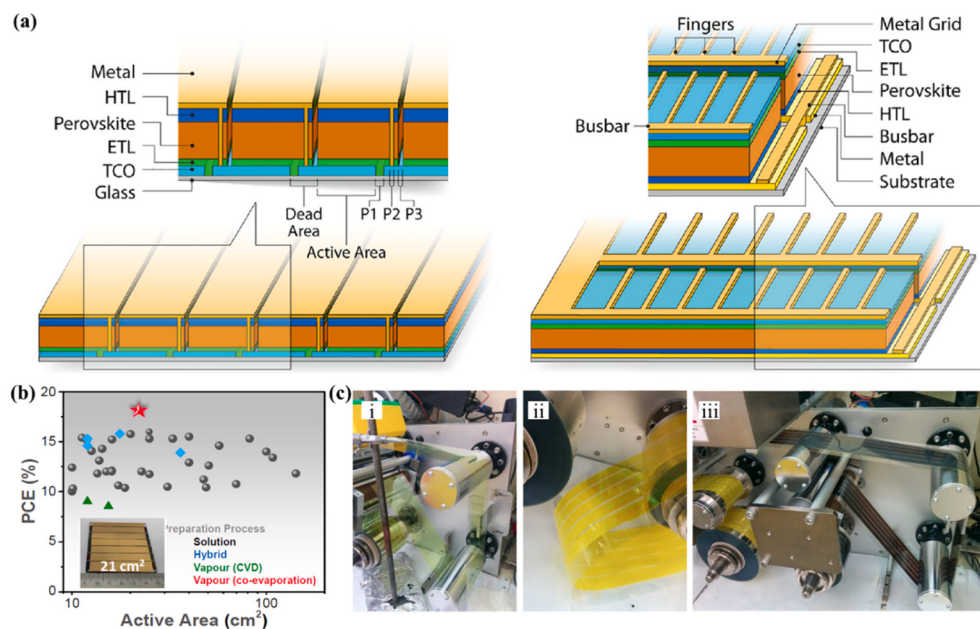


Fig. 36. (a) Schematic diagram of perovskite modules with P1,P2,P3 series connection.^[200] Copyright 2018, Elsevier. (b) Part of the reported PCEs of perovskite modules with an active area larger than 10 cm².^[199] Copyright 2020, Elsevier. (c) roll-to-roll production of perovskite module.^[201] Copyright 2015, Wiley-VCH.

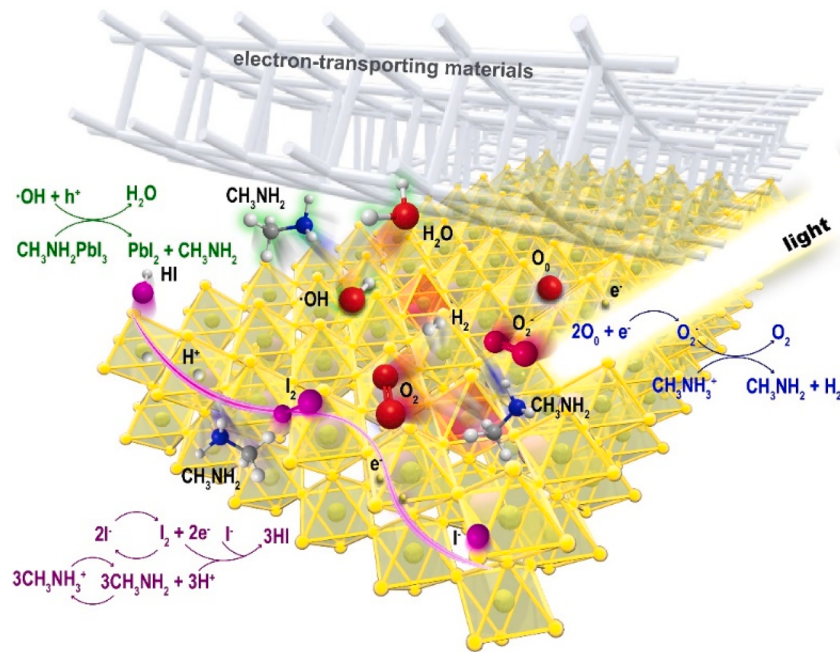


Fig. 37. Schematic illustration of the failure mechanism in perovskite on low-temperature ETMs surfaces.

spontaneously. The consumption of CH_3NH_3^+ and I^- lead to the degradation of perovskite and in turn result in the sharp decay of device performance as described by stage II in Fig. 38(c). Adversely, the UV light stability is more serious for low-temperature TiO_2 due to the increased defects induced by lower heat treatment temperatures.

Similarly, ZnO ETM also possesses photocatalytic activity.^[228] The photogenerated charges on ZnO surface would react with H_2O and O_2 and form hydroxyl radicals ($\cdot\text{OH}$) and O_2^- , thereby causing decomposition.^[229] Additionally, the TiO_2 would extract electrons from I^- in perovskite and then oxidize it into I_2 . Subsequently, the deprotonation of MA^+ results in the formation of CH_3NH_2 and H^+ . Finally, the electrons, I^- atoms and H^+ combine to HI . Moreover, the surface of ZnO ETM exhibits

alkaline property, which also induced deprotonation reaction, once ZnO contact with perovskite. Beyond that, the chemical residues such as hydroxyl species and residual acetate accelerate the decomposition of ETM and perovskite absorber.^[22] For example, the solution processed ZnO ETM at low temperature is not completely oxidized and covered oxygen groups on the surface.^[230] And then, the ionic interaction between MA^+ and PbI_3 is broke, which destroy the crystal structure of both perovskite and ZnO . More seriously, accompanied with increased temperature, the deterioration of ZnO as well as the decomposition of perovskite process would be dramatically exacerbated, which result in the poor stability.^[20] Meanwhile, even though SnO_2 is a chemically inert materials with negligible catalytic properties and insensitive to UV-

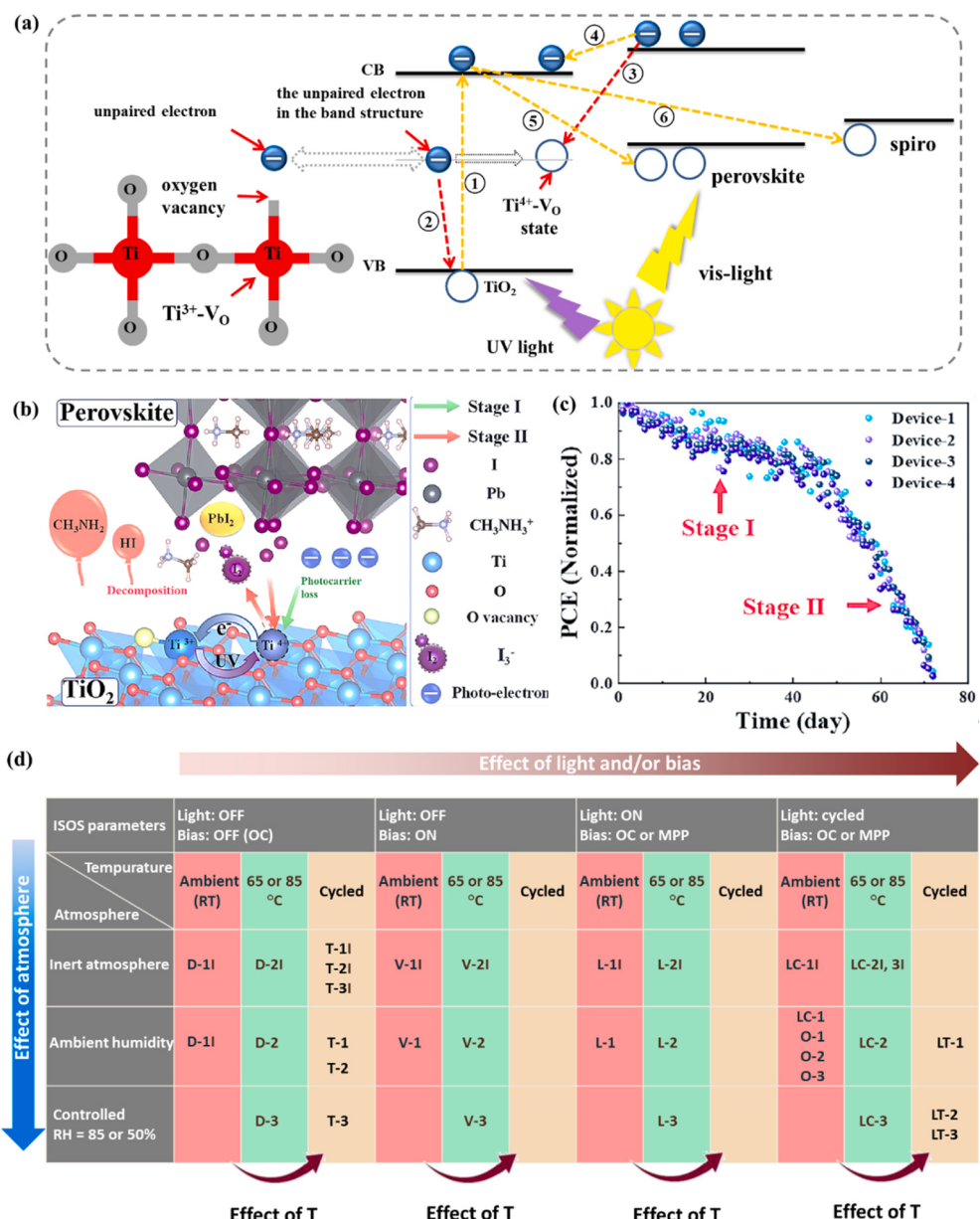


Fig. 38. (a) The carrier recombination channel and the generation process of $\text{Ti}^{4+}\text{-VO}$ under UV irradiation, (b) the mechanism of TiO_2 induced perovskite degradation, (c) the evolution of normalized PCE of PSCs under UV irradiation for 72 days, [227] Copyright 2020, Elsevier. (d) illustration of stress factors affecting the PSCs in different ISOS protocols. [231] Copyright 2020, Springer Nature.

light, the defect states, such as oxygen and tin vacancies, root in synthetic process induce severe device hysteresis and stability issues. In earlier work, the researchers proposed a standardized procedure for studying the stability of PSCs based on the ISOS protocol, as shown in Fig. 38(d). [231] As an important part of PSCs, the stability of the cryogenic electron transport layers needs to withstand multiple environmental factors.

Numerous targeted strategies, such as UV filter, surface/interface defects passivation, crystal quality modulation and synthesis routes design, have been proposed. Despite the recent progresses, degradation issue of the low-temperature ETMs as well as associated interfacial reactions are still the Achilles heel of PSCs, especially when scaled up to the module level.

8. Conclusion and Outlook

8.1. Conclusion

With unrivaled potential for excellent PCE and low manufacturing cost, PSCs have emerged as a disruptive class of photovoltaic technologies that have developed so rapidly that their commercialization is expected in a very near term. In this context, the low-temperature ETMs have shown to be promising due to the superiority in reduction of the manufacture cost, applicability in flexible devices and roll to roll processing, short preparation cycle, compatibility with other layers sensitive to temperatures, as well as feasibility in 2 T tandem devices. To summarize, the low-temperature ETMs have demonstrated flourishing progress owing to its alluring application scenario in photovoltaic products. In this review, we focus on the recent notable achievements in low-temperature ETMs for PSCs and modules, including extensive utilized TiO_2 , ZnO , SnO_2 as well as some alternatives. Their advancement,

key advantage, existing problems and various low-temperature processing technologies have been thoroughly introduced. Moreover, we emphatically elaborated the optimization strategies for champion perovskite devices with outstanding stability. Further, the development of low-temperature ETMs-based perovskite modules has been thoroughly reviewed. Next, we shed light on the service behavior of low-temperature ETMs from material fabrication to devices operation, mainly addressing the service mechanism. Finally, we complement this with an overview of the critical technical targets, the key technological obstacles to the ‘lab-to-fab’ transition and the potential opportunities arising from the use of low-temperature ETMs.

- (1) Regarding synthesis strategies, their merits and demerits have been reasonably discussed and compared (Fig. 13) to figure out the correlation between synthesis conditions and the characteristics of low-temperature ETMs. Currently, the spin coating method is commonly employed for the fabrication of low-temperature ETMs in high-efficiency PSCs, albeit with limited working area. The solution chemistry and processing conditions developed for spin coating cannot be easily extrapolated in other scalable deposition methods. Accurate synthesis strategies for low-temperature emerging thin films, comparable to those deposited at high temperatures, are still pending. Advancing our understanding of the factors that impact thin-film formation and enhancing our control of thin-film formation in different deposition processes are crucial for scaling up PSCs. Lastly, it is emphasized that the development of low temperature ETMs should prioritize high-quality film formation, cost-effectiveness, ease of operation, and scalability.
- (2) Serial advanced optimization strategies have been summarized, highlighting their features and limitations for low-temperature ETM modification (Fig. 25). Element doping and surface modification are considered as powerful regulation strategies of electron control and interfacial chemical compatibility modulation. And they exhibit the potential to seamlessly integrate into existing large-area preparation processes. Even though the significant advancements, the combination property of most low-temperature ETMs still fall behind their high-temperature counterparts. The joint application of various optimization strategies possesses tremendous effectiveness for the construction of high-quality low-temperature ETMs. By delving deeper into the micro-control mechanism behind various regulatory means applicable to low-temperature ETMs, new possibilities for designing exceptional ETMs at low temperatures can be unlocked.
- (3) Target at the mechanical reliability, a comprehensive analysis is conducted on the underlying causes, challenges, and current development status (Fig. 32). In order to pursue high stability, the mechanical properties of low temperature ETMs and the mechanical tolerance of the adjacent layer interface should be carefully considered. Interface modification provides a viable approach to enhance mechanical tolerance. Actually, organic molecules, due to their versatile functional groups, exhibit excellent flexibility, making them ideal candidates. Consequently, this leads to diverse mechanical properties that enable the absorption and release of compressive and tensile stresses at the interface. While, molecular rotational and/or bending flexibilities to accommodate complicated stress is desired to resist external forces. For that, the anchoring groups on molecules may require a chemical modification and functionalized design. In all, exploring new interfacial modifier to adjust/compromise the strain at interface without introducing phase and structural heterogeneity even on nanoscale, is rather urgent. And the mechanical modification of low-temperature ETMs without compromising its electrical properties is also of great importance, albeit challenging.

(4) Regarding the progress of low-temperature ETMs from laboratory-scale to industrial modules, the strategic importance of developing large-area low-temperature ETMs for perovskite modules has been emphasized. Recent progress in minimizing the efficiency gap have been summarized, highlighting the development tendency for moving PSCs technology toward industrial scale. The current large-area low-temperature ETMs fall short of the industry’s stringent requirements for efficiency and stability. Although laboratory-scale modules are processing rapidly, the compatibility issue with large-scale industrial production lines remains a significant concern, resulting in a substantial disparity between mature commercial-scale modules. In general, from lab-scale research to the potential commercialization, the trend of low-temperature ETMs is finally moving towards diversified large-scale preparation technology with high-quality deposition, environmentally friendly materials and processes, as well as large-scale and high-precision material property assessment.

8.2. Outlook

Despite impressive progress, there are still many key materials and processing challenges holding the crux for future development of low-temperature ETMs-based PSCs and modules:

- (1) *Machine learning accelerates process optimization and standardization.* Despite impressive progress, the uniformly low-temperature deposition technologies are still in the early stages. Specifically, key processing challenges include the fully scalable fabrication and reliable schemes for module interconnection. The challenges are further complicated because the most ideal ETM has not yet been identified and several manufacture-materials combinations have shown outstanding performance at cell level. In addition, transferring the highly crystalline low-temperature ETMs to production scale requires more effort in process engineering because of changes in the material processing conditions. Machine learning enables faster optimization compared with researcher driven design-of-experiment methods, which could help stabilize and rapidly update baseline manufacturing processes. Not only that, the machine learning assisted process could narrow the performance gap between large and small-size devices, thereby accelerating the standardization. Benefiting from blend machine algorithms and human expertise, the mature low-temperature processing technology line is promising to be put into routine use for laboratory-scale devices to industry-scale deployment.
- (2) *Novel and complementary modification routes.* In spite of some great progress, the performance of PSCs based on low-temperature ETMs is often considered inferior to that of conventional high-temperature processed ETMs. Low-temperature treatment have a great influence on the properties such as mobility, surface defects, and energy band alignment, which consequently induces a series of electrical and stability problems, especially at module-level. The fundamental understanding of the charge transfer behavior in low temperature ETMs -particularly on the nano- to microscale - is essential to control charge carriers and push devices to their performance limits. Therefore, novel interface modification strategy and structure design scheme should be sanely proposed and exclusively investigated. Specifically, rational surface modification by blending the ideal ETM with functional organic molecules could regulate the interface chemical environment. Reasonable microstructure design of low-temperature ETMs may be conducive to juggle the favorable contact between ETM and perovskite. Artful multi-layer stacking of low-temperature ETMs could achieve mutual complementarity by fulfilling each other’s imperfection.

- (3) *Techniques suitable for characterizing and guiding the development of low-temperature ETMs.* In transitioning from lab-scale to module-level development, it is particularly vital and complex to assess and control the uniformity of material properties, the distribution of defects, the locations of short circuits and shunts, as well as interconnect properties in modules. In this regard, joint utilization of spectroscopic and image mapping techniques is critical to present the full landscape of low-temperature ETMs for large-area device and/or module development. Specifically, the electroluminescence image could carry the charge recombination information at nanoscale and macroscopic charge transport obstacles unite with impurities, non-uniformity. While the complementary of electroluminescence and photoluminescence could effectively reveal macroscopic defects by weaker electroluminescence and stronger photoluminescence features in the image.
- (4) *Amplification degradation investigation at module level.* Major degradation factors of low-temperature ETMs in PSCs have been systematically discussed, but the service behavior at module level is more miscellaneous than at the small-cell level. Not only the potential of large-scale low-temperature deposition processed-induced degradation routes, certain service behaviors are unique to more complex models, such as the degradation of ETMs caused by partial shading/uneven lighting. In addition, the interconnection regions have high reverse bias and cause local temperature difference. These effects might accelerate the intrinsic and extrinsic failure factors to change the service performance of transporting layers over time. Thus, the amplification degradation analysis for low-temperature ETMs is necessary in realistic module configurations.
- (5) *Intellectually trade-off for performance-cost-stability-environment relation.* As perovskite technology matures, the low-cost production and sustainability of photovoltaic systems at scale should be considered. ETMs are one of the largest contributors to primary energy consumption and environmental impact. Importantly, many of the low-temperature ETMs discussed in this paper have one or more property/stability-related issues, which convinces us to push novel processing and modification techniques of these materials as mentioned above. The still immature manufacturing processes, mutative operating conditions and individual differences for each material induce lots of uncertainty for environment. These procedures for improved stability and PCE must be carried out on the premise of economic and environmental life cycle assessments studies to boost eco-efficiency.

In short, founded on material physics and chemistry, and referring to integrated manufacturing technology, the development of low-temperature ETMs will be constantly promoted, which is expected to achieve both cost-effective, stable and scalable all-cryogenic perovskite devices and modules, and meet the needs of flexible and 2 T series devices and other applications.

Declaration of Competing Interest

The authors declare that they have no known competing financial interests or personal relationships that could have appeared to influence the work reported in this paper.

Data availability

No data was used for the research described in the article.

Acknowledgements

This work was supported by the National Key Research and Development Program of China (No. 2018YFA0703500), the National Natural Science Foundation of China (Nos. 52232006, 52188101, 52102153,

52072029, 51991340, and 51991342), the Overseas Expertise Introduction Projects for Discipline Innovation (B14003), the Fundamental Research Funds for the Central Universities (FRF-TP-18-001C1 and 06500160), and Interdisciplinary Research Project for Young Teachers of USTB (Fundamental Research Funds for the Central Universities) (Nos. FRF-IDRY-21-019 and FRF-IDRY-21-014), and the State Key Lab for Advanced Metals and Materials (2023-Z01).

References

- [1] M.A. Green, A. Ho-Baillie, H.J. Snaith, *Nat. Photonics* 8 (2014) 506–514.
- [2] NREL Best research-cell efficiencies chart, <https://www.nrel.gov/pv/assets/pdfs/best-research-cell-efficiencies.pdf>.
- [3] N. Li, X. Niu, Q. Chen, H. Zhou, *Chem. Soc. Rev.* 49 (2020) 8235–8286.
- [4] H.S. Jung, G.S. Han, N.-G. Park, M.J. Ko, *Joule* 3 (2019) 1850–1880.
- [5] S. Chen, X. Xiao, H. Gu, J. Huang, *Sic. Adv.*, 7 (2021) eabe8130.
- [6] H. Si, Z. Zhang, Q. Liao, G. Zhang, Y. Ou, S. Zhang, H. Wu, J. Wu, Z. Kang, Y. Zhang, *Adv. Mater.* 32 (2019) 1904702.
- [7] M.H. Kumar, N. Yantara, S. Dharani, M. Graetzel, S. Mhaisalkar, P.P. Boix, N. Mathews, *Chem. Commun.* 49 (2013) 11089–11091.
- [8] B.J. Kim, D.H. Kim, Y.-Y. Lee, H.-W. Shin, G.S. Han, J.S. Hong, K. Mahmood, T. K. Ahn, Y.-C. Joo, K.S. Hong, N.-G. Park, S. Lee, H.S. Jung, *Energ. Environ. Sci.* 8 (2015) 916–921.
- [9] S.S. Shin, W.S. Yang, J.H. Noh, J.H. Suk, N.J. Jeon, J.H. Park, J.S. Kim, W. M. Seong, S.I. Seok, *Nat. Commun.* 6 (2015) 7410.
- [10] Y. Gao, K. Huang, C. Long, Y. Ding, J. Chang, D. Zhang, L. Etgar, M. Liu, J. Zhang, J. Yang, *ACS Energy Lett.* 7 (2022) 1412–1445.
- [11] G. Tang, F. Yan, *Nano Today* 39 (2021), 101155.
- [12] X. Wu, G. Xu, F. Yang, W. Chen, H. Yang, Y. Shen, Y. Wu, H. Chen, J. Xi, X. Tang, Q. Cheng, Y. Chen, X.-M. Ou, Y. Li, Y. Li, *ACS Energy Lett.* (2023) 3750–3759.
- [13] A. Al-Ashouri, E. Köhnen, B. Li, A. Magomedov, H. Hempel, P. Caprioglio, J. A. Márquez, A.B.M. Vilches, E. Kasparavicius, J.A. Smith, N. Phung, D. Menzel, M. Grischek, L. Kegelmann, D. Skroblin, C. Göllwitzer, T. Malinauskas, M. Jost, G. Matić, B. Rech, R. Schlatmann, M. Topić, L. Korte, A. Abate, B. Stannowski, D. Neher, M. Stolterfoht, T. Unold, V. Getautis, S. Albrecht, *Science* 370 (2020) 1300–1309.
- [14] S. Mariotti, E. Köhnen, F. Scheler, K. Sveinbjörnsson, L. Zimmermann, M. Piot, F. Yang, B. Li, J. Warby, A. Muñizienko, D. Menzel, F. Lang, S. Keßler, I. Levine, D. Mantione, A. Al-Ashouri, M.S. Härtel, K. Xu, A. Cruz, J. Kurpiers, P. Wagner, H. Köbler, J. Li, A. Magomedov, D. Mecerreyes, E. Unger, A. Abate, M. Stolterfoht, B. Stannowski, R. Schlatmann, L. Korte, S. Albrecht, *Science* 381 (2023) 63–69.
- [15] S.S. Shin, S.J. Lee, S.I. Seok, *Adv. Funct. Mater.* 29 (2019) 1900455.
- [16] Y. Zhou, X. Li, H. Lin, *Small* 16 (2020) 1902579.
- [17] C. Altinkaya, E. Aydin, E. Ugur, F.H. Isikgor, A.S. Subbiah, M. De Bastiani, J. Liu, A. Babayigit, T.G. Allen, F. Laquai, A. Yıldız, S. De Wolf, *Adv. Mater.* 33 (2021) 2005504.
- [18] J. Lian, B. Lu, F. Niu, P. Zeng, X. Zhan, *Small Methods* 2 (2018) 1800082.
- [19] S. Zhang, H. Si, W. Fan, M. Shi, M. Li, C. Xu, Z. Zhang, Q. Liao, A. Sattar, Z. Kang, Y. Zhang, *Angew. Chem. Int. Ed.* 59 (2020) 11573–11582.
- [20] H. Si, Q. Liao, Z. Zhang, Y. Li, X. Yang, G. Zhang, Z. Kang, Y. Zhang, *Nano Energy* 22 (2016) 223–231.
- [21] D. Reyes-Coronado, G. Rodríguez-Gattorno, M.E. Espinosa-Pesqueira, C. Cab, R. de Coss, G. Oskam, *Nanotechnology* 19 (2008), 145605.
- [22] H. Si, Z. Zhang, Q. Liao, Z. Kang, Y. Zhang, *Kexue Tongbao/Chin. Sci. Bull.* 65 (2020) 2721–2739.
- [23] S. Bai, Y. Jin, X. Liang, Z. Ye, Z. Wu, B. Sun, Z. Ma, Z. Tang, J. Wang, U. Würfel, F. Gao, F. Zhang, *Adv. Energy Mater.* 5 (2015) 1401606.
- [24] D. Liu, T.L. Kelly, *Nat. Photonics* 8 (2014) 133–138.
- [25] L. Xiong, M. Qin, C. Chen, J. Wen, G. Yang, Y. Guo, J. Ma, Q. Zhang, P. Qin, S. Li, G. Fang, *Adv. Funct. Mater.* 28 (2018) 1706276.
- [26] J. Wei, Q. Wang, J. Huo, F. Gao, Z. Gan, Q. Zhao, H. Li, *Adv. Energy Mater.* (2020) 2002326.
- [27] L. Xiong, J. Li, F. Ye, H. Wang, Y. Guo, X. Ming, Q. Chen, S. Zhang, R. Xie, Z. Chen, Y. Lv, G. Hu, Y. He, G. Fang, *Adv. Funct. Mater.* 31 (2021) 2103949.
- [28] K. Wang, Y. Shi, Q. Dong, Y. Li, S. Wang, X. Yu, M. Wu, T. Ma, *J. Phys. Chem. Lett.* 6 (2015) 755–759.
- [29] R. Fang, S. Wu, W. Chen, Z. Liu, S. Zhang, R. Chen, Y. Yue, L. Deng, Y.-B. Cheng, L. Han, W. Chen, *ACS Nano* 12 (2018) 2403–2414.
- [30] X. Ling, J. Yuan, D. Liu, Y. Wang, Y. Zhang, S. Chen, H. Wu, F. Jin, F. Wu, G. Shi, X. Tang, J. Zheng, S. Liu, Z. Liu, W. Ma, *ACS Appl. Mater. Interfaces* 9 (2017) 23181–23188.
- [31] C. Chen, Y. Jiang, Y. Wu, J. Guo, X. Kong, X. Wu, Y. Li, D. Zheng, S. Wu, X. Gao, Z. Hou, G. Zhou, Y. Chen, J.-M. Liu, K. Kempa, J. Gao, *Solar RRL* 4 (2020) 1900499.
- [32] X. Wang, L.-L. Deng, L.-Y. Wang, S.-M. Dai, Z. Xing, X.-X. Zhan, X.-Z. Lu, S.-Y. Xie, R.-B. Huang, L.-S. Zheng, *J. Mater. Chem. A* 5 (2017) 1706–1712.
- [33] J. Feng, Z. Yang, D. Yang, X. Ren, X. Zhu, Z. Jin, W. Zi, Q. Wei, S. Liu, *Nano Energy* 36 (2017) 1–8.
- [34] D. Han, Y. Xin, Q. Yuan, Q. Yang, Y. Wang, Y. Yang, S. Yi, D. Zhou, L. Feng, Y. Wang, *Solar RRL* 3 (2019) 1900091.
- [35] F. Sadegh, S. Akin, M. Moghadam, V. Mirkhani, M.A. Ruiz-Preciado, Z. Wang, M. Tavakoli, M. Graetzel, A. Hagfeldt, W. Tress, *Nano Energy* 75 (2020), 105038.

- [36] Z. Galazka, R. Uecker, K. Irmscher, D. Klimm, R. Bertram, A. Kwasniewski, M. Naumann, R. Schewski, M. Pietsch, U. Juda, A. Fiedler, M. Albrecht, S. Ganschow, T. Markurt, C. Guguschev, M. Bickermann, *J. Phys. Condens. Matter* 29 (2016) 075701.
- [37] S. Bhandari, A. Roy, T.K. Mallick, S. Sundaram, *Chem. Eng. J.* 446 (2022), 137378.
- [38] F. Wang, Y. Cao, C. Chen, Q. Chen, X. Wu, X. Li, T. Qin, W. Huang, *Adv. Funct. Mater.* 28 (2018) 1803753.
- [39] A.A. Said, J. Xie, Q. Zhang, *Small* 15 (2019) 1900854.
- [40] J.-Y. Shao, D. Li, J. Shi, C. Ma, Y. Wang, X. Liu, X. Jiang, M. Hao, L. Zhang, C. Liu, Y. Jiang, Z. Wang, Y.-W. Zhong, S.F. Liu, Y. Mai, Y. Liu, Y. Zhao, Z. Ning, L. Wang, B. Xu, L. Meng, Z. Bian, Z. Ge, X. Zhan, J. You, Y. Li, Q. Meng, *Sci. China Chem.* 66 (2023) 10–64.
- [41] Y. Jiang, J. Wang, H. Zai, D. Ni, J. Wang, P. Xue, N. Li, B. Jia, H. Lu, Y. Zhang, F. Wang, Z. Guo, Z. Bi, H. Xie, Q. Wang, W. Ma, Y. Tu, H. Zhou, X. Zhan, *J. Am. Chem. Soc.* 144 (2022) 5400–5410.
- [42] Q. Tan, Z. Li, G. Luo, X. Zhang, B. Che, G. Chen, H. Gao, D. He, G. Ma, J. Wang, J. Xiu, H. Yi, T. Chen, Z. He, *Nature* (2023).
- [43] C. Sun, Z. Wu, H.-L. Yip, H. Zhang, X.-F. Jiang, Q. Xue, Z. Hu, Z. Hu, Y. Shen, M. Wang, F. Huang, Y. Cao, *Adv. Energy Mater.* 6 (2016) 1501534.
- [44] S.-K. Jung, J.H. Heo, D.W. Lee, S.-C. Lee, S.-H. Lee, W. Yoon, H. Yun, S.H. Im, J. H. Kim, O.-P. Kwon, *Adv. Funct. Mater.* 28 (2018) 1800346.
- [45] S. Zheng, G. Wang, T. Liu, L. Lou, S. Xiao, S. Yang, *Sci. China Chem.* 62 (2019) 800–809.
- [46] X. Luo, Z. Shen, Y. Shen, Z. Su, X. Gao, Y. Wang, Q. Han, L. Han, *Adv. Mater.* 34 (2022) 2202100.
- [47] K. Wojciechowski, M. Saliba, T. Leijtens, A. Abate, H.J. Snaith, *Energ. Environ. Sci.* 7 (2014) 1142–1147.
- [48] J.M. Szeifert, D. Fattakhova-Rohlfing, D. Georgiadou, V. Kalousek, J. Rathouský, D. Kuang, S. Wenger, S.M. Zakeeruddin, M. Grätzel, T. Bein, *Chem. Mater.* 21 (2009) 1260–1265.
- [49] E.J.W. Crossland, N. Noel, V. Sivaram, T. Leijtens, J.A. Alexander-Webber, H. J. Snaith, *Nature* 495 (2013) 215–219.
- [50] A. Kogo, M. Ikegami, T. Miyasaka, *Chem. Commun.* 52 (2016) 8119–8122.
- [51] S.-Y. Lin, T.-S. Su, T.-Y. Hsieh, P.-C. Lo, T.-C. Wei, *Adv. Energy Mater.* 7 (2017) 1700169.
- [52] J. Huang, Z. Gu, L. Zuo, H. Chen, *Sol. Energy* 133 (2016) 331–338.
- [53] L. Zuo, Z. Gu, T. Ye, W. Fu, G. Wu, H. Li, H. Chen, *J. Am. Chem. Soc.* 137 (2015) 2674–2679.
- [54] Y.-H. Zhao, K.-C. Zhang, Z.-W. Wang, P. Huang, K. Zhu, Z.-D. Li, D.-H. Li, L.-G. Yuan, Y. Zhou, B. Song, *ACS Appl. Mater. Interfaces* 9 (2017) 26234–26241.
- [55] L. Zuo, H. Guo, D.W. deQuilettes, S. Jariwala, N. De Marco, S. Dong, R. DeBlock, D.S. Ginger, B. Dunn, M. Wang, Y. Yang, *Sic. Adv.*, 3 (2017) e1700106.
- [56] W. Ke, G. Fang, Q. Liu, L. Xiong, P. Qin, H. Tao, J. Wang, H. Lei, B. Li, J. Wan, G. Yang, Y. Yan, *J. Am. Chem. Soc.* 137 (2015) 6730–6733.
- [57] H. Yu, H.-I. Yeom, J.W. Lee, K. Lee, D. Hwang, J. Yun, J. Ryu, J. Lee, S. Bae, S. K. Kim, J. Jang, *Adv. Mater.* 30 (2018) 1704825.
- [58] G. Yang, C. Chen, F. Yao, Z. Chen, Q. Zhang, X. Zheng, J. Ma, H. Lei, P. Qin, L. Xiong, W. Ke, G. Li, Y. Yan, G. Fang, *Adv. Mater.* 30 (2018) 1706023.
- [59] Q. Jiang, L. Zhang, H. Wang, X. Yang, J. Meng, H. Liu, Z. Yin, J. Wu, X. Zhang, J. You, *Nat. Energy* 2 (2016) 16177.
- [60] T. Bu, J. Li, F. Zheng, W. Chen, X. Wen, Z. Ku, Y. Peng, J. Zhong, Y.-B. Cheng, F. Huang, *Nat. Commun.* 9 (2018) 4609.
- [61] R. Chen, J. Wang, Z. Liu, F. Ren, S. Liu, J. Zhou, H. Wang, X. Meng, Z. Zhang, X. Guan, W. Liang, P.A. Troshin, Y. Qi, L. Han, W. Chen, *Nat. Energy* (2023).
- [62] R. Viswanatha, H. Amenitsch, D.D. Sarma, *J. Am. Chem. Soc.* 129 (2007) 4470–4475.
- [63] D.-Y. Son, J.-H. Im, H.-S. Kim, N.-G. Park, *J. Phys. Chem. C* 118 (2014) 16567–16573.
- [64] H. Si, Z. Kang, Q. Liao, Z. Zhang, X. Zhang, L. Wang, Y. Zhang, *Science China-Materials* 60 (2017) 793–810.
- [65] A. Yella, L.-P. Heiniger, P. Gao, M.K. Nazeeruddin, M. Grätzel, *Nano Lett.* 14 (2014) 2591–2596.
- [66] E.H. Anaraki, A. Kermanpur, L. Steier, K. Domanski, T. Matsui, W. Tress, M. Saliba, A. Abate, M. Grätzel, A. Hagfeldt, J.-P. Correa-Baena, *Energ. Environ. Sci.* 9 (2016) 3128–3134.
- [67] J.-Y. Chen, C.-C. Chueh, Z. Zhu, W.-C. Chen, A.K.Y. Jen, *Sol. Energy Mater. Sol. Cells* 164 (2017) 47–55.
- [68] P. Zhang, J. Wu, T. Zhang, Y. Wang, D. Liu, H. Chen, L. Ji, C. Liu, W. Ahmad, Z. D. Chen, *Adv. Mater.* 30 (2018) 1703737.
- [69] K.-M. Lee, S.H. Chang, K.-H. Wang, C.-M. Chang, H.-M. Cheng, C.-C. Kei, Z.-L. Tseng, C.-G. Wu, *Sol. Energy* 120 (2015) 117–122.
- [70] K.O. Brinkmann, T. Gahlmann, T. Riedl, *Solar Rrl* 4 (2020).
- [71] A. Illiberi, F. Roozeboom, P. Poodt, *ACS Appl. Mater. Interfaces* 4 (2012) 268–272.
- [72] C. Wang, D. Zhao, C.R. Grice, W. Liao, Y. Yu, A. Cimaroli, N. Shrestha, P. J. Roland, J. Chen, Z. Yu, P. Liu, N. Cheng, R.J. Ellingson, X. Zhao, Y. Yan, *J. Mater. Chem. A* 4 (2016) 12080–12087.
- [73] C. Wang, C. Xiao, Y. Yu, D. Zhao, R.A. Awni, C.R. Grice, K. Ghimire, I. Constantinou, W. Liao, A.J. Cimaroli, P. Liu, J. Chen, N.J. Podraza, C.-S. Jiang, M.M. Al-Jassim, X. Zhao, Y. Yan, *Adv. Energy Mater.* 7 (2017) 1700414.
- [74] Y. Lee, S. Lee, G. Seo, S. Paek, K.T. Cho, A.J. Huckaba, M. Calizzi, D.-W. Choi, J.-S. Park, D. Lee, H.J. Lee, A.M. Asiri, M.K. Nazeeruddin, *Adv. Sci.* 5 (2018) 1800130.
- [75] A.K. Chandiran, A. Yella, M.T. Mayer, P. Gao, M.K. Nazeeruddin, M. Grätzel, *Adv. Mater.* 26 (2014) 4309–4312.
- [76] D. Yang, R. Yang, J. Zhang, Z. Yang, S. Liu, C. Li, *Energ. Environ. Sci.* 8 (2015) 3208–3214.
- [77] C. Chen, Y. Cheng, Q. Dai, H. Song, *Sci. Rep.* 5 (2016) 17684.
- [78] H. Si, S. Zhang, S. Ma, Z. Xiong, A. Kausar, Q. Liao, Z. Zhang, A. Sattar, Z. Kang, Y. Zhang, *Adv. Energy Mater.* 10 (2020) 1903922.
- [79] Z. Chen, G. Yang, X. Zheng, H. Lei, C. Chen, J. Ma, H. Wang, G. Fang, *J. Power Sources* 351 (2017) 123–129.
- [80] H. Li, M. Liu, M. Li, H. Park, N. Mathews, Y. Qi, X. Zhang, H.J. Bolink, K. Leo, M. Graetzel, C. Yi, *iEnergy*, 1 (2022) 434–452.
- [81] C. Momblonia, L. Gil-Escrí, E. Bandiello, E.M. Hutter, M. Sessolo, K. Lederer, J. Blochwitz-Nimoth, H.J. Bolink, *Energ. Environ. Sci.* 9 (2016) 3456–3463.
- [82] D. Pérez-del-Rey, P.P. Boix, M. Sessolo, A. Hadipour, H.J. Bolink, *J. Phys. Chem. Lett.* 9 (2018) 1041–1046.
- [83] X. Zheng, Z. Li, Y. Zhang, M. Chen, T. Liu, C. Xiao, D. Gao, J.B. Patel, D. Kuciauskas, A. Magomedov, R.A. Scheidt, X. Wang, S.P. Harvey, Z. Dai, C. Zhang, D. Morales, H. Pruett, B.M. Wieliczka, A.R. Kirmani, N.P. Padture, K. R. Graham, Y. Yan, M.K. Nazeeruddin, M.D. McGehee, Z. Zhu, J.M. Luther, *Nat. Energy* 8 (2023) 462–472.
- [84] F. Li, X. Deng, Z. Shi, S. Wu, Z. Zeng, D. Wang, Y. Li, F. Qi, Z. Zhang, Z. Yang, S.-H. Jiang, F.R. Lin, S.W. Tsang, X.-K. Chen, A.K.Y. Jen, *Nat. Photonics* 17 (2023) 478–484.
- [85] J. Ma, X. Zheng, H. Lei, W. Ke, C. Chen, Z. Chen, G. Yang, G. Fang, *Solar RRL* 1 (2017) 1700118.
- [86] J. Nam, J.H. Kim, C.S. Kim, J.-D. Kwon, S. Jo, *ACS Appl. Mater. Interfaces* 12 (2020) 12648–12655.
- [87] H. Zhou, Q. Chen, G. Li, S. Luo, T.-B. Song, H.-S. Duan, Z. Hong, J. You, Y. Liu, Y. Yang, *Science* 345 (2014) 542–546.
- [88] H. Tan, A. Jain, O. Voznyy, X. Lan, F.P. García de Arquer, J.Z. Fan, R. Quintero-Bermudez, M. Yuan, B. Zhang, Y. Zhao, *Science* 355 (2017) 722–726.
- [89] A. Huang, L. Lei, J. Zhu, Y. Yu, Y. Liu, S. Yang, S. Bao, X. Cao, P. Jin, *ACS Appl. Mater. Interfaces* 9 (2017) 2016–2022.
- [90] J. You, L. Meng, T.-B. Song, T.-F. Guo, Y. Yang, W.-H. Chang, Z. Hong, H. Chen, H. Zhou, Q. Chen, Y. Liu, N. De Marco, Y. Yang, *Nat. Nanotechnol.* 11 (2016) 75–81.
- [91] J.H. Heo, M.H. Lee, H.J. Han, B.R. Patil, J.S. Yu, S.H. Im, J. Mater. Chem. A 4 (2016) 1572–1578.
- [92] X. Dong, H. Hu, B. Lin, J. Ding, N. Yuan, *Chem. Commun.* 50 (2014) 14405–14408.
- [93] C.-Y. Chang, K.-T. Lee, W.-K. Huang, H.-Y. Siao, Y.-C. Chang, *Chem. Mater.* 27 (2015) 5122–5130.
- [94] K. Mahmood, B.S. Swain, A. Amassian, *Nanoscale* 6 (2014) 14674–14678.
- [95] K. Mahmood, B.S. Swain, A. Amassian, *Adv. Energy Mater.* 5 (2015) 1500568.
- [96] J. Dong, J. Shi, D. Li, Y. Luo, Q. Meng, *Appl. Phys. Lett.* 107 (2015), 073507.
- [97] S. Li, P. Zhang, H. Chen, Y. Wang, D. Liu, J. Wu, H. Sarvari, Z.D. Chen, *J. Power Sources* 342 (2017) 990–997.
- [98] J. Zhang, E.J. Juárez-Pérez, I. Mora-Seró, B. Viana, T. Pauporté, *J. Mater. Chem. A* 3 (2015) 4909–4915.
- [99] Z.-L. Tseng, C.-H. Chiang, C.-G. Wu, *Sci. Rep.* 5 (2015) 13211.
- [100] J.P. Correa Baena, L. Steier, W. Tress, M. Saliba, S. Neutzner, T. Matsui, F. Giordano, T.J. Jacobsson, A.R. Srimath Kandada, S.M. Zakeeruddin, A. Petrozza, A. Abate, M.K. Nazeeruddin, M. Grätzel, A. Hagfeldt, *Energ. Environ. Sci.* 8 (2015) 2928–2934.
- [101] S. Jeong, S. Seo, H. Park, H. Shin, *Chem. Commun.* 55 (2019) 2433–2436.
- [102] J. Barbe, M.L. Tietze, M. Neophytou, B. Murali, E. Alarousu, A.E. Laban, M. Abulikemu, W. Yue, O.F. Mohammed, I. McCulloch, A. Amassian, S. Del Gobbo, *ACS Appl. Mater. Interfaces* 9 (2017) (1836) 11828–111821.
- [103] S.N. Habisreutinger, B. Wenger, H.J. Snaith, R.J. Nicholas, *ACS Energy Lett.* 2 (2017) 622–628.
- [104] A. Gheno, T.T. Thu Pham, C. Di Bin, J. Bouclé, B. Ratier, S. Vedraine, *Sol. Energy Mater. Sol. Cells* 161 (2017) 347–354.
- [105] T. Yokoyama, Y. Nishitani, Y. Miyamoto, S. Kusumoto, R. Uchida, T. Matsui, K. Kawano, T. Sekiguchi, Y. Kaneko, *ACS Appl. Mater. Interfaces* 12 (2020) 27131–27139.
- [106] X. Hu, C. Liu, Z. Zhang, X.-F. Jiang, J. Garcia, C. Sheehan, L. Shui, S. Priya, G. Zhou, S. Zhang, K. Wang, *Adv. Sci.* 7 (2020) 2001285.
- [107] X. Deng, F. Li, Q. Wang, D. Liu, F. Lin, D. Shen, D. Lei, Y.-K. Peng, Z. Zhu, A.K.Y. Jen, *Mater.* (2021).
- [108] H. Guo, H. Chen, H. Zhang, X. Huang, J. Yang, B. Wang, Y. Li, L. Wang, X. Niu, Z. Wang, *Nano Energy* 59 (2019) 1–9.
- [109] R. Azmi, S. Hwang, W. Yin, T.-W. Kim, T.K. Ahn, S.-Y. Jang, *ACS Energy Lett.* 3 (2018) 1241–1246.
- [110] E.H. Jung, B. Chen, K. Bertens, M. Vafaei, S. Teale, A. Proppe, Y. Hou, T. Zhu, C. Zheng, E.H. Sargent, *ACS Energy Lett.* 5 (2020) 2796–2801.
- [111] Z. Liu, K. Deng, J. Hu, L. Li, *Angew. Chem. Int. Ed. Engl.* 58 (2019) 11497–11504.
- [112] P. Zhu, S. Gu, X. Luo, Y. Gao, S. Li, J. Zhu, H. Tan, *Adv. Energy Mater.* 10 (2020) 1903083.
- [113] Y. Bai, Y. Fang, Y. Deng, Q. Wang, J. Zhao, X. Zheng, Y. Zhang, J. Huang, *ChemSusChem* 9 (2016) 2686–2691.
- [114] M. Park, J.-Y. Kim, H.J. Son, C.-H. Lee, S.S. Jang, M.J. Ko, *Nano Energy* 26 (2016) 208–215.
- [115] E. Wang, P. Chen, X. Yin, Y. Wu, W. Que, *Solar RRL* 3 (2019) 1900041.
- [116] J. Tian, J. Zhang, X. Li, B. Cheng, J. Yu, W. Ho, *Solar RRL* 4 (2020) 2000090.
- [117] Y.W. Noh, J.H. Lee, I.S. Jin, S.H. Park, J.W. Jung, *Nano Energy* 65 (2019), 104014.
- [118] Z. Song, W. Bi, X. Zhuang, Y. Wu, B. Zhang, X. Chen, C. Chen, Q. Dai, H. Song, *Solar RRL* 4 (2020) 1900266.

- [119] E. Halvani Anaraki, A. Kermanpur, M.T. Mayer, L. Steier, T. Ahmed, S.-H. Turren-Cruz, J. Seo, J. Luo, S.M. Zakeeruddin, W.R. Tress, T. Edvinsson, M. Grätzel, A. Hagfeldt, J.-P. Correa-Baena, *ACS Energy Lett.* 3 (2018) 773–778.
- [120] J. Song, W. Zhang, D. Wang, K. Deng, J. Wu, Z. Lan, *Sol. Energy* 185 (2019) 508–515.
- [121] S. Akin, *ACS Appl Mater Interfaces* 11 (2019) 39998–40005.
- [122] X. Gong, Q. Sun, S. Liu, P. Liao, Y. Shen, C. Grätzel, S.M. Zakeeruddin, M. Grätzel, M. Wang, *Nano Lett.* 18 (2018) 3969–3977.
- [123] W. Gong, H. Guo, H. Zhang, J. Yang, H. Chen, L. Wang, F. Hao, X. Niu, *J. Mater. Chem. C* 8 (2020) 11638–11646.
- [124] Y. Qiang, Y. Xie, Y. Qi, P. Wei, H. Shi, C. Geng, H. Liu, *Sol. Energy* 201 (2020) 523–529.
- [125] P. Sakthivel, S. Foo, M. Thambidurai, P.C. Harikesh, N. Mathews, R. Yuvakkumar, G. Ravi, C. Dang, *J. Power Sources* 471 (2020), 228443.
- [126] Q. Cao, Z. Li, J. Han, S. Wang, J. Zhu, H. Tang, X. Li, X. Li, *Solar RRL* 3 (2019) 1900333.
- [127] J. Bahadur, A.H. Ghahremani, B. Martin, T. Druffel, M.K. Sunkara, K. Pal, *Org. Electron.* 67 (2019) 159–167.
- [128] Z. Ma, W. Zhou, Z. Xiao, H. Zhang, Z. Li, J. Zhuang, C. Peng, Y. Huang, *Org. Electron.* 71 (2019) 98–105.
- [129] Q. Liu, X. Zhang, C. Li, H. Lu, Z. Weng, Y. Pan, W. Chen, X.-C. Hang, Z. Sun, Y. Zhan, *Appl. Phys. Lett.* 115 (2019), 143903.
- [130] Z. Xu, S.H. Teo, L. Gao, Z. Guo, Y. Kamata, S. Hayase, T. Ma, *Org. Electron.* 73 (2019) 62–68.
- [131] J. Jia, J. Dong, J. Wu, H. Wei, B. Cao, *J. Alloy. Compd.* 844 (2020), 156032.
- [132] S.S. Shin, J.H. Suk, B.J. Kang, W. Yin, S.J. Lee, J.H. Noh, T.K. Ahn, F. Rotermund, I.S. Cho, S.I. Seok, *Energ. Environ. Sci.* 12 (2019) 958–964.
- [133] J. Xue, R. Wang, Y. Yang, *Nat. Rev. Mater.* 5 (2020) 809–827.
- [134] W. Hui, Y. Yang, Q. Xu, H. Gu, S. Feng, Z. Su, M. Zhang, J. Wang, X. Li, J. Fang, F. Xia, Y. Xia, Y. Chen, X. Gao, W. Huang, *Adv. Mater.* 32 (2019) 1906374.
- [135] H. Si, Q. Liao, Z. Kang, Y. Ou, J. Meng, Y. Liu, Z. Zhang, Y. Zhang, *Adv. Funct. Mater.* 27 (2017) 1701804.
- [136] J. Wang, K. Datta, C.H.L. Weijtens, M.M. Wienk, R.A.J. Janssen, *Adv. Funct. Mater.* 29 (2019) 1905883.
- [137] S.-K. Huang, Y.-C. Wang, W.-C. Ke, Y.-T. Kao, N.-Z. She, J.-X. Li, C.-W. Luo, A. Yabushita, D.-Y. Wang, Y.J. Chang, K. Tsukagoshi, C.-W. Chen, *J. Mater. Chem. A* 8 (2020) 23607–23616.
- [138] J.-T.-W. Wang, J.M. Ball, E.M. Bareja, A. Abate, J.A. Alexander-Webber, J. Huang, M. Saliba, I. Mora-Sero, J. Bisquert, H.J. Snaith, R.J. Nicholas, *Nano Lett.* 14 (2014) 724–730.
- [139] J. Jiménez-López, B.M.D. Puscher, D.M. Guldí, E. Palomares, *J. Am. Chem. Soc.* 142 (2020) 1236–1246.
- [140] K. Choi, J. Lee, H.I. Kim, C.W. Park, G.-W. Kim, H. Choi, S. Park, S.A. Park, T. Park, *Energ. Environ. Sci.* 11 (2018) 3238–3247.
- [141] J. Tian, Q. Xue, X. Tang, Y. Chen, N. Li, Z. Hu, T. Shi, X. Wang, F. Huang, C. J. Brabec, H.-L. Yip, Y. Cao, *Adv. Mater.* 31 (2019) 1901152.
- [142] D. Yang, R. Yang, K. Wang, C. Wu, X. Zhu, J. Feng, X. Ren, G. Fang, S. Priya, S. Liu, *Nat. Commun.* 9 (2018) 3239.
- [143] X. Huang, R. Chen, G. Deng, F. Han, P. Ruan, F. Cheng, J. Yin, B. Wu, N. Zheng, *J. Am. Chem. Soc.* 142 (2020) 6149–6157.
- [144] X. Huang, F. Cao, S. Zhan, Q. Feng, M. Zhu, Z. Su, X. Gao, J. Yin, J. Li, N. Zheng, B. Wu, *Joule* 7 (2023) 1556–1573.
- [145] R. Chen, J. Cao, Y. Duan, Y. Hui, T.T. Chuong, D. Ou, F. Han, F. Cheng, X. Huang, B. Wu, N. Zheng, *J. Am. Chem. Soc.* 141 (2019) 541–547.
- [146] M. Fahim, I. Firdous, W. Zhang, W.A. Daoud, *Nano Energy* 86 (2021), 106127.
- [147] X. Wu, J. Zhang, M. Qin, K. Liu, Z. Lv, Z. Qin, X. Guo, Y. Li, J. Xu, G. Li, H. Yan, X. Lu, *EcoMat* 4 (2022) e12192.
- [148] F. Cheng, X. Jing, R. Chen, J. Cao, J. Yan, Y. Wu, X. Huang, B. Wu, N. Zheng, *Inorg. Chem. Front.* 6 (2019) 2458–2463.
- [149] J.C. Yu, D.B. Kim, G. Baek, B.R. Lee, E.D. Jung, S. Lee, J.H. Chu, D.-K. Lee, K. J. Choi, S. Cho, M.H. Song, *Adv. Mater.* 27 (2015) 3492–3500.
- [150] J. Cao, B. Wu, R. Chen, Y. Wu, Y. Hui, B.-W. Mao, N. Zheng, *Adv. Mater.* 30 (2018) 1705596.
- [151] Z. Pang, S. Yang, Y. Sun, L. He, F. Wang, L. Fan, S. Chi, X. Sun, L. Yang, J. Yang, *Chem. Eng. J.* 439 (2022), 135701.
- [152] J. Chung, S.S. Shin, K. Hwang, G. Kim, K.W. Kim, D.S. Lee, W. Kim, B.S. Ma, Y.-K. Kim, T.-S. Kim, J. Seo, *Energ. Environ. Sci.* 13 (2020) 4854–4861.
- [153] K. Yao, S.F. Leng, Z.L. Liu, L.F. Fei, Y.J. Chen, S.B. Li, N.G. Zhou, J. Zhang, Y. X. Xu, L. Zhou, H.T. Huang, A.K.Y. Jen, *Joule* 3 (2019) 417–431.
- [154] Z. Cao, C. Li, X. Deng, S. Wang, Y. Yuan, Y. Chen, Z. Wang, Y. Liu, L. Ding, F. Hao, *J. Mater. Chem. A* 8 (2020) 19768–19787.
- [155] Y. Lv, R. Yuan, B. Cai, B. Bahrami, A.H. Chowdhury, C. Yang, Y. Wu, Q. Qiao, S. Liu, W.-H. Zhang, *Angew. Chem. Int. Ed.* 59 (2020) (1976) 11969–11961.
- [156] H. Si, Z. Kang, X. Cheng, Z. Bai, Y. Zhang, *Chinese Journal of Engineering* 39 (2017) 973–980.
- [157] X. Chen, P. Lin, X. Yan, Z. Bai, H. Yuan, Y. Shen, Y. Liu, G. Zhang, Z. Zhang, Y. Zhang, *ACS Appl Mater. Interfaces* 7 (2015) 3216–3223.
- [158] F. Wang, Y. Zhang, M. Yang, J. Du, L. Xue, L. Yang, L. Fan, Y. Sui, J. Yang, X. Zhang, *Nano Energy* 63 (2019), 103825.
- [159] F. Wang, M. Yang, Y. Zhang, J. Du, D. Han, L. Yang, L. Fan, Y. Sui, Y. Sun, X. Meng, J. Yang, *Chem. Eng. J.* 402 (2020), 126303.
- [160] Y.W. Noh, I.S. Jin, K.S. Kim, S.H. Park, J.W. Jung, *J. Mater. Chem. A* 8 (2020) 17163–17173.
- [161] L. Lin, T.W. Jones, J.-T.-W. Wang, A. Cook, N.D. Pham, N.W. Duffy, B. Mihaylov, M. Grigore, K.F. Anderson, B.C. Duck, H. Wang, J. Pu, J. Li, B. Chi, G.J. Wilson, *Small* 16 (2020) 1901466.
- [162] H.B. Lee, N. Kumar, M.M. Ovhal, Y.J. Kim, Y.M. Song, J.-W. Kang, *Adv. Funct. Mater.* 30 (2020) 2001559.
- [163] Y. Gao, Y. Wu, Y. Liu, C. Chen, X. Shen, X. Bai, Z. Shi, W.W. Yu, Q. Dai, Y. Zhang, *Solar RRL* 3 (2019) 1900314.
- [164] M. Hu, L. Zhang, S. She, J. Wu, X. Zhou, X. Li, D. Wang, J. Miao, G. Mi, H. Chen, Y. Tian, B. Xu, C. Cheng, *Solar RRL* 4 (2020) 1900331.
- [165] P. Huang, Q. Chen, K. Zhang, L. Yuan, Y. Zhou, B. Song, Y. Li, *J. Mater. Chem. A* 7 (2019) 6213–6219.
- [166] P. Wang, R. Li, B. Chen, F. Hou, J. Zhang, Y. Zhao, X. Zhang, *Adv. Mater.* 32 (2020) 1905766.
- [167] J. Dagar, S. Castro-Hermosa, G. Lucarelli, F. Cacialli, T.M. Brown, *Nano Energy* 49 (2018) 290–299.
- [168] S. Song, G. Kang, L. Pyeon, C. Lim, G.-Y. Lee, T. Park, J. Choi, *ACS Energy Lett.* 2 (2017) 2667–2673.
- [169] Y. Hou, X. Chen, S. Yang, C. Li, H. Zhao, H.G. Yang, *Adv. Funct. Mater.* 27 (2017) 1700878.
- [170] P. Wang, J. Zhao, J. Liu, L. Wei, Z. Liu, L. Guan, G. Cao, *J. Power Sources* 339 (2017) 51–60.
- [171] J. Ma, G. Yang, M. Qin, X. Zheng, H. Lei, C. Chen, Z. Chen, Y. Guo, H. Han, X. Zhao, G. Fang, *Adv. Sci.* 4 (2017) 1700031.
- [172] Z. Zhu, Y. Bai, X. Liu, C.-C. Chueh, S. Yang, A.-K.-Y. Jen, *Adv. Mater.* 28 (2016) 6478–6484.
- [173] G. Hu, W. Guo, R. Yu, X. Yang, R. Zhou, C. Pan, Z.L. Wang, *Nano Energy* 23 (2016) 27–33.
- [174] J. Sun, Q. Hua, R. Zhou, D. Li, W. Guo, X. Li, G. Hu, C. Shan, Q. Meng, L. Dong, C. Pan, Z.L. Wang, *ACS Nano* 13 (2019) 4507–4513.
- [175] D. Yang, R. Yang, C. Zhang, T. Ye, K. Wang, Y. Hou, L. Zheng, S. Priya, S. Liu, *Adv. Mater.*, n/a (2023) 2302484.
- [176] Y. Meng, C. Liu, R. Cao, J. Zhang, L. Xie, M. Yang, L. Xie, Y. Wang, X. Yin, C. Liu, Z. Ge, *Adv. Funct. Mater.* 33 (2023) 2214788.
- [177] B. Yang, D. Bogachuk, J. Suo, L. Wagner, H. Kim, J. Lim, A. Hinsch, G. Boschloo, M.K. Nazeeruddin, A. Hagfeldt, *Chem. Soc. Rev.* 51 (2022) 7509–7530.
- [178] Z. Zheng, F. Li, J. Gong, Y. Ma, J. Gu, X. Liu, S. Chen, M. Liu, *Adv. Mater.* 34 (2022) 2109879.
- [179] J. Min, S. Demchyshyn, J.R. Sempionatto, Y. Song, B. Hailegnaw, C. Xu, Y. Yang, S. Solomon, C. Putz, L.E. Lehner, J.F. Schwarz, C. Schwarzsinger, M.C. Scharber, E. Shirzaei Sani, M. Kaltenbrunner, W. Gao, *Nature*, *Electronics* (2023).
- [180] S.Y. Park, K. Zhu, *Adv. Mater.* 34 (2022) 2110438.
- [181] L. Duan, D. Walter, N. Chang, J. Bullock, D. Kang, S.P. Phang, K. Weber, T. White, D. Macdonald, K. Catchpole, H. Shen, *Nat. Rev. Mater.* 8 (2023) 261–281.
- [182] Z. Huang, L. Li, T. Wu, T. Xue, W. Sun, Q. Pan, H. Wang, H. Xie, J. Chi, T. Han, X. Hu, M. Su, Y. Chen, Y. Song, *Nat. Commun.* 14 (2023) 1204.
- [183] C.-C. Zhang, S. Yuan, Y.-H. Lou, Q.-W. Liu, M. Li, H. Okada, Z.-K. Wang, *Adv. Mater.* 32 (2020) 2001479.
- [184] Z. Dai, S.K. Yadavalli, M. Chen, A. Abbaspourtamijani, Y. Qi, N.P. Padture, *Science* 372 (2021) 618–622.
- [185] Z. Dai, S. Li, X. Liu, M. Chen, C.E. Athanasiou, B.W. Sheldon, H. Gao, P. Guo, N. P. Padture, *Adv. Mater.* 34 (2022) 2205301.
- [186] Q. Dong, C. Zhu, M. Chen, C. Jiang, J. Guo, Y. Feng, Z. Dai, S.K. Yadavalli, M. Hu, X. Cao, Y. Li, Y. Huang, Z. Liu, Y. Shi, L. Wang, N.P. Padture, Y. Zhou, *Nat. Commun.* 12 (2021) 973.
- [187] G. Lee, M.-C. Kim, Y.W. Choi, N. Ahn, J. Jang, J. Yoon, S.M. Kim, J.-G. Lee, D. Kang, H.S. Jung, M. Choi, *Energ. Environ. Sci.* 12 (2019) 3182–3191.
- [188] O.Y. Gong, G.S. Han, S. Lee, M.K. Seo, C. Sohn, G.W. Yoon, J. Jang, J.M. Lee, J. H. Choi, D.-K. Lee, S.B. Kang, M. Choi, N.-G. Park, D.H. Kim, H.S. Jung, *ACS Energy Lett.* 7 (2022) 2893–2903.
- [189] M.M. Tavakoli, Q. Lin, S.-F. Leung, G.C. Lui, H. Lu, L. Li, B. Xiang, Z. Fan, *Nanoscale* 8 (2016) 4276–4283.
- [190] M.J. Paik, J.W. Yoo, J. Park, E. Noh, H. Kim, S.-G. Ji, Y.Y. Kim, S.I. Seok, *ACS Energy Lett.* 7 (2022) 1864–1870.
- [191] J. Deng, K. Wei, L. Yang, L. Lin, Y. Xiao, X. Cai, C. Zhang, D. Wu, X. Zhang, J. Zhang, *Adv. Mater.* 35 (2023) 2300233.
- [192] S. Wu, Z. Li, J. Zhang, X. Wu, X. Deng, Y. Liu, J. Zhou, C. Zhi, X. Yu, W.C.H. Choy, Z. Zhu, A.-K.-Y. Jen, *Adv. Mater.* 33 (2021) 2105539.
- [193] K. Wei, J. Deng, L. Yang, C. Zhang, M. Huang, X. Cai, X. Zhang, J. Zhang, *Adv. Energy Mater.* 13 (2023) 2203448.
- [194] L. Zhang, C. Fu, S. Wang, M. Wang, R. Wang, S. Xiang, Z. Wang, J. Liu, H. Ma, Y. Wang, Y. Yan, M. Chen, L. Shi, Q. Dong, J. Bian, Y. Shi, *Adv. Funct. Mater.* 33 (2023) 2213961.
- [195] N. Rolston, W.J. Scheideler, A.C. Flick, J.P. Chen, H. Elmaraghi, A. Sleagh, O. Zhao, M. Woodhouse, R.H. Dauskardt, *Joule* 4 (2020) 2675–2692.
- [196] X. Tian, S.D. Stranks, F. You, *Nat. Sustainability* 4 (2021) 821–829.
- [197] J. Gong, S.B. Darling, F. You, *Energ. Environ. Sci.* 8 (2015) 1953–1968.
- [198] NREL Champion Photovoltaic Module Efficiency Chart, <https://www.nrel.gov/pv/module-efficiency.html>.
- [199] J. Li, H. Wang, X.Y. Chin, H.A. Dewi, K. Vergeer, T.W. Goh, J.W.M. Lim, J.H. Lew, K.P. Loh, C. Soci, *Joule* 4 (2020) 1035–1053.
- [200] D.H. Kim, J.B. Whitaker, Z. Li, M.F.A.M. van Hest, K. Zhu, *Joule* 2 (2018) 1437–1451.
- [201] K. Hwang, Y.-S. Jung, Y.-J. Heo, F.H. Scholes, S.E. Watkins, J. Subbiah, D. J. Jones, D.-Y. Kim, D. Vak, *Adv. Mater.* 27 (2015) 1241–1247.
- [202] N.-G. Park, K. Zhu, *Nat. Rev. Mater.* 5 (2020) 333–350.
- [203] S. He, L. Qiu, D.-Y. Son, Z. Liu, E.J. Juarez-Perez, L.K. Ono, C. Stecker, Y. Qi, *ACS Energy Lett.* 4 (2019) 2032–2039.
- [204] J. Dagar, S. Castro-Hermosa, M. Gasbarri, A.L. Palma, L. Cina, F. Matteocci, E. Calabro, A. Di Carlo, T.M. Brown, *Nano Res.* 11 (2018) 2669–2681.

- [205] Z. Liu, L. Qiu, L.K. Ono, S. He, Z. Hu, M. Jiang, G. Tong, Z. Wu, Y. Jiang, D.-Y. Son, *Nat. Energy* 5 (2020) 596–604.
- [206] B. Ding, S.-Y. Huang, Q.-Q. Chu, Y. Li, C.-X. Li, C.-J. Li, G.-J. Yang, *J. Mater. Chem. A* 6 (2018) 10233–10242.
- [207] J. Li, T. Bu, Y. Liu, J. Zhou, J. Shi, Z. Ku, Y. Peng, J. Zhong, Y.B. Cheng, F. Huang, *ChemSusChem* 11 (2018) 2898–2903.
- [208] G. Bai, Z. Wu, J. Li, T. Bu, W. Li, W. Li, F. Huang, Q. Zhang, Y.-B. Cheng, J. Zhong, *Sol. Energy* 183 (2019) 306–314.
- [209] G.S. Han, J. Kim, S. Bae, S. Han, Y.J. Kim, O.Y. Gong, P. Lee, M.J. Ko, H.S. Jung, *ACS Energy Lett.* 4 (2019) 1845–1851.
- [210] E. Calabro, F. Matteocci, A.L. Palma, L. Vesce, B. Taheri, L. Carlini, I. Pis, S. Nappini, J. Dagar, C. Battocchio, *Sol. Energy Mater. Sol. Cells* 185 (2018) 136–144.
- [211] T. Bu, S. Shi, J. Li, Y. Liu, J. Shi, L. Chen, X. Liu, J. Qiu, Z. Ku, Y. Peng, J. Zhong, Y.-B. Cheng, F. Huang, *ACS Appl. Mater. Interfaces* 10 (2018) 14922–14929.
- [212] L. Luo, Y. Zhang, N. Chai, X. Deng, J. Zhong, F. Huang, Y. Peng, Z. Ku, Y.-B. Cheng, *J. Mater. Chem. A* 6 (2018) 21143–21148.
- [213] L. Qiu, Z. Liu, L.K. Ono, Y. Jiang, D.Y. Son, Z. Hawash, S. He, Y. Qi, *Adv. Funct. Mater.* 29 (2019) 1806779.
- [214] L. Qiu, S. He, Y. Jiang, D.-Y. Son, L.K. Ono, Z. Liu, T. Kim, T. Bouloumis, S. Kazaoui, Y. Qi, *J. Mater. Chem. A* 7 (2019) 6920–6929.
- [215] B. Taheri, E. Calabro, F. Matteocci, D. Di Girolamo, G. Cardone, A. Liscio, A. Di Carlo, F. Brunetti, *Energ. Technol.* 8 (2020) 1901284.
- [216] K.-S. Lim, D.-K. Lee, J.-W. Lee, N.-G. Park, *J. Mater. Chem. A* 8 (2020) 9345–9354.
- [217] T. Bu, X. Liu, J. Li, W. Huang, Z. Wu, F. Huang, Y.-B. Cheng, J. Zhong, *Solar RRL* 4 (2020) 1900263.
- [218] M. Singh, C.-H. Chiang, K.M. Boopathi, C. Hanmandlu, G. Li, C.-G. Wu, H.-C. Lin, C.-W. Chu, *J. Mater. Chem. A* 6 (2018) 7114–7122.
- [219] J. He, E. Bi, W. Tang, Y. Wang, X. Yang, H. Chen, L. Han, *Nano-Micro Letters* 10 (2018) 1–8.
- [220] F. Di Giacomo, V. Zardetto, A. D'Epifanio, S. Pescetelli, F. Matteocci, S. Razza, A. Di Carlo, S. Licoccia, W.M. Kessels, M. Creatore, *Adv. Energy Mater.* 5 (2015) 1401808.
- [221] Y. Jiang, M. Remeika, Z. Hu, E.J. Juarez-Perez, L. Qiu, Z. Liu, T. Kim, L.K. Ono, D.-Y. Son, Z. Hawash, M.R. Leyden, Z. Wu, L. Meng, J. Hu, Y. Qi, *Adv. Energy Mater.* 9 (2019) 1803047.
- [222] F. Di Giacomo, S. Shanmugam, H. Fledderus, B.J. Bruijnaers, W.J.H. Verhees, M. S. Dorenkamp, S.C. Veenstra, W. Qiu, R. Gehlhaar, T. Mercckx, T. Aernouts, R. Andriessen, Y. Galagan, *Sol. Energy Mater. Sol. Cells* 181 (2018) 53–59.
- [223] D. Vak, K. Hwang, A. Faulks, Y.-S. Jung, N. Clark, D.-Y. Kim, G.J. Wilson, S. E. Watkins, *Adv. Energy Mater.* 5 (2015) 1401539.
- [224] R. Wang, M. Mujahid, Y. Duan, Z.-K. Wang, J. Xue, Y. Yang, *Adv. Funct. Mater.* 29 (2019) 1808843.
- [225] Z. Guo, L. Gao, C. Zhang, Z. Xu, T. Ma, *J. Mater. Chem. A* 6 (2018) 4572–4589.
- [226] T. Leijtens, G.E. Eperon, S. Pathak, A. Abate, M.M. Lee, H.J. Snaith, *Nat. Commun.* 4 (2013) 2885.
- [227] J. Ji, X. Liu, H. Jiang, M. Duan, B. Liu, H. Huang, D. Wei, Y. Li, M. Li, *iScience*, 23 (2020) 101013.
- [228] Z. Kang, H. Si, S. Zhang, J. Wu, Y. Sun, Q. Liao, Z. Zhang, Y. Zhang, *Adv. Funct. Mater.* 29 (2019) 1808032.
- [229] P. Zhang, J. Wu, T. Zhang, Y. Wang, D. Liu, H. Chen, L. Ji, C. Liu, W. Ahmad, Z. D. Chen, S. Li, *Adv. Mater.* 30 (2018).
- [230] P. Zhang, J. Wu, Y. Wang, H. Sarvari, D. Liu, Z.D. Chen, S. Li, *J. Mater. Chem. A* 5 (2017) 17368–17378.
- [231] M.V. Khenkin, E.A. Katz, A. Abate, G. Bardizza, J.J. Berry, C. Brabec, F. Brunetti, V. Bulović, Q. Burlingame, A. Di Carlo, R. Cheacharoen, Y.-B. Cheng, A. Colsmann, S. Cros, K. Domanski, M. Dusza, C.J. Fell, S.R. Forrest, Y. Galagan, D. Di Girolamo, M. Grätzel, A. Hagfeldt, E. von Hauff, H. Hoppe, J. Kettle, H. Köbler, M.S. Leite, S. Liu, Y.-L. Loo, J.M. Luther, C.-Q. Ma, M. Madsen, M. Manceau, M. Matheron, M. McGehee, R. Meitzner, M.K. Nazeeruddin, A. F. Nogueira, Ç. Odabaşı, A. Oshevov, N.-G. Park, M.O. Reese, F. De Rossi, M. Saliba, U.S. Schubert, H.J. Snaith, S.D. Stranks, W. Tress, P.A. Troshin, V. Turkovic, S. Veenstra, I. Visoly-Fisher, A. Walsh, T. Watson, H. Xie, R. Yıldırım, S.M. Zakeeruddin, K. Zhu, M. Lira-Cantu, *Nat. Energy* 5 (2020) 35–49.